

T2231

THE DIRECT CURRENT RESISTIVITY MODELING OF THIN INSULATORS

WEN J. WHAN

ProQuest Number: 11016695

All rights reserved

INFORMATION TO ALL USERS

The quality of this reproduction is dependent upon the quality of the copy submitted.

In the unlikely event that the author did not send a complete manuscript and there are missing pages, these will be noted. Also, if material had to be removed, a note will indicate the deletion.



ProQuest 11016695

Published by ProQuest LLC (2019). Copyright of the Dissertation is held by the Author.

All rights reserved.

This work is protected against unauthorized copying under Title 17, United States Code
Microform Edition © ProQuest LLC.

ProQuest LLC.
789 East Eisenhower Parkway
P.O. Box 1346
Ann Arbor, MI 48106 – 1346

A Thesis submitted to the Faculty and the Board of Trustees
of the Colorado School of Mines in partial fulfillment of the
requirements for the degree of Doctor of Philosophy.

Signed: Wen J. Whan
Wen J. Whan

Golden, Colorado
Date: 10/18, 1979

Approved: Charles H. Stoyer
Dr. Charles H. Stoyer
Thesis Advisor

Phillip R. Romig
Dr. Phillip R. Romig
Head of Department- Geophysics

Golden, Colorado
Date: 10/25, 1979

ABSTRACT

A method is developed for the solution of the resistivity modeling problem for three-dimensional thin inhomogeneities buried in a halfspace. Investigating the boundary conditions across the thin layers and applying the Green's identity with these boundary conditions, the problems reduce to Fredholm integral equations of the second kind. These are solved by dividing the thin body into a number of thin rectangular facets, which allows us to replace the Fredholm integral equation by a set of simultaneous algebraic equations. These are then solved by Gaussian elimination.

A number of results, which model the response of thin insulating disks set in an otherwise homogeneous earth, are given for a bipole source. The second vertical derivatives of the potentials, which enhance the signal from the thin insulating disk, are calculated using this array. A positive response from this calculation depends on the extent, depth and the transverse resistance of the thin layer. Using a buried current electrode and measuring the second vertical derivative of the potential on the surface, the thin layer can be detected more positively.

The numerical results show that for a model corresponding to an overburden of 1,000 meters of 10 ohm-meter material and a producing zone 100 meter thick with a resistivity of 50 ohm-meters, the difference between the maximum and the minimum normalized second vertical derivative is about seven percent, while that for the total electrical field apparent resistivity is only about three percent. The smaller the radius of the disk the lower the anomaly. As the thin disk is extended in radius, its normalized second vertical derivative transforms in character from one which has closed low contours just above the disk to one which has contours surrounding the current sources and which has a much larger anomaly, up to seven hundred percent. As T_2/T_1 increases, the normalized second vertical derivative saturates at about 9-10 % for the horizontal disk with the radius being equal to the thickness of the overburden, and for a T_2/T_1 equal to 3.

By the Green's identity approach the problem of the topography effect reduces to a Fredholm integral equation of the second kind. The results are sufficiently accurate for correcting field data corrupted with topography effects.

CONTENTS

	Page
Illustrations	vi
Acknowledgments	ix
Chapter 1: Introduction	1
Chapter 2: Arbitrarily Shaped Bodies	6
Chapter 3: Imperfect Thin Insulators	9
Chapter 4: Perfect Thin Insulators	24
Chapter 5: Modeling with an Irregular Surface	29
Chapter 6: Solutions of Integral Equations	36
Chapter 7: The Second Vertical Derivative of the Potential	45
Chapter 8: Numerical Results	51
Chapter 9: Conclutions	110
Appendix 1: Analytical Solution for An Imperfect Thin Sphere in an uniform field	113
Appendix 2: Analytical Solutions of Two Co-origin Spheres in an uniform field	118
Appendix 3: The Integration of The Kernel of the Integral Equation over a rectangle	121
Appendix 4: User's Manuals	123
References	133

ILLUSTRATIONS

Figure	Page
1. An irregular body buried in a homogeneous half space and its image with respect to the earth surface.	8
2. Real world model of the direct current prospecting over an imperfect thin insulator	12
3. For an imperfect thin insulator, the normal component of the current density should be continuous.	12
4. Symmetry disallows normal current along surface S.	16
5. The normal directions at points on the boundaries.	20
6. The normal direction at a point on the mathematic boundary.	20
7. Physical model for an homogeneous earth with irregular earth surface.	33
8. Physical model of a buried body with irregular earth surface	33
9. Model shows the inner space proposed and the normal directions of the surface.	34
9-1. Calculation of the second vertical derivative from the potentials.	45
9-2. Calculation of the second vertical derivative from the field measurement.	46
9-3. Contour map of the normalized total potential for the model shown in the same map.	48
9-4. Contour map of the apparent resistivity for the same model as that in Fig. 9-3.	49
9-5. Contour map of the normalized second vertical derivative for the same model as that in Figure 9-3.	50

Figure	Page
10. Two co-original half spheres buried just beneath the surface and subjected to a uniform primary electrical field.	53
11. A half sphere is simulated by 40 triangular facets.	53
12-14 Comparison of the analytical and the numerical results for the multiple reflection coefficient case.	54-6
15. The model and the source locations from which the normalized second vertical derivative is calculated.	58
16-23 The contour maps of the normalized second vertical derivative for the model shown in Fig. 15 with different reflection coefficients.	59-66
24. An imperfect thin half sphere buried just beneath the surface and subjected to a uniform primary electrical field.	68
25-29 Comparison of the analytical and the numerical results for the imperfect thin insulator case.	69-73
30. The thin circular disk is divided into rectangular facets.	75
31. The model and the source locations from which the normalized second vertical derivative is calculated.	76
32-43 The contour maps of the normalized second vertical derivative for the model shown in Figure 31 with different parameters.	77-82, 85-90
43A-C The contour map of the normalized second vertical derivative for a thin horizontal layer.	91-93
44. Physical model of the secondary electrical field from the thin disk.	95
45. The model and the location for the buried current electrode from which the second vertical derivative is calculated.	97

Figure	Page
46-49 The contour maps of the normalized second vertical derivative for the model shown in Fig. 45 with different parameters.	98-101
50. The zero contour of the second vertical derivative for an uniform earth. The current electrode is buried at (0., 0., 0.5).	102
51-53 The contour maps of the second vertical derivative using buried current electrode for different models.	104-6
54. The testing model for calculating the topography response.	107
55. The comparison of the analytical and the numerical results for the topography effect.	108.

Tables

1. The maximum values of the normalized secondary vertical derivative of the total field for the model shown in fig. 31. Diameter of the disk is two	84
2. Diameter of the disk is one	84
3. The relations between the maximum values of the normalized secondary vertical derivatives and the sources' locations. Model is as fig 31. Transverse resistance of the disk is one.	103
4. The minimum values of the normalized secondary vertical derivative of the total field for the model shown in fig 31 with different T values. Current electrode is buried	103

ACKNOWLEDGEMENTS

I would like to thank my advisor, Dr. Charles H. Stoyer for all his help from the first day I came to the school. Professors Robert G. Underwood, George V. Keller, Alexander A. Kaufman and Frank A. Hadsell also served as committee members and made valuable suggestions during the preparation of the report.

I gratefully acknowledge the support provided by the geophysical department during this study, in the form of research assistantships. I am especially in debt to Dr. Keller who made this support available.

My wife, Kong M. Whan is an invaluable source of inspiration which helped me complete this research.

CHAPTER 1: INTRODUCTION

Three cases are treated in this thesis. These are resistivity modeling for

- 1) thin insulators in a homogeneous half space.
- 2) multiple bodies with multiple reflection coefficients,
- 3) uniform earth with irregular surface.

As oil becomes more scarce, more effort must be devoted to oil exploration techniques. Most oil exploration is done using the seismic reflection method. Electrical methods are much simpler and the expense of electrical exploration is much less than that of reflection seismic exploration. To find the oil by electrical methods is thus worthwhile. We have chosen the direct current resistivity method for this study. The equipment for this method is simple to design and interpretation is more straightforward than other electrical methods.

The electrical methods are not applicable for surveys under some geological conditions. So it is very helpful to delineate the conditions under which the electrical methods can be successfully applied. Oil reservoirs are usually

more resistive than the surrounding medium. Most of them are thin layers compared with the thickness of the overburden and the lateral dimensions of the oil reservoir. The response of the oil reservoir using resistivity method is thus small; however by choosing some specific source and receiver configurations, the detectability can be enhanced. The objective of this investigation is to define the response of these thin layers. Also of interest in this study are the general techniques of the integral equation approach to direct current modeling problems. The problems are solved by first investigating the boundary conditions and then applying Green's identity to derive the specific integral equations. These are then solved numerically.

Assume the variation of all electrical properties of the medium occurs only at discrete boundaries. The sources of the electric field caused by driving a direct current into the ground can be considered as surface sources distributed on the boundaries and point sources at the current electrodes. Solving the boundary value problem, these source distribution can be expressed as the solution of a Fredholm integral equation of the second kind. Solving this integral equation for source distribution, we then can get the potential field at any point (Dieter et al, 1969;

Barnett, 1972; Snyder, 1975).

Finite difference and finite element methods (Geoscience, 1965; Coggon, 1971) have also been widely applied to solve the boundary value problems, but computer time and storage requirements make these methods unwieldy in three dimensional problems. The integral equation solution is much more storage- and computation-efficient, but for large or complicated-shape bodies, the integral equation can not always be solved properly.

Consider a horizontally layered earth containing 3 layers, in which the second layer is very thin and resistive compared with the first and the third layers. The analytic expression for the potential can be reduced asymptotically to an expression which is function of T , h_1 , ρ_1 , ρ_3 instead of h_1 , h_2 , ρ_1 , ρ_2 , ρ_3 , where ρ represents the resistivity, h represent the thickness of the layer and T represents the insulating factor of the second layer., which is equal to $h_2\rho_2$ (Keller, 1966).

Assume that h_2 is much smaller than any of the other dimensions and that the distance between the layer and the current electrode is much greater than h_2 . Also assume that

we measure the electric field very far from the layer compared with .

Hurley (1975) derived the boundary conditions across the thin layer by mathematical asymptotic expansion (Cole, 1968) for both the insulating and the conducting case. An alternative approach for obtaining the boundary conditions across the thin insulating layer was applied in this thesis. In this approach, the physical considerations are that the normal component of the current density is continuous across the thin insulating layers.

In this thesis, the potential arising from current sources placed in the vicinity of an arbitrarily shaped thin layer is expressed in terms of fictitious source distributions over the thin layer. These secondary source distributions are formulated in Fredholm's integral equations of the second kind by applying the Green's identity with the specific boundary conditions. Since the integral equations are with respect to a single sheet, they are suitable for numerical solution. Physically speaking, the secondary sources over the insulating thin layer are dipoles.

The problem of modeling the topography effect is formulated into a Fredholm integral equation of the second kind and the accuracy of the program is demonstrated.

There are two methods for solving the integral equation. They are the method of successive approximations and the simultaneous equation method. In this paper, the integral equations for the multiple body case and the topography effect case are solved by the successive approximation method where the secondary source distributions are expanded into series in the electric parameters. However for the thin layer cases, the electric parameter, T , can be infinity. It is thus improper to apply the successive approximation method. Instead, the simultaneous equation method is applied.

CHAPTER 2: ARBITRARILY SHAPED BODIES

The mathematical problem of determining the direct current response of an arbitrarily shaped body immersed in an homogeneous earth can be shown as the problem of solving the Laplace equation with the following boundary conditions (Barnett, 1972):

$$(1) \left. \frac{\partial U}{\partial Z} \right|_{Z=0} = 0 \quad (2-1)$$

$$(2) U(m^+) = U(m^-) \quad (2-2)$$

$$(3) \left. \frac{1}{\rho_e} \frac{\partial U(m^+)}{\partial n} \right|_S = \left. \frac{1}{\rho_i} \frac{\partial U(m^-)}{\partial n} \right|_S \quad (2-3)$$

$$(4) U \rightarrow \frac{\rho_i I}{2\pi R} \text{ near source placed on the surface} \quad (2-4)$$

where:

U is the electric potential

ρ_e is the resistivity of the homogeneous earth

ρ_i is the resistivity of the arbitrarily shaped body

S is the boundary of the arbitrarily shaped body

I is the current being put into the ground

m^+ is a point approaching S from exterior of the body

m^- is the point approaching S from interior of the body

R is the distance between the current electrode and

the observation point.

It is shown by Barnett (1972) that the solution for the above problem can be expressed by

$$U(Q) = \frac{\rho_e I}{4\pi} \left(\frac{1}{r_{AQ}} + \frac{1}{r_{\underline{A}Q}} \right) + \int_S \sigma(p) \frac{1}{r_{pQ}} ds + \int_{\underline{S}} \sigma(\underline{p}) \frac{1}{r_{\underline{p}Q}} ds \quad (2-5)$$

where σ is the unknown source distribution defined by

$$\sigma(m) = \frac{K \rho_e I}{2\pi} \left(\frac{\partial}{\partial n} \left(\frac{1}{r_{Am}} \right) + \frac{\partial}{\partial n} \left(\frac{1}{r_{\underline{A}m}} \right) \right) + \frac{K}{2\pi} \left(\int_{S'} \sigma(p) \frac{\partial}{\partial n} \left(\frac{1}{r_{pm}} \right) ds + \int_{\underline{S}} \sigma(\underline{p}) \frac{\partial}{\partial n} \left(\frac{1}{r_{\underline{p}m}} \right) d\underline{S} \right) \quad (2-6)$$

and:

A is the position of the current electrode.

Q is the observation point.

K is the reflection coefficient defined by $\frac{\rho_i - \rho_e}{\rho_i + \rho_e}$

p, m are the points near S

\underline{S} is the image surface of S with respect to the earth surface.

\underline{A} is the image point of A with respect to the earth surface.

\underline{p} is a point on \underline{S}

S' is the surface of S with point m deleted.

n is the normal direction of S at point m, points outward from interior of the body.

The configuration of the above arrangement is illustrated in Fig.1. For the multiple body case, we just consider K as a function of p and put K inside the integral of Eq.(2-6).

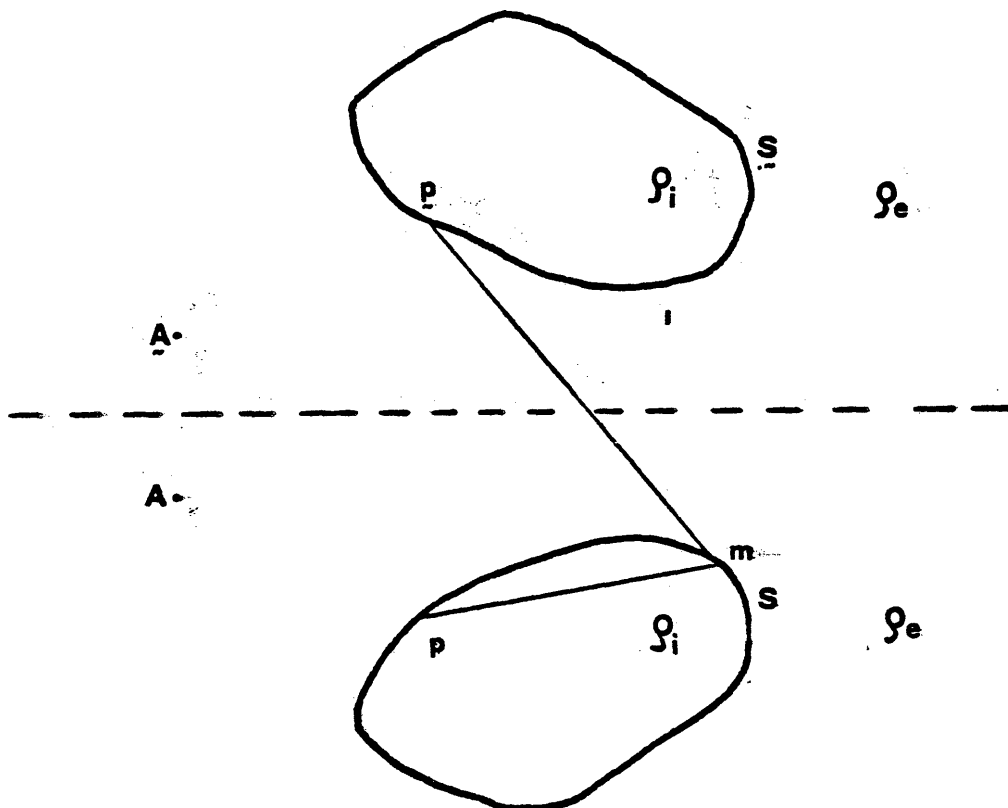


Fig.1 : An irregular body buried in a homogeneous half space and its image with respect to the earth surface.

CHAPTER 3: IMPERFECT THIN INSULATOR

If the arbitrarily shaped body as shown in Fig.1, chapter 2, is a thin layer, expressions (2-5) and (2-6) for the electric potential and the source distribution still hold. But in order to solve them numerically, the area of the finite facets which simulate the surface of the thin body must be much smaller than the thickness of the layer squared. Thus, it will be wasteful, at least, to solve the integral equation (2-6) without making use of the thinness to reduce the extent of the integration.

In this section, we derive the boundary conditions across the imperfect thin insulator. The mathematical problem turns out to be a Laplace problem with our new boundary conditions. Solving by the Green's function method, it is shown that there is a dipole moment distribution on the layer which can be expressed once again in the form of the Fredholm's integral equation of the second kind. This introduces numerical accuracy and changes the area of integration from a closed surface to an open one.

Boundary Conditions

The model to be solved is represented by Fig.2, where A is the point of the direct current source. m is the point of the receiver where we want to know the value of the electric potential, S_a is the surface of the current electrode, S_e is the air-earth interface, S_t is the surface of the imperfect thin insulator, V is the volume surrounded by S_a , S_e and S_t .

On S_e , since there are no currents flowing into free space, we have the following boundary condition:

The following condition:

$$\left. \frac{\partial U}{\partial z} \right|_{z=0} = 0 \quad (3-1)$$

On S_a , the current flowing through the surface of the electrode is equal to the total current put into the ground,

i.e.:

$$\oint_{S_a} \vec{j} \cdot d\vec{S}' = -I \quad (3-2)$$

where the direction of $d\vec{S}'$ is outward from the current electrode or inward in volume V.

From Ohm's law, we have:

$$\vec{j} = \sigma_e \vec{E} = -\frac{1}{\rho_e} \nabla U \quad (3-3)$$

where σ_e is the conductivity of the medium.

Substituting (3-3) into (3-2), we get:

$$\oint_{S_a} \nabla U \cdot d\vec{S}' = I \rho_e \quad (3-4)$$

where $\vec{ds} = -d\vec{s}$. \vec{ds} is then pointing outward from the volume

On S_t , since the layer is very thin and since the current tends not to flow along the highly resistive layer, it is reasonable to see that the normal component of the current density is continuous across the layer. That is

$$J_n^+ = J_n^i = J_n^- \quad (3-5)$$

as shown in Fig.3.

From Ohm's law, we get
$$\frac{1}{\rho_e} E_n^+ = \frac{1}{\rho_i} E_n^i = \frac{1}{\rho_e} E_n^- \quad (3-6)$$

The potential difference between the points just above and

below the layer is:

$$U^+ - U^- = - \int_{-}^{+} \vec{E}^i \cdot d\vec{q} \quad (3-6-1)$$

which can be reduced by the following sequence:

$$\begin{aligned} U^+ - U^- &= - \int_{-}^{+} E^i \cdot dl \\ &= - E_n^i \ell \\ &= - \frac{\rho_i}{\rho_e} E_n^+ \ell \end{aligned}$$

If $T = \rho_i \ell$, then

$$\begin{aligned} U^+ - U^- &= - \frac{T}{\rho_e} E_n^+ \\ &= - \frac{T}{\rho_e} E_n^e \\ &= \frac{T}{\rho_e} \frac{\partial U^e}{\partial n} \end{aligned} \quad (3-7)$$

where \vec{n} is pointed as shown in Fig.3, which points from the

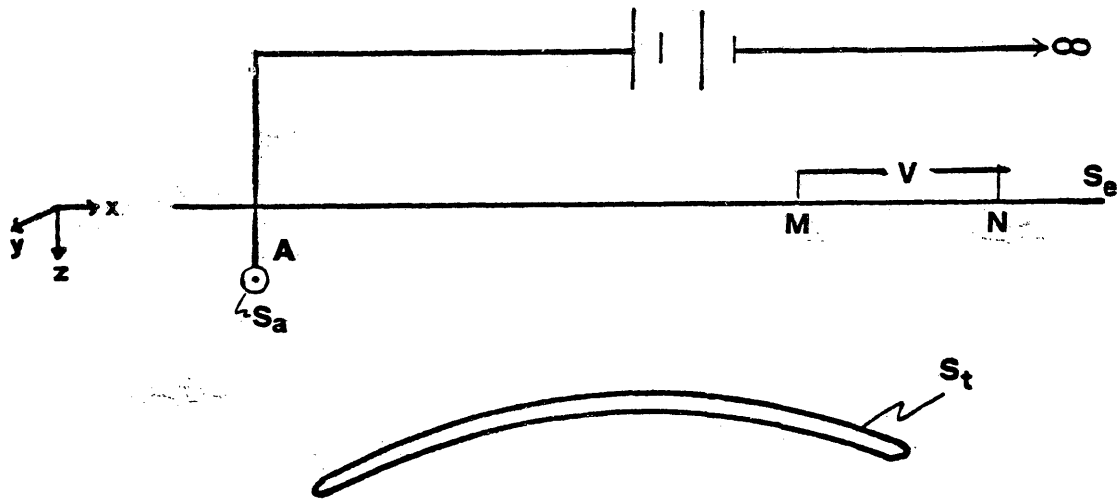


Fig. 2: Real world model of the direct current prospecting over an imperfect thin insulator.

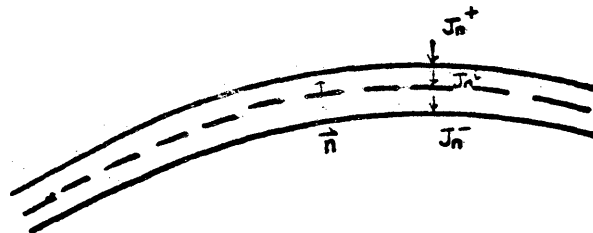


Fig. 3: For an imperfect thin insulator, the normal component of the current density should be continuous.

negative side to the positive side and $\frac{\partial U^e}{\partial n}$ represents the normal component of the electrical field just outside the layer. The direction of \vec{n} is the same as that of the normal vector at the corresponding point on the upper surface.

From the above discussion, we can summarize our mathematical problem for the imperfect thin insulator as follows:

Solving the Laplace equation

$$\nabla^2 U = 0 \quad \text{in } V \quad (3-11)$$

with the following boundary conditions:

$$(i) \quad \left. \frac{\partial U}{\partial z} \right|_{z=0} = 0 \quad \text{on } S_e \quad (3-12)$$

$$(ii) \quad \oint \nabla U \cdot d\vec{S} = I \rho_e \quad \text{on } S_a \quad (3-13)$$

$$(iii) \quad U^+ - U^- = \frac{T}{\rho_e} \frac{\partial U^e}{\partial n} \quad \text{across } S_t \quad (3-14)$$

$$(iv) \quad \frac{\partial U^+}{\partial n} = \frac{\partial U^-}{\partial n} \quad \text{across } S_t \quad (3-15)$$

where V is the space surrounded by the earth surface, S_e , the surface of the current electrode, S_a , and the surface of the thin layer, S_t , as shown in Fig.3, and where $\frac{\partial U^e}{\partial n}$ denotes the normal component of the electrical field just outside the layer S_t .

We use image theory to satisfy boundary condition 1, i.e. Eq.(3-12). Consider the model in Fig 4 instead of that in Fig.2. There is no current flowing across the S_e surface because the model is symmetric about this plane. The boundary condition 1 is then automatically satisfied.

Our mathematical problem is then modified to:

Solving the Laplace equation

$$\nabla^2 U = 0 \quad \text{in } \bar{V} \quad (3-16)$$

with the following boundary conditions:

$$(1) \oint U \cdot d\vec{S}_a = I \rho_e \quad \text{at } S_a \quad (3-17)$$

$$\oint U \cdot d\vec{S}_a = I \rho_e \quad \text{at } \underline{S}_a \quad (3-18)$$

$$(2) U^+ - U^- = \frac{\tau}{\rho_e} \frac{\partial U^e}{\partial n} \quad \text{at } S_t \text{ and } \underline{S}_t \quad (3-19)$$

$$(3) \frac{\partial U^+}{\partial n} = \frac{\partial U^-}{\partial n} \quad \text{at } S_t \text{ and } \underline{S}_t \quad (3-20)$$

where:

S_t is the surface of the thin layer

\underline{S}_t is the image surface of S_t

\bar{V} is the volume surrounded by S_a , \underline{S}_a , S_t , \underline{S}_t , as shown in Fig.4.

Integral Expression for the Electric Potential

To solve eqs.(3-16) and (3-19) using the method of Green's function we will further change \bar{V} so that it now excludes a small sphere S_m centered at a fixed point m . We

denote this new volume by V' . (see Fig.4)

The Green's function for the Laplace equation is

$$G(\vec{r}_m, \vec{r}_p) = \frac{1}{4\pi} \frac{1}{r_{pm}} \quad (3-21)$$

where:

\vec{r}_p is the position vector of the observation point p

\vec{r}_m is the position vector of the fixed point, as mentioned above.

r_{pm} is the directed distance between point p and point m .

and

\vec{r}_{pm} is the vector directed from m to p .

The Green's identity gives us the relation between the field in the region V' and the field on the boundaries as follows:

$$\int_{V'} [G(\vec{r}_m, \vec{r}) \nabla^2 U(p) - U(p) \nabla^2 G(\vec{r}_m, \vec{r}_p)] dV_p \quad (3-22)$$

$$= \oint_{S_m \cup S_a \cup S_b \cup S_t \cup S_t} [G(\vec{r}_m, \vec{r}_p) \frac{\partial U(p)}{\partial n_p} - U(p) \frac{\partial G(\vec{r}_m, \vec{r}_p)}{\partial n_p}] dS_p$$

where:

P represents a point in V'

p represents a point on the boundaries

n_p is the normal direction at point p on the boundary,

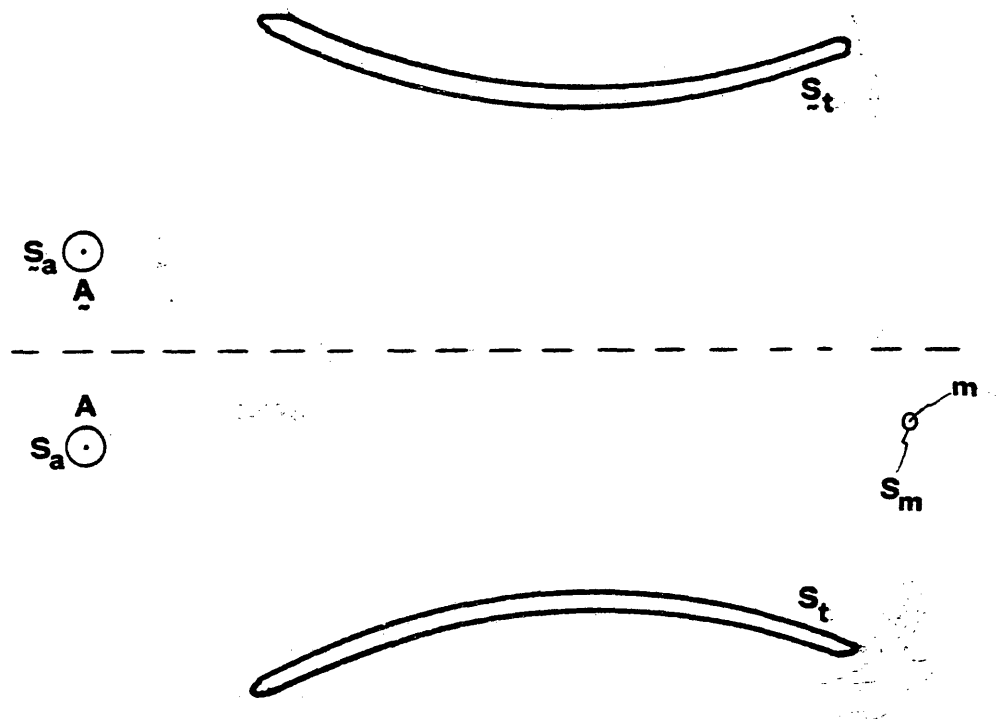


Fig.4: Symmetry disallows normal current along surface S .

which is defined to be outward from the volume V' and is shown in Fig.5.

Since $\nabla^2 G(\vec{r}_m, \vec{r}_p) = \delta(\vec{r}_m, \vec{r}_p)$ and

$$\nabla^2 U(p) = 0 \quad \text{in } V' \quad (3-23)$$

and since point m is not in V' , the left hand side of Eq.(3-22) vanishes. Now separate the right hand side of Eq.(3-22) into three integrals as follows:

$$\int_{S_m} U \frac{\partial U}{\partial n} + \int_{S_a} U \frac{\partial U}{\partial n} + \int_{S_t} U \frac{\partial U}{\partial n} \quad (3-24)$$

The first term of the right hand side of Eq.(3-24)

becomes, as the radius of the sphere approaches zero,

$$\begin{aligned} & \int_{S_m} [G(\vec{r}_m, \vec{r}_p) \frac{\partial U(p)}{\partial n_p} - U(p) \frac{\partial G(\vec{r}_m, \vec{r}_p)}{\partial n_p}] d S_p \\ &= \lim_{r \rightarrow 0} \int_0^{2\pi} \int_0^\pi \left[\frac{1}{4\pi r} \frac{\partial U(p)}{\partial n_p} - U(p) \frac{\partial}{\partial n_p} \left(\frac{1}{4\pi r} \right) \right] r^2 \sin\theta \, d\phi \, d\theta \quad (3-25) \end{aligned}$$

Since $\frac{\partial U}{\partial n}$ is continuous and uniformly bounded, the first term in the integration of the right hand side of Eq.(3-25)

becomes

$$\begin{aligned} & \lim_{r \rightarrow 0} \int_0^{2\pi} \int_0^\pi \left[\frac{1}{4\pi r} \frac{\partial U(p)}{\partial n_p} \right] r^2 \sin\theta \, d\phi \, d\theta \\ &= \lim_{r \rightarrow 0} \frac{r}{4\pi} \int_0^\pi \int_0^{2\pi} \frac{\partial U(p)}{\partial n_p} \sin\theta \, d\phi \, d\theta = 0 \quad (3-26-1) \end{aligned}$$

As $r \rightarrow 0$, it is reasonable to see that $U(p)$ is uniform on the

sphere S_m and is approximately equal to $U(m)$. Eq.(3-25)

then becomes

$$\begin{aligned} \lim_{r \rightarrow 0} \oint_{S_m} &= \lim_{r \rightarrow 0} -U(m) \int_0^{2\pi} \int_0^{\pi} \frac{\partial}{\partial n_p} \left(\frac{1}{4\pi r} \right) r^2 \sin\theta d\phi d\theta \\ &= \frac{U(m)}{2} \cos \theta \Big|_0^{\pi} = -U(m) \end{aligned} \quad (3-26)$$

where the direction of \vec{n} is opposite to that of \vec{r} and is normal to S_m , as shown in Fig.4.

The second integral on the right hand of Eq.(3-24) is

$$\begin{aligned} \text{where} \quad \oint_{S_a} U S_a &= \oint_{S_a} + \oint_{\underline{S}_a} \\ \oint_{S_a} &= \oint_{S_a} \left[G(\vec{r}_m, \vec{r}_p) \frac{\partial U(p)}{\partial n_p} - U(p) \frac{\partial G(\vec{r}_m, \vec{r}_p)}{\partial n_p} \right] dS_p \\ &= \lim_{r \rightarrow 0} \oint_{S_a} \left[G(\vec{r}_m, \vec{r}_p) \frac{U(p)}{n_p} - U(p) \frac{G(\vec{r}_m, \vec{r}_p)}{n_p} \right] dS_p \end{aligned} \quad (3-27)$$

where r is the radius of the sphere S_a or the radius of the current electrode. As r approaches zero, we can assume $G(r_m, r_p)$ is constant on S_a and is equal to $G(r_m, r_A)$. Applying the boundary condition of Eq.(3-13) the integral

$$\begin{aligned} \text{becomes} \quad \oint_{S_a} &= \oint_{S_a} \frac{1}{4\pi r_{Am}} \frac{\partial U(p)}{\partial n_p} dS_p \\ &= \frac{1}{4\pi r_{Am}} \oint_{S_a} U \cdot \vec{dS}_p = \frac{I \rho_e}{4\pi r_{Am}} \end{aligned} \quad (3-28)$$

Similarly, for the integral over S_a , we get

$$\oint_{S_a} = \frac{I \rho_e}{4 \pi r_{Am}}$$

The third integral on the right hand side of (3-24) is

where

$$\begin{aligned} \oint_{S_t} &= \int_{S_t^u} + \int_{S_t^d} \\ \oint_{S_t} &= \oint_{S_t} [G(\vec{r}_m, \vec{r}_p) \frac{\partial U(p)}{\partial n_p} - U(p) \frac{\partial G(\vec{r}_m, \vec{r}_p)}{\partial n_p}] dS_p \\ &= \int_{S_t^u} [G(\vec{r}_m, \vec{r}_{p_u}) \frac{\partial U(p_u)}{\partial n_{p_u}} - U(p_u) \frac{\partial G(\vec{r}_m, \vec{r}_{p_u})}{\partial n_{p_u}}] dS_{p_u} \\ &\quad + \int_{S_t^d} [G(\vec{r}_m, \vec{r}_{p_d}) \frac{\partial U(p_d)}{\partial n_{p_d}} - U(p_d) \frac{\partial G(\vec{r}_m, \vec{r}_{p_d})}{\partial n_{p_d}}] dS_{p_d} \end{aligned} \quad (3-30)$$

where S_t^u is the upper part of S_t

S_t^d is the lower part of S_t

p_d is a point on S_t^u

p_u is a point on S_t^d

As the thickness of the layer, l , approaches zero, i.e. as S_t approaches a single sheet S_i as shown in Fig.6, we get

$$-n_{p_u} = +n_{p_d} = n_{p^o} \quad (3-32-1)$$

where p_u, p_d, p^o and $n_{p_u}, n_{p_d}, n_{p^o}$ are as shown in Fig.6. The

Eq.(3-25) becomes

$$\begin{aligned} \oint_{S_t} &= \int_{S_t^o} [G(\vec{r}_m, \vec{r}_{p^o}) \left[\frac{\partial U^+(p^o)}{\partial n_{p^o}} + \frac{\partial U^-(p^o)}{\partial n_{p^o}} \right] \\ &\quad + \frac{\partial G(\vec{r}_m, \vec{r}_{p^o})}{\partial n_{p^o}} [U^+(p^o) - U^-(p^o)]] dS_{p^o} \end{aligned} \quad (3-32)$$

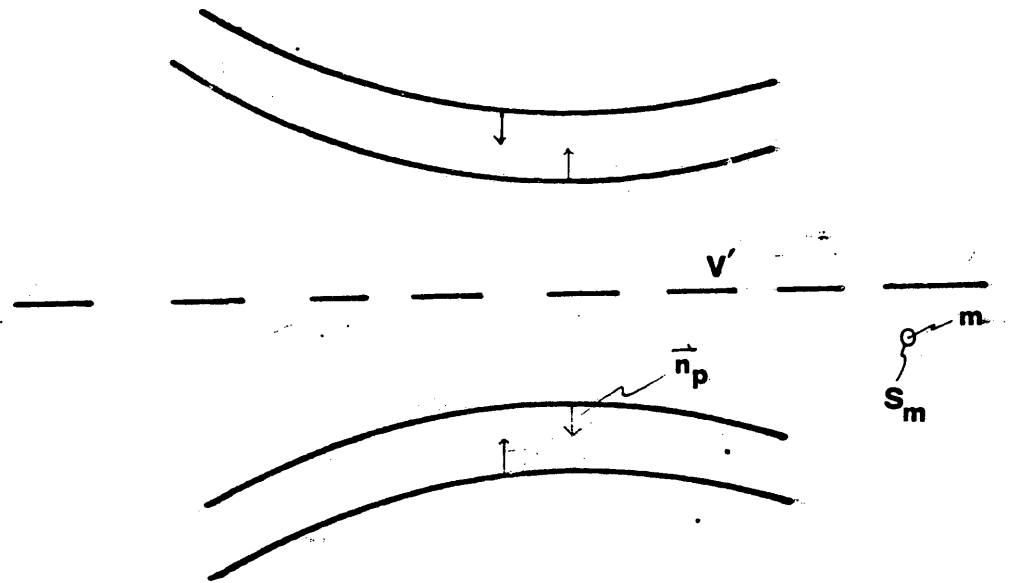


Fig.5: The normal directions at points on the boundaries.

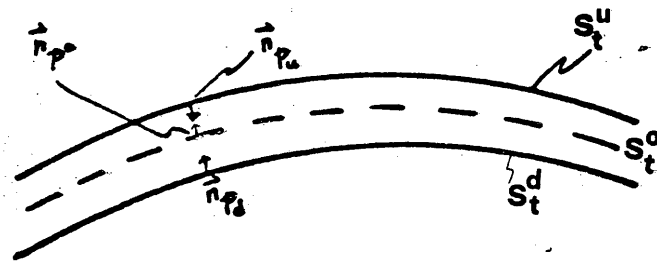


Fig.6: The normal direction at a point on the mathematic boundary.

From the boundary conditions of Eq.(3-14) and (3-15), the integral becomes:

$$\begin{aligned} \oint_{S_t} &= \int_{S_{t^{\circ}}} [U^+(p^{\circ}) - U^-(p^{\circ})] \frac{\partial G(\vec{r}_m, \vec{r}_{p^{\circ}})}{\partial n_{p^{\circ}}} d S_{p^{\circ}} \\ &= \frac{1}{4\pi} \int_{S_{t^{\circ}}} \frac{T}{\rho_e} \frac{\partial U^+(p^{\circ})}{\partial n_{p^{\circ}}} \frac{\partial}{\partial n_{p^{\circ}}} \left(\frac{1}{r_{mp^{\circ}}} \right) d S_{p^{\circ}} \quad (3-33) \end{aligned}$$

Similarly we can get the integral over S_t as

$$\oint_{S_t} = \frac{1}{4\pi} \int_{S_{t^{\circ}}} \frac{T}{\rho_e} \frac{\partial U^e(p^{\circ})}{\partial n_{p^{\circ}}} \frac{\partial}{\partial n_{p^{\circ}}} \left(\frac{1}{r_{mp^{\circ}}} \right) d S_{p^{\circ}} \quad (3-33)$$

Now substitute Eq.(3-34), (3-33), (3-29), (3-28), (3-26)

into (3-22). We get

$$\begin{aligned} U(m) &= \frac{I\rho_1}{4\pi} \left(\frac{1}{r_{Am}} + \frac{1}{r_{Am}} \right) + \frac{1}{4\pi} \int_{S_{t^{\circ}}} \frac{T}{\rho_e} \frac{\partial U^e(p^{\circ})}{\partial n_{p^{\circ}}} \frac{\partial}{\partial n_{p^{\circ}}} \left(\frac{1}{r_{mp^{\circ}}} \right) d S_{p^{\circ}} \\ &+ \frac{1}{4\pi} \int_{S_{t^{\circ}}} \frac{T}{\rho_e} \frac{\partial U^e(p^{\circ})}{\partial n_{p^{\circ}}} \frac{\partial}{\partial n_{p^{\circ}}} \left(\frac{1}{r_{mp^{\circ}}} \right) d S_{p^{\circ}} \quad (3-35) \end{aligned}$$

which is the expression for the electric potential at point m in V' in terms of the primary field and the normal derivative of the electric potential over all the boundaries.

Integral Equation For the Areal Dipole Moment Density

In Eq.(3-35), let us set

$$s(p) = \frac{T}{\rho_e} \frac{\partial U^e(p)}{\partial n_p}$$

Then, ζ can be explained as a secondary source due to the existence of the imperfect thin layer. Recall that the potential, in electrostatic unit, at point m due to a dipole moment $\vec{\eta}$ at point p is

$$\begin{aligned} U &= \vec{\eta} \cdot \nabla \left(\frac{1}{r_{mp}} \right) \\ &= \eta \frac{\partial}{\partial n_p} \left(\frac{1}{r_{mp}} \right) \end{aligned} \quad (3-37)$$

where \vec{n}_p is the unit vector along $\vec{\eta}$ and the magnitude of is η . Thus our secondary sources on S_t , S_t^* are actually dipole sources.

Substituting Eq.(3-36) into (3-35), we get

$$\begin{aligned} U(m) &= \frac{I\rho}{4\pi} \left(\frac{1}{r_{Am}} + \frac{1}{r_{AM}} \right) + \frac{1}{4\pi} \int_{S_{t^*}} \xi(p^*) \frac{\partial}{\partial n_{p^*}} \left(\frac{1}{r_{p^*m}} \right) dS_{p^*} \\ &+ \frac{1}{4\pi} \int_{S_t} \xi(p) \frac{\partial}{\partial n_p} \left(\frac{1}{r_{pm}} \right) dS_p \end{aligned} \quad (3-38)$$

For m near but not on S_t^* we can take the normal derivatives of Eq.(3-38) with respect to the observation point m , and we can differentiate under the integral. Thus Eq.(3-38) becomes

$$\begin{aligned} \xi(m) &= \frac{T}{\rho_e} \frac{I\rho_e}{4\pi} \frac{\partial}{\partial n_m} \left(\frac{1}{r_{Am}} + \frac{1}{r_{AM}} \right) + \frac{1}{4\pi} \int \frac{T}{\rho_e} \xi(p^*) \\ &\frac{\partial^2}{\partial n_{p^*} \partial n_m} \left(\frac{1}{r_{mp^*}} \right) dS_{p^*} + \frac{1}{4\pi} \int_{S_t} \frac{T}{\rho_e} \xi(p) \frac{\partial^2}{\partial n_{p^*} \partial n_m} \left(\frac{1}{r_{mp}} \right) dS_p \end{aligned}$$

Note that from physical point of view Eq.(3-39) is equivalent to

$$\zeta(m) = \frac{T}{\rho_e} E(m)$$

where $E(m)$ is the normal component of the electrical field at point m , which is due to the primary sources and the dipole moment distributed on the layer.

In numerical solution, we divide the layer into rectangular facets and use the step approximation that the dipole moment density is constant on each facet. There is a singularity in Eq.(3-39) as point m approaches S_i . Physically, it means that we are going to calculate the normal component of the electrical field at point m located on a facet distributed with dipole moment. If the facet is rectangle, this computation can be expressed in a closed form as we will see in chapter 6 and appendix 3 for the numerical computation.

Eq.(3-39) is a Fredholm integral equation of the second kind. Once it is solved for ζ , the electrical potential at any point in V can be expressed by Eq.(3-35) with ζ , the dipole moment density, being substituted for $\frac{T \partial U}{\rho \partial n}$.

CHAPTER 4: PERFECT THIN INSULATOR

For a perfect thin insulator which has the transverse resistance of infinity, it is shown in this chapter that the secondary sources can still be considered as dipoles. However, if the thin layer is infinity extended, the potential field in the first layer can be obtained through three different ways.

Boundary Conditions

There is no current flowing across the perfect thin insulator. Hence it is apparent that one of the boundary condition should be

$$\frac{\partial U(m^+)}{\partial n} = \frac{\partial U(m^-)}{\partial n} = 0 \quad (4-1)$$

Two other boundary conditions remain true here. They are

$$\left. \frac{\partial U}{\partial n} \right|_{z=0} = 0 \quad (4-2)$$

$U \rightarrow \frac{1}{4\pi} \frac{I\rho_i}{R}$ as the observation point approaches the source. When the layer is infinity extended, the third layer can be considered as a perfect conductor compared with the resistivity of the intermediate layer. Recall that there is no electrical field inside a perfect conductor. The boundary condition below the infinity extended layer is

that the electrical field vanishes.

Mathematical Model for Imperfect Thin Insulator

Consider a single sheet distributed with dipole moments, as shown in Fig.A, which has been proposed for the mathematical model of an imperfect thin insulator. At points m^+ and m^- , the normal component of the secondary electrical fields are continuous. Furthermore, the normal component of the primary electrical fields are continuous since the distance between the primary source and the layer is assumed to be much greater than the thickness of the layer. Note that the direction of the normal component of the primary field is opposite to that of the secondary field. For the perfect thin insulator case, the normal component of the secondary field is strong enough to cancel that of the primary field.

Mathematical Models for Perfect Thin Insulator of Infinite Extent

Consider an infinitely extended perfect thin insulator. Since there is no current flowing across the thin layer, the current density distribution in the first layer must be the same as that for the two-layer case with the second layer being perfect insulating, as shown in Fig.B. The potential

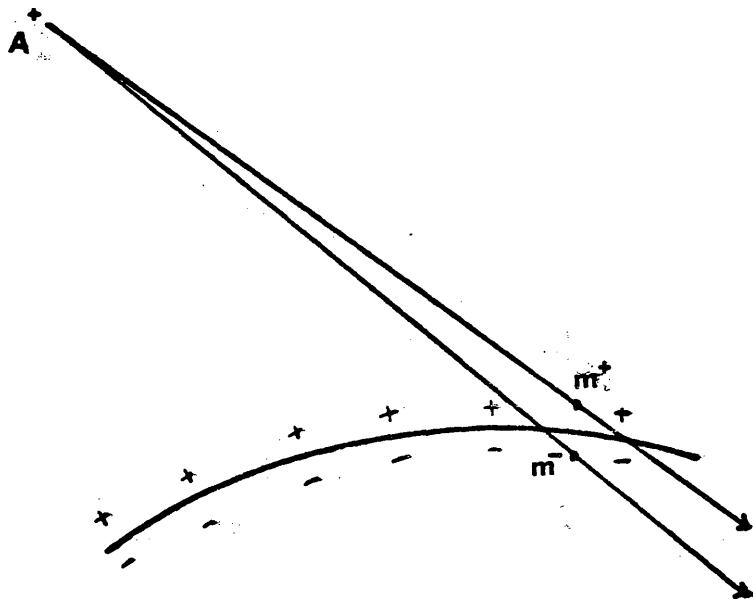


Fig. A The mathematic model for an imperfect thin conductor.

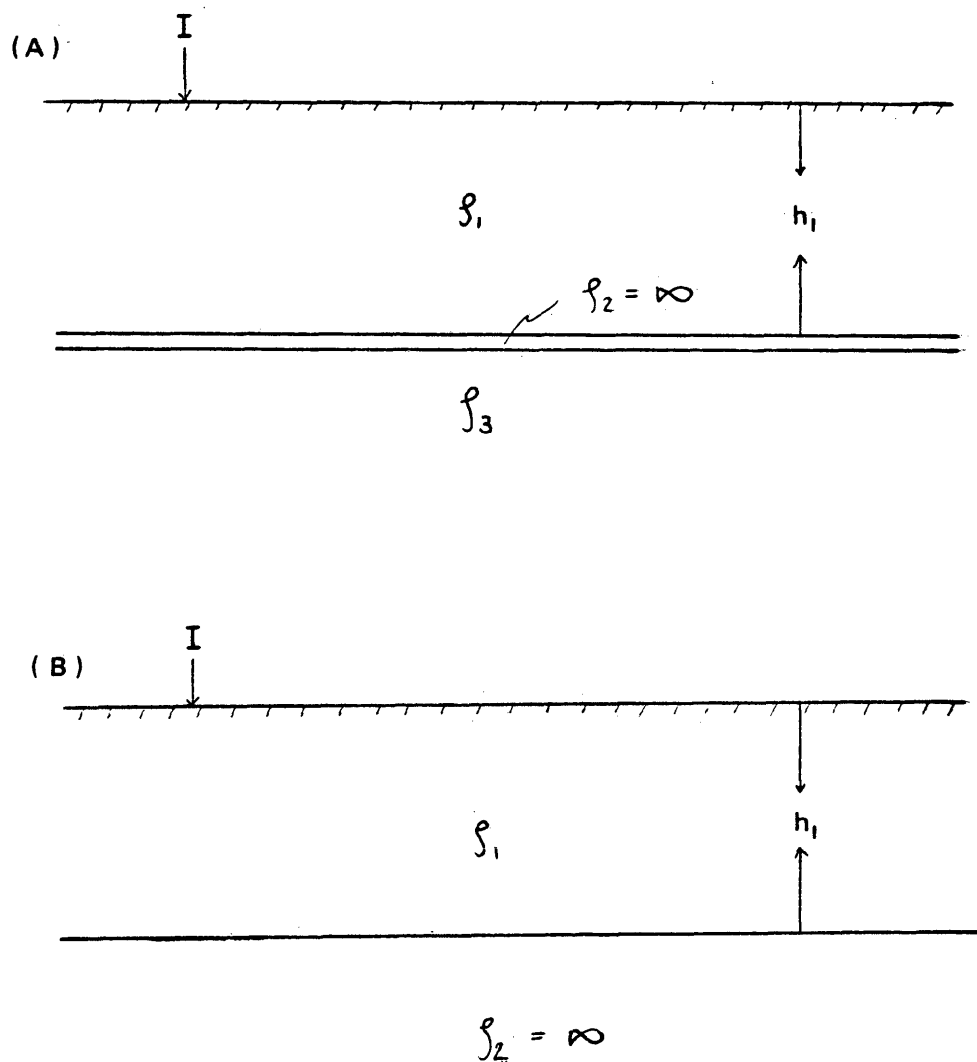


Fig. B The current density distribution in the first layer must be the same for case (A) and case (B). In case (A), there is a perfect insulating intermediate layer. In case (B), the second layer is perfectly insulating.

T-2231

fields in the first layer are thus the same for both cases.

The potential in the first layer can then be obtained either through Eq.(3-38) and (3-39) for the thin insulator case with T being infinity, or through Eq.(2-5) and (2-6) for the two-layer case with K being unity. In chapter 5, we will see that the potential field can also be obtained through Eq.(5-1) and (5-4). From the uniqueness of the boundary value problem (Stratton, 1941), the solutions of these three methods must be the same. If it is solved through Eq.(2-5) and (2-6) with K being unity, the secondary sources can be considered as charges while for the other two cases they are dipoles. They must create the same field in the first layer.

CHAPTER 5: MODELING WITH IRREGULAR EARTH SURFACE

When a direct-current resistivity survey is conducted over an irregular surface, the anomalies produced by topography effects might lead to erroneous interpretations. In Fox's paper (p. 13-14, 1978), the correction factors, or the geometric factors for the apparent resistivity over an irregular surface are calculated through the modeling of a homogeneous earth with irregular surface by the finite element method. However, since the secondary sources induced along the discontinuity interact among themselves as we can see from the integral equations for all kinds of sources in the preceding chapters, the corrections for the topography effects for apparent resistivity are not like that for the gravity and magnetic survey which have static sources. Actually, up to now, there are no papers published for exact ways to correct apparent resistivity data taken over an irregular surface. The correction method of Fox's (1978) has some restrictions as shown in his paper. Therefore, it is will be helpful to be able to model the direct current field over an irregular earth surface in order to compare with the field data, so that topography effects can be identified, and possibly removed.

T-2231

It is shown in this chapter that the potential at any point inside the earth can be expressed in terms of the potentials over the irregular earth surface and in terms of the charges over the boundaries of the body buried. It can be seen that the potential due to the sources along the earth surface are equivalent to dipole sources.

Again, as we have done in the preceding chapters, we start with the Green's Identity and apply the boundary conditions to get the expression for the field and the equations for the sources.

Integral Equation for the Potential on the Irregular Surface
Homogeneous Earth Case

In this case we consider the inner space as in the medium surrounded by the irregular surface as shown in Fig. 7. The potential at any point in the inner space can then be expressed by

$$\begin{aligned} U(m) &= \frac{I \rho_1}{4\pi} \frac{1}{r_{Am}} + \frac{1}{4\pi} \int_S \left[\frac{\partial U(p')}{\partial n_p} \frac{1}{r_{pm}} - U(p') \frac{\partial}{\partial n_p} \frac{1}{r_{pm}} \right] dS_p \\ &= \frac{I \rho_1}{4\pi} \frac{1}{r_{Am}} - \frac{1}{4\pi} \int_S U(p') \frac{\partial}{\partial n_p} \frac{1}{r_{pm}} dS_p \end{aligned} \quad (5-1)$$

for $\frac{\partial U}{\partial n} = 0$ on S

If point A is on the surface, the boundary condition tells us that the potential at point p is then

$$U(p) \rightarrow \frac{I \rho_1}{4\pi r_{Ap}} \quad \text{as } p \rightarrow A \quad (5-2)$$

The integral in the expression for the potential, Eq.(5-1) thus contains a singularity at point A. However we see that potential increases to infinity as r approaches zero with an order of minus one, while the area around point A is proportional to r with an order of two. The interacting factor over this small area can be considered as constant. The integration over this small area around point A is then zero. So we can delete point A from the integration region in the Eq.(5-1). We get

$$U(m) = \frac{I \rho_1}{4\pi} \frac{1}{r_{Am}} - \frac{1}{4\pi} \int_{S'} U(p) \frac{\partial}{\partial n_p} \frac{1}{r_{pm}} dS_p \quad (5-3)$$

where S' represents S with point A being deleted.

Let point m approach the surface S. We get the expression for the potential at a point on S in terms of the potentials at points on S other than points A and m. That is an integral equation for the potential over the surface S.

$$U(m) = \frac{I \rho_1}{2\pi} \frac{1}{r_{Am}} - \frac{1}{2\pi} \int_{S'} U(p) \frac{\partial}{\partial n_p} \frac{1}{r_{pm}} dS_p \quad (5-4)$$

where S^* represents S with points A and m being deleted.

Buried Body Case

The model considered in this case can be shown typically in Fig. 8, where we have an irregular earth surface. To apply the Green's Identity, Eq.(3-22), we consider the inner space of the model shown in Fig. as the space surrounded by the surface S_b^u , S_b^d , S_e as shown in Fig. 9. S_b^u and S_b^d are the surfaces surrounding and approaching S_b , which is the boundary of the buried body. S_e is the irregular earth surface.

Assuming the source point A is located on the earth surface. The potential at any point inside the space can be expressed by

$$U(m) = \frac{I \rho_l}{4\pi} \frac{1}{r_{Am}} - \frac{1}{4\pi} \int_{S_b^u} U(p) \frac{\partial}{\partial n_p} \frac{1}{r_{pm}} dS_p + \frac{1}{4\pi} \int_{S_b^d} \sigma(p) \frac{1}{r_{pm}} dS_p \quad (5-5)$$

where S_e' represents S_e with point A being deleted, and

$$\sigma(p) = \frac{\partial U^-(p)}{\partial n} - \frac{\partial U^+(p)}{\partial n} \quad (5-6)$$

which is physically the charge distribution at point p .

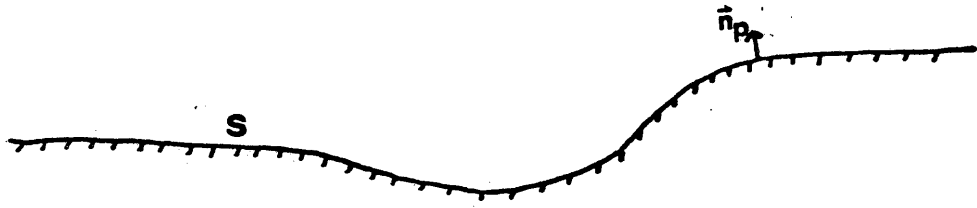


Fig. 7: Physical model for an homogeneous earth with irregular earth surface.

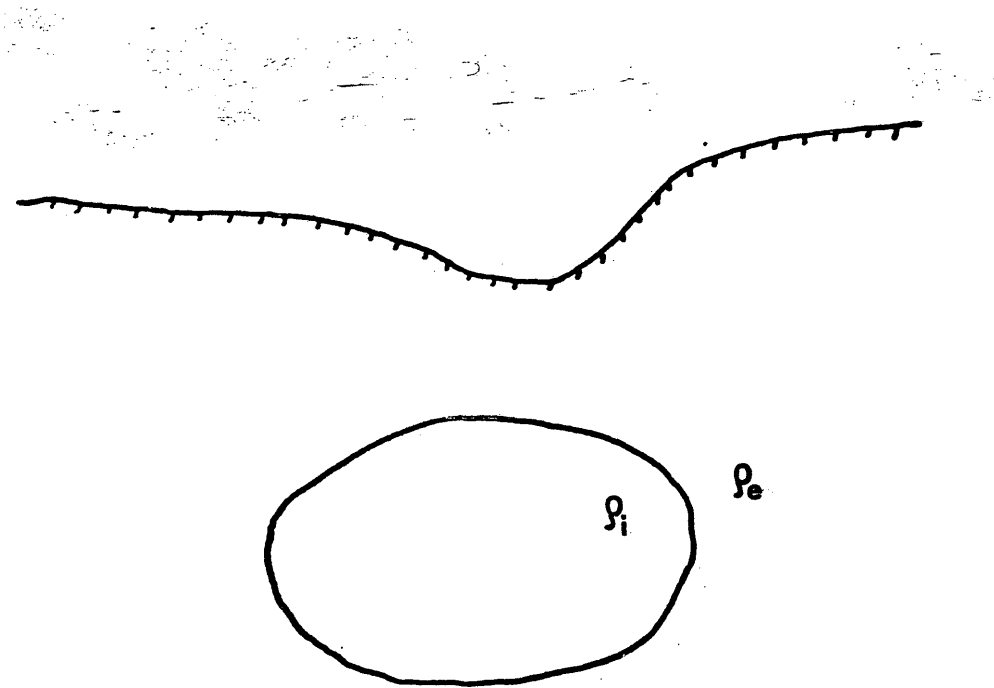


Fig. 8: Physical model of a buried body with irregular earth surface.

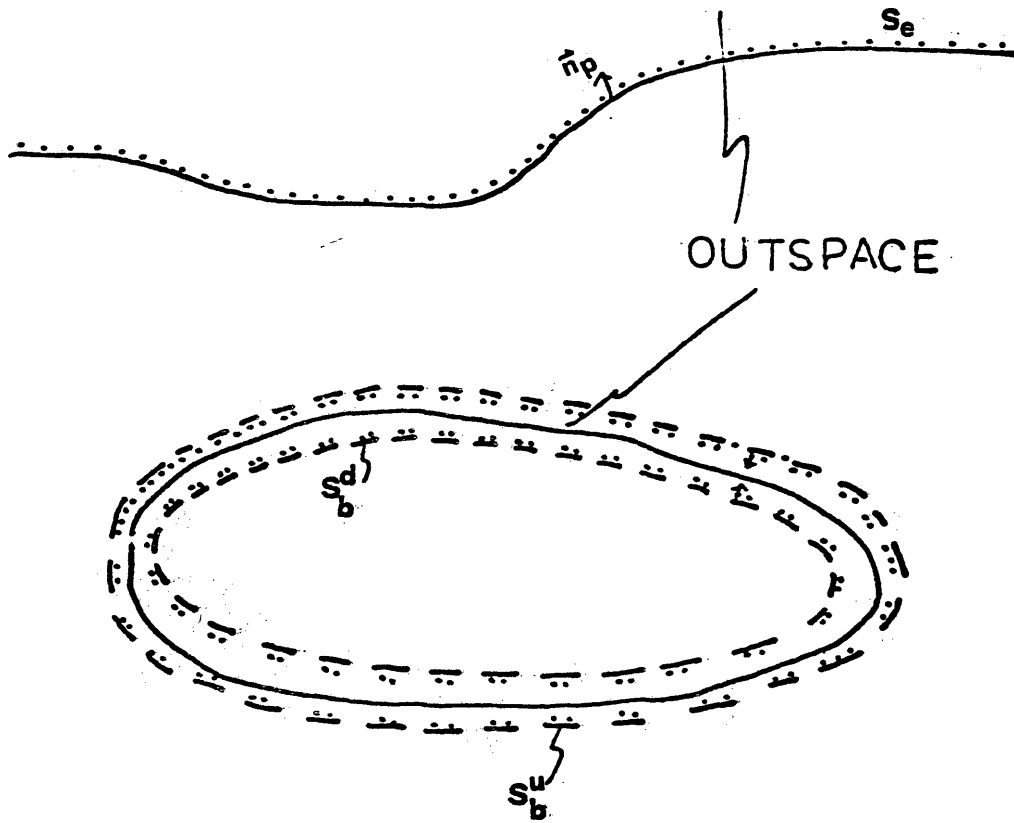


Fig. 9: Model shows the inner space proposed and the normal directions of the surface.

Let m approach S_e . We get the expression for the potential at point m on S_e in terms of the potentials due to the charges on S_b .

$$U(m) = \frac{I \rho_1}{2\pi} \frac{1}{r_{Am}} - \frac{1}{2\pi} \int_{S_e^*} U(p) \frac{\partial}{\partial n_p} \frac{1}{r_{pm}} dS_p + \frac{1}{2\pi} \int_{S_b} \sigma(p) \frac{1}{r_{pm}} dS_p \quad (5-7)$$

where S_e^* represents S_e with points A and m being deleted.

Let m^+ be the point at S_b^u , m^- be the point at S_b^d and let m^+ approach m^- . Applying the boundary condition that the normal component of the current density be continuous through S_b , we get

$$\sigma(m) = \frac{I \rho_1 K}{2\pi} \frac{\partial}{\partial n_m} \frac{1}{r_{Am}} - \frac{K}{2\pi} \int_{S_e'} U(p) \frac{\partial^2}{\partial n_p \partial n_m} \frac{1}{r_{pm}} dS_p + \frac{K}{2\pi} \int_{S_b'} \sigma(p') \frac{\partial}{\partial n_m} \frac{1}{r_{p'm}} dS_{p'} \quad (5-8)$$

where m is at S_b

$$K = \frac{\rho_3 - \rho_1}{\rho_3 + \rho_1}$$

S_b' represents S_b with point m being deleted.

Thus, solving the integral equations, Eqs.(5-7) and (5-8), we will be able to get the potential at any point on the earth's surface.

CHAPTER 6: SOLUTIONS OF INTEGRAL EQUATIONS

In the preceding chapters, the field of any model being considered is expressed by a term regarding to the primary source in addition to an integration regarding to the secondary sources over the discontinuities of our mathematical models. If we know the types and the values of all the sources, the calculations of the field at any point inside the space of the model includes two parts. The first part is equivalent to solve the integral equation for the secondary sources. The second part is to calculate the field due to the secondary net charges or the secondary dipoles at the discontinuities of our mathematical models. The secondary source for any model shown in the preceding chapters are in the Fredholm integral equations of the second kind. That is, the sources at any point along the discontinuities of our mathematical model are induced by the primary sources and interact with the other secondary sources.

All the integral equations shown in this paper can be represented by the following form which is the Fredholm integral equation of the second kind:

$$f(m) = f_0(m) + v \int_S f(p)K(m,p) dp \quad (6-1-1)$$

where $K(m,p)$ is the kernel or the interacting factor, $f_0(m)$ is the source of the zero order induced at point m by the primary sources and v is some electric parameter. There are two different kinds of zero order induced sources and two different kinds of interacting factors in integral equations mentioned in this paper. They are developed into more programmable forms in the following two sections. The numerical method for solving these integral equations is also discussed.

The Zero Order Terms

The zero order terms represent the interaction from the primary sources. The first type of those appearing in Eqs. (2-6) and (3-39) is related to

$$\begin{aligned} f_0^1(m) &= \frac{\partial}{\partial n_m} \left(\frac{1}{r_{AM}} + \frac{1}{r_{AM}} \right) = \left[\nabla_m \frac{1}{r_{AM}} + \nabla_m \frac{1}{r_{AM}} \right] \cdot \vec{n}_m \\ &= \left[\frac{\vec{r}_{AM}}{r_{AM}^3} + \frac{\vec{r}_{AM}}{r_{AM}^3} \right] \cdot \vec{n}_m \end{aligned} \quad (6-1)$$

where \vec{r}_{AM} points from point m to point A

\vec{r}_{AM} points from point m to point A

The second type of the zero term appear in the integral equation of the topography effect is related to:

$$f_0^2(m) = \frac{1}{r_{AM}} \quad (6-2)$$

The above terms are in programmable forms.

Interacting Factors

If we consider the image terms, Eq.(6-1-1) becomes

$$f(m) = f_0(m) + \nu \int_{S'} f(p) K(m,p) dSp + \nu \int_S f(p) K(m,p) dSp \quad (6-3)$$

where S' represents the image of S as shown in Fig. 1, page 8.

$$f(p) = f(\underline{p})$$

we can combine the kernel in Eq.(6-3) and get $f(p) = f(p)$

Since

$$f(m) = f_0(m) + \nu \int_S f(p) K^*(m,p) dSp \quad (6-4)$$

where

$$K^*(m,p) = K(m,p) + K(m,\underline{p}) \quad (6-5)$$

The first kind of the kernel appearing in Eq.(2-6) is

$$K_1^*(m,p) = \frac{\partial}{\partial n_m} \left(\frac{1}{r_{p^0 m}} + \frac{1}{r_{\underline{p}^0 m}} \right) = \left[\frac{\vec{r}_{p^0 m}}{r_{p^0 m}^3} + \frac{\vec{r}_{\underline{p}^0 m}}{r_{\underline{p}^0 m}^3} \right] \cdot \vec{n}_m, \quad p^0 \neq m$$

and

$$K_1^*(m,p) = \frac{\partial}{\partial n_m} \frac{1}{r_{\underline{p}^0 m}} = \frac{\vec{r}_{\underline{p}^0 m}}{r_{\underline{p}^0 m}^3} \cdot \vec{n}_m, \quad p^0 = m \quad (6-6)$$

The second kind of kernels appearing in Eq.(3-39) is

$$\begin{aligned}
 K_2^*(m,p) &= \frac{\partial}{\partial n_m} \left[\frac{\partial}{\partial n_{p^0}} \frac{1}{r_{p^0 m}} + \frac{\partial}{\partial n_{p^0}} \frac{1}{r_{p^0 m}} \right] \\
 &= - \frac{3(\vec{r}_{p^0 m} \cdot \vec{n}_{p^0})(\vec{r}_{p^0 m} \cdot \vec{n}_m)}{r_{p^0 m}^5} + \frac{\vec{n}_{p^0} \cdot \vec{n}_m}{r_{p^0 m}^3} \\
 &\quad - \frac{3(\vec{r}_{p^0 m} \cdot \vec{n}_{p^0})}{r_{p^0 m}^5} (\vec{r}_{p^0 m} \cdot \vec{n}_m) + \frac{\vec{n}_{p^0} \cdot \vec{n}_m}{r_{p^0 m}^3}, \quad p^0 \neq m \\
 K_2^*(m,p) &= - \frac{3(\vec{r}_{p^0 m} \cdot \vec{n}_{p^0})(\vec{r}_{p^0 m} \cdot \vec{n}_m)}{r_{p^0 m}^5} + \frac{\vec{n}_{p^0} \cdot \vec{n}_m}{r_{p^0 m}^3} \quad p^0 = m \quad (6-7)
 \end{aligned}$$

The kernel appearing in the integral equation with the topography effects include two types. One is the same as $K_1^*(m,p)$ with no image part. The other is the same as $K_2^*(m,p)$ with no image part.

From the above, the integral equations can be organized into programmable equations.

Numerical Method

Successive approximation method

The numerical method applied in this paper for solving the integral equations for the arbitrarily shaped body case and the topography effect case is the successive approximation method. This method has certain advantages

over the simultaneous equation method. By applying the successive method, the dimension of the computer storage is much less than that required by the simultaneous equation method. If the buried bodies are rather smooth in geometry, the results from the successive method are usually accurate enough. The advantages allow us to program for multiple body or huge body cases. If we do have a complicated geometry, it will be better to smooth the geometry. To see if the method is applicable to a specific model, the series of the solution is inspected by Shank's transform (1955) to test and/or force convergence.

The numerical solution for the integral equation, Eq.(6-4) involving only one type of secondary sources is

$$f(m) = f_0(m) + \nu f_1(m) + \nu^2 f_2(m) + \dots \quad (6-8)$$

where

$$f_n(m) = \int_S f_{n-1} K^*(m,p) dS \quad (6-9)$$

There are simultaneous integral equations for the buried body with irregular surface case. Let these equations be

$$f(m) = f_0(m) + \nu_1 \int_{S_1} f(p) K_1^*(m,p) dS_1 \quad (6-10)$$

$$+ \nu_1 \int_{S_2} g(p) K_2^*(m,p) dS_2$$

$$g(m) = g_0(m) + \gamma_2 \int_{s_1} f(p) K_1^*(m,p) dS_1 + \gamma_2 \int_{s_2} g(p) K_2^*(m,p) dS_2 \quad (6-11)$$

For solving the above two equations by the successive method, let

$$\gamma_2 = k \gamma_1 \quad (6-12)$$

$$\text{and } f(m) = \gamma_1^n f_n(m) \quad (6-13)$$

$$g(m) = k \gamma_1^n g_n(m) \quad (6-14)$$

Substituting Eqs.(6-13) and (6-14) into Eqs.(6-10) and (6-11), we obtain the n-th order ones in terms of the (n-1)-th order terms as follows:

$$g_n = \int_{s_1} f_{n-1}(p) K_1^*(m,p) dS_1 + \gamma_1^{n-1} \int_{s_2} g_{n-1}(p) K_2^*(m,p) dS_2 \quad (6-15)$$

$$f_n = \frac{1}{\gamma_1^{n-1}} g_n \quad (6-16)$$

In our numerical solutions, the bodies are simulated by plane facets. Assuming the step approximation of the solution on each facet, Eq.(6-15) can then be put into a matrix form as

$$g_n = [\tilde{K}_1^*] f_{n-1} + \gamma_1^{n-1} [\tilde{K}_2^*] g_{n-1} \quad (6-17)$$

$$\text{where } g_n = \begin{bmatrix} g_n(1) \\ \vdots \\ g_n(N) \end{bmatrix} \quad f_n = \begin{bmatrix} f_n(1) \\ \vdots \\ f_n(N) \end{bmatrix}$$

$$\text{and } [\tilde{K}_1^*(m,p)] = \left[\int_{s_1} \tilde{K}_1^*(m,p) dS_1 \right] \quad (6-18)$$

$$[\tilde{K}_2^*(m,p)] = \left[\int_{s_2} \tilde{K}_2^*(m,p) dS_2 \right]$$

N is the total number of the facets.

The solutions of the integral equations are expanded into series. The series are transformed by a nonlinear second order transformation (Shanks, 1955) to test and/or force convergence.

Simultaneous Equation Method

The insulating factor, T , in the integral equation for the imperfect thin insulator can be infinite. It is thus improper to use the successive method to solve the integral equation involving with large T value.

In our numerical solutions, the bodies are simulated by plane facets. Assuming that on each facet the charges or the dipole moments are constant, the integral equations can be put into a matrix form as follows

$$\bar{K}(m,p) \vec{f} = \vec{f}_0 \quad (6-15)$$

where

$$\vec{f} = \begin{bmatrix} f(1) \\ \vdots \\ f(N) \end{bmatrix} \quad \vec{f}_0 = \begin{bmatrix} f_0(1) \\ \vdots \\ f_0(N) \end{bmatrix}$$

and

$$\bar{K}(m,p) = \left[\int K * (m,p) dS \right]$$

The diagonal terms of $\bar{K}(m,p)$ play an important role for solving the above simultaneous equations, which involve singularity terms in the integral equation. The singularities in the integral equations for arbitrarily shaped bodies and topography effects have been solved in the respective chapter. The singularities in the integral equations of the thin layer cases will be discussed in the next section.

Step Approximation

In both of the numerical methods, we use step approximation. That is the charges or the dipole moments are uniform on each facet. Eq.(6-4) thus becomes

$$f(m) = f_o(m) + \sum_{n=1}^N v f(n) \int_{S_n} K^*(m,p) dS_n \quad (6-21)$$

$m \leq N$

The kernel are expressed in more programmable forms as shown in Eq.(6-6) and (6-7). For the terms involving $\vec{r}_{pm} \cdot \vec{n}_m$ in the kernels, the integral in Eq.(6-21) can be approximated by

$$K^*(m,p_c) \Delta S_p \quad (6-22)$$

This approximation is very conservative regarding computation time and the solutions are accurate enough if the value for

$$\frac{\vec{r}_{pm} \cdot \vec{n}_m}{r_{pm}^3}$$

(6-23)

is not too large, i.e., the geometry of the bodies to be modeled is not too complicated.

For the second and the third kinds of kernels, the integral in Eq.(6-21) involves an integration as follows

$$\int_{S_n} \frac{1}{r_{pm}} ds \quad (6-24)$$

Numerical evaluation of the integral is possible. But it might cause erroneous results for those facets close to point m. If S is a rectangle, the integration for Eq.(6-24) can be expressed in a closed form as shown in Appendix 3. There is a singularity in the integral if m is on S. The singularity is solved as a special case of Appendix 3. One thing important is that the direction of the normal component of the electrical field at point m due to the singularity facet is opposite to that of the facets adjacent to point m.

CHAPTER 7: THE SECOND VERTICAL DERIVATIVE OF THE POTENTIAL

A modified receiver array is applied to enhance the signal from the thin disk. The array is shown to be related to the second vertical derivative of the potential and hence has the ability to delineate the high spacial harmonic signals which are mainly from our confined targets.

If we compute the potential at any point m , due to a current source at A in the vicinity of an arbitrarily shaped body or thin insulator, we can use the principle of superposition to calculate the second vertical derivative. The scalar potential functions for different electrode positions may be added algebraically.

From the Laplace equation

$$\nabla^2 U = 0 \quad (A4-1)$$

the second vertical derivative can be obtained by

$$\frac{\partial^2 U}{\partial z^2} = - \left(\frac{\partial^2 U}{\partial x^2} + \frac{\partial^2 U}{\partial y^2} \right) \quad (A4-2)$$

If we calculate the potential at the five points as shown in Fig. 9-1, the second vertical derivative can be approximated by

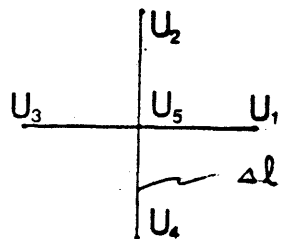
$$\frac{\partial^2 U}{\partial z^2} = \frac{1}{(\Delta l)^2} (U_1 + U_2 + U_3 + U_4 - 4U_5) \quad (A4-3)$$


Fig. 9-1

The true second vertical derivative is the case when Δl approaches zero. In application, the choice of Δl will depend on the depth of the target. Since Δl does not approach zero, we do not obtain the true second vertical derivative. However, we will still use this term since the arrays contain the ability to delineate the high spacial harmonic signals which are from the confined targets and since the second vertical derivative is actually a high pass filter.

In the field, we measure the potential differences at the four points with respect to the center as shown in Figure 7-2. The second vertical derivative is calculated by

$$\frac{\partial^2 U}{\partial Z^2} = \frac{\Delta U_{x_1} - \Delta U_{x_2}}{\Delta x} + \frac{\Delta U_{y_1} - \Delta U_{y_2}}{\Delta y} \quad (A4-4)$$

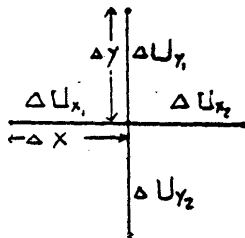
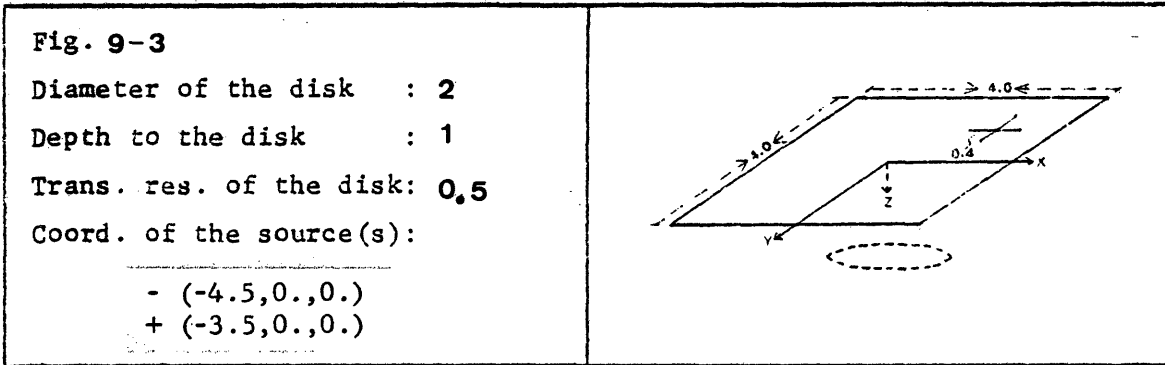
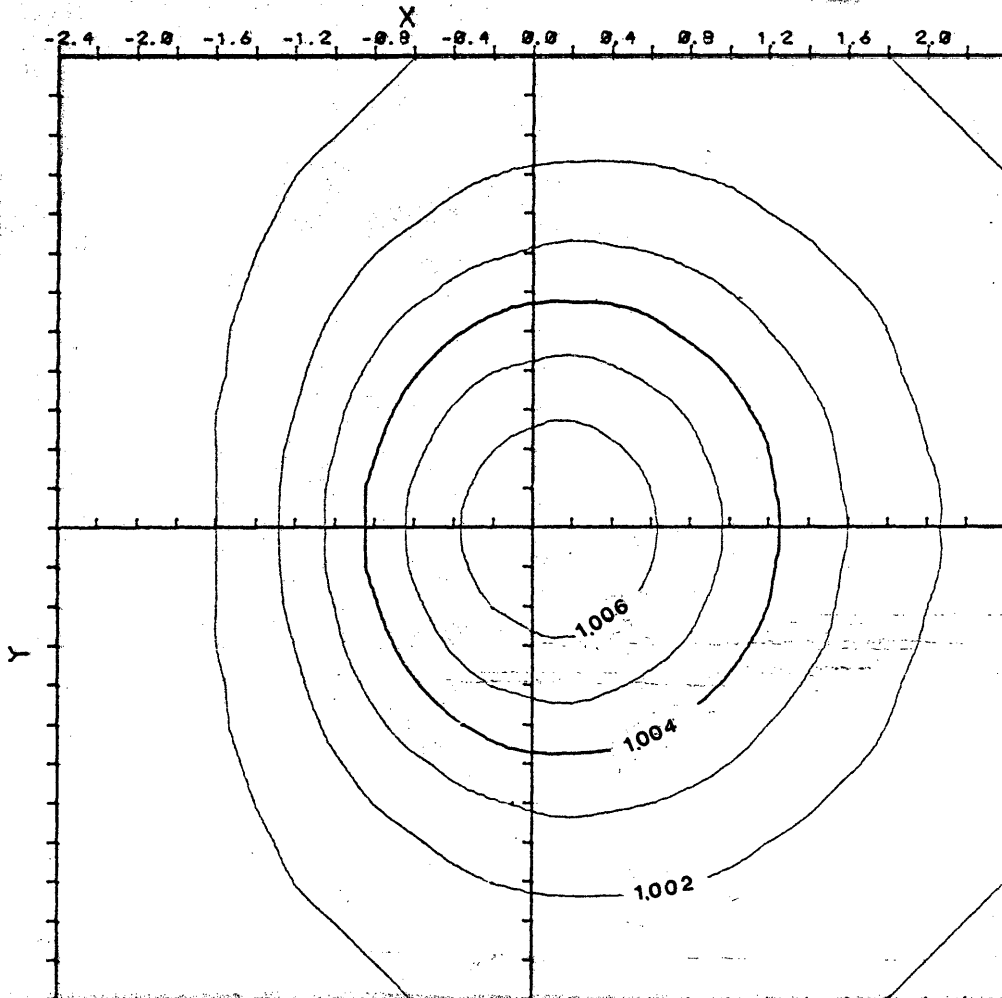


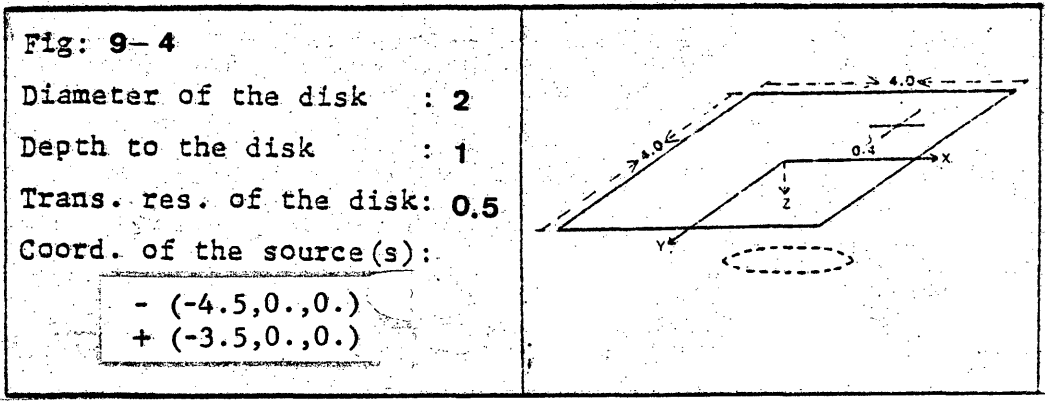
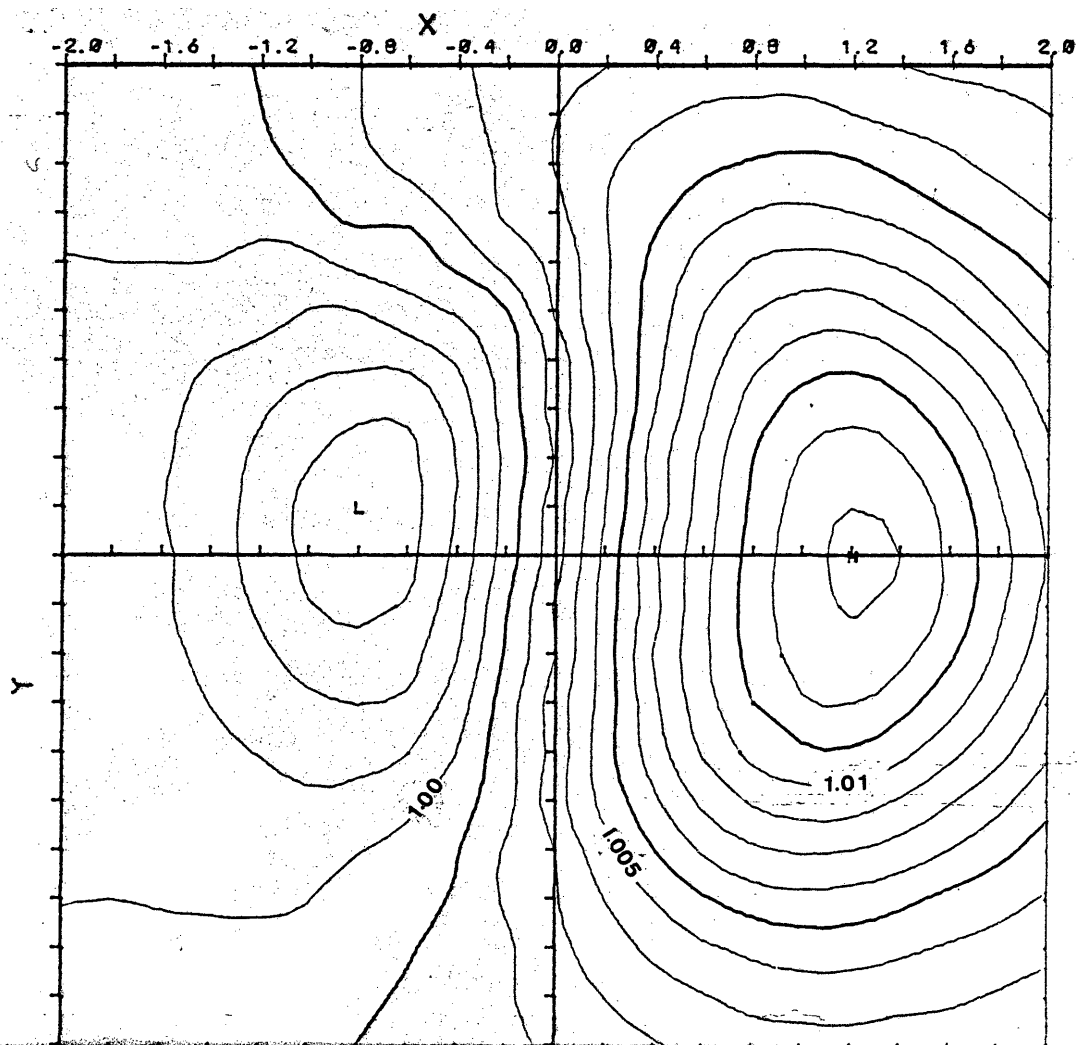
Fig. 9-2

All the computer programs in this thesis compute the potential at any point which is not at the current electrode location and which is not on the surface of the buried body. It will be a simple subroutine to superimpose the potentials for any arrays.

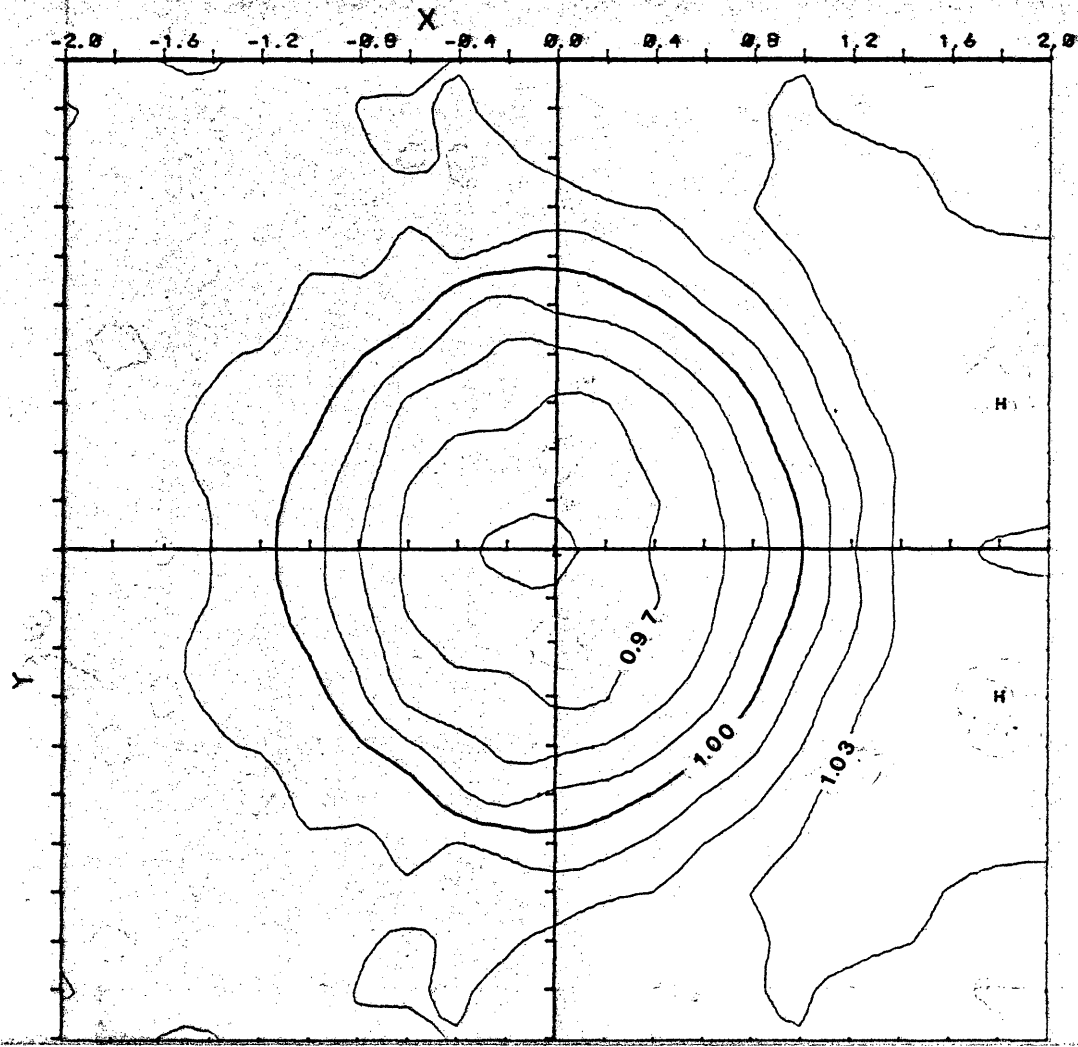
In order to see the enhancement of the signal by measuring the second vertical derivative, we use a thin disk as our model with parameters shown in the figures. Figure 9-3 is the contour map of the normalized total potential. Figure 9-4 is the contour map of the apparent resistivity using dipole receivers. Figure 9-5 is the contour map of the normalized second vertical derivative. The maximum responses of the normalized potential, apparent resistivity and the normalized second vertical derivative are about one percent, 1.6 percents and 8 percents respectively. We see thus the second vertical derivative has the ability to enhance the signal from the thin insulating layer. For this version, we shall use the normalized second vertical derivative to display most of the model results in the subsequent chapters.



Contour map of the normalized total potential for the model shown above.



Contour map of the apparent resistivity for the model shown above.



<p>Fig: 9-5</p> <p>Diameter of the disk : 2</p> <p>Depth to the disk : 1</p> <p>Trans. res. of the disk: 0.5</p> <p>Coord. of the source(s):</p> <p>- (-4.5,0.,0.)</p> <p>+ (-3.5,0.,0.)</p>	
---	--

Contour map of the normalized secondary vertical derivative for the model shown above.

CHAPTER 8: NUMERICAL RESULTS

Three computer programs have been developed. The first one is to model the response of arbitrarily shaped three-dimensional bodies, with the flexibility for multiple reflection coefficients. The second one is to model the response of arbitrarily shaped three-dimensional thin insulators. The third one is to model the topography effects in the electric surveys, which allows us to derive the corrected geometric factor in the three dimensional case.

In this chapter, we will show the accuracy of the programs and discuss the numerical results using the bipole source over some models, especially over imperfect thin insulators which might be oil reservoirs. The second vertical derivatives of the total potentials using the bipole source are normalized by the second vertical derivatives of the primary fields. The possibility of a positive response of an imperfect thin insulator is discussed by investigating these normalized fields.

Arbitrarily Shaped Bodies

In order to test the accuracy of the program which

models the response of arbitrarily shaped three-dimensional bodies with the flexibility for multiple reflection coefficients, we use a two co-original half spheres, as shown in Fig.10, as our testing model. The analytical expression for the potential subjected to an uniform primary field is shown in Appendix 2. From the image theory, the solution is the same as a two co-original spheres subjected to a primary field, which is a simple extension for the solution for one sphere in the whole space case (Stratton, 1941).

In the numerical computations for the testing model, each half sphere is simulated by 40 triangular facets and the potentials are computed along the x axis as shown in Fig. 11. The comparisons of the numerical results with the analytical ones are shown from Fig.12 to Fig.14 for different parameters. The numerical results show that the larger the contrast between the two reflection coefficients, the larger the errors. There are two possibilities for the causes of these errors. One is that the kernel in the integral equation of Eq.(6-21) is approximated by Eq.(6-22). The other is the finite facet simulation. Note that if the vertices of the triangles are located on the sphere, the total areas of the facets are then smaller than that of the

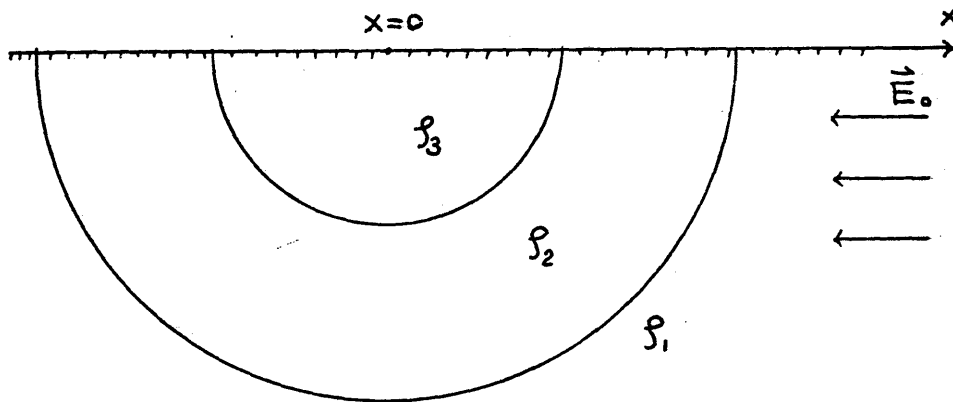


Fig. 10: Two co-original half spheres buried just beneath the surface and subjected to an uniform primary electrical field.

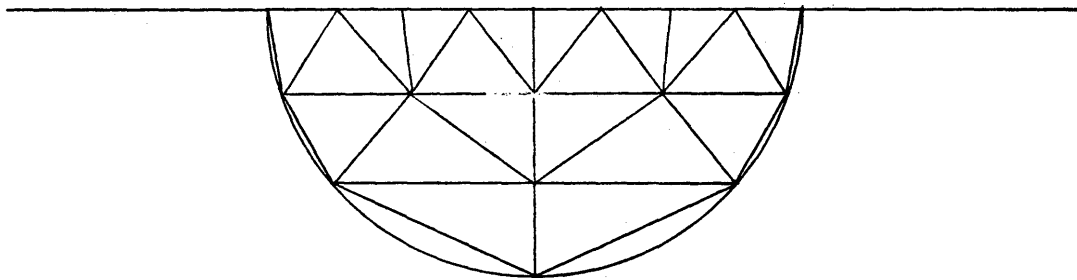


Fig. 11: A half sphere is simulated by 40 triangular facets.

SOLID LINE: ANALYTIC

$D1=.95$, $D2=1.9$, $R1=1.$, $R2=3.$, $R3=9.$

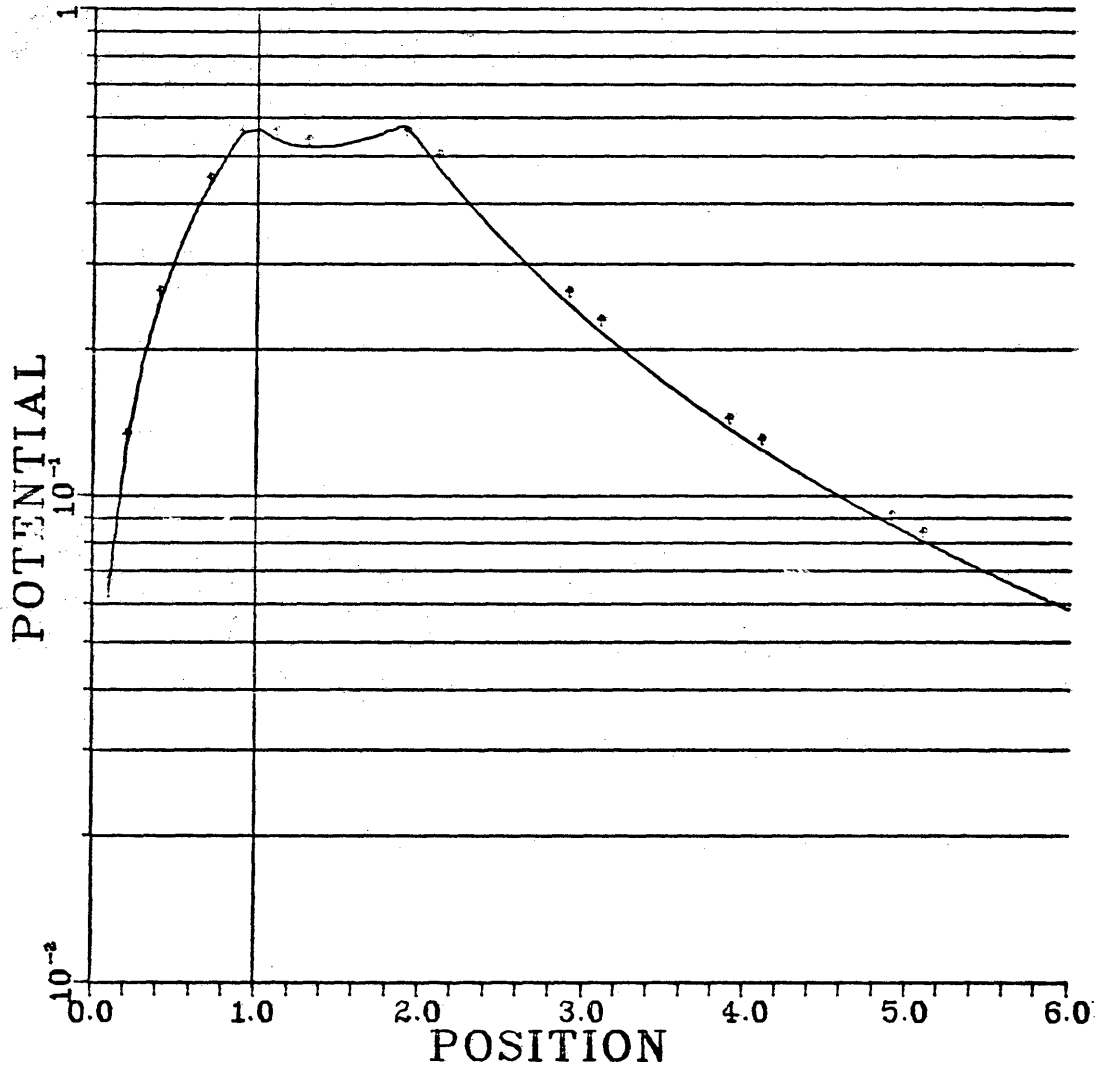


Fig. 12: The symbols represent the numerical results of the modeling for two half spheres with different reflection coefficients. The solid line represents the analytic solution. $D1$ and $D2$ are the radii of the inner sphere and the outer sphere respectively. $R1$, $R2$ and $R3$ are the resistivities of the homogeneous earth, the outer sphere and the inner sphere respectively.

SOLID LINE: ANALYTIC

$D1=.95$, $D2=1.9$, $R1=3.$, $R2=997.$, $R3=2992.$

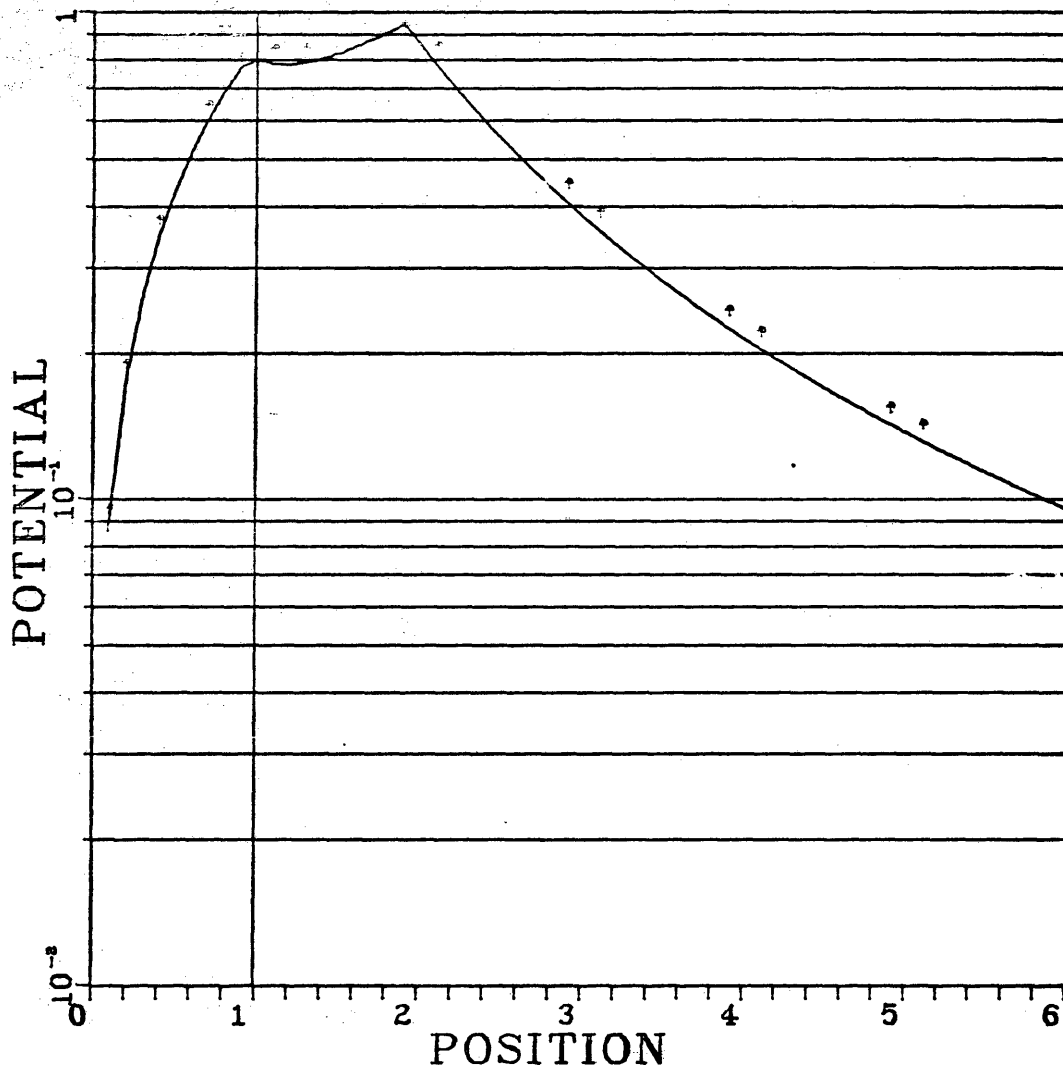


Fig. 13: The symbols represent the numerical results of the modeling for two half spheres with different reflection coefficients. The solid line represents the analytic solution. $D1$ and $D2$ are the radii of the inner sphere and the outer sphere respectively. $R1$, $R2$ and $R3$ are the resistivities of the homogeneous earth, the outer sphere and the inner sphere respectively.

SOLID LINE: ANALYTIC

D1=.95, D2=1.9, R1=3., R2=1., R3=3.

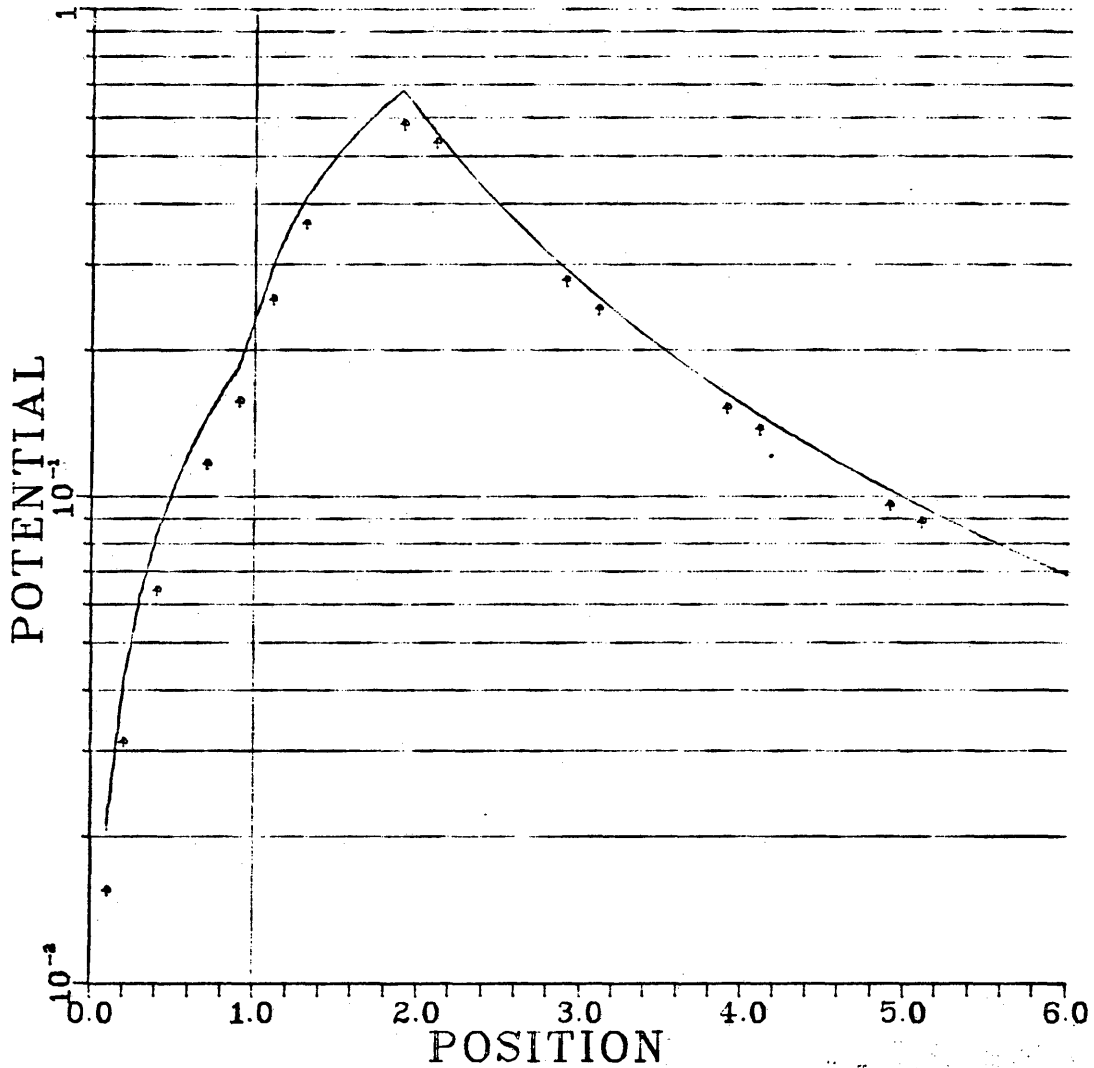


Fig. 14: The symbols represent the numerical results of the modeling for two half spheres with different reflection coefficients. The solid line represents the analytic solution. $D1$ and $D2$ are the radii of the inner sphere and the outer sphere respectively. $R1$, $R2$ and $R3$ are the resistivities of the homogeneous earth, the outer sphere and the inner sphere respectively.

sphere, so are the numerical results. In order to eliminate this kind of error, it is better to make the facets tangential to the sphere. In the numerical computation for the testing model, the vertices of the triangular facets are located on two half spheres of radii one and two and the analytical solutions are calculated for those of radii 0.95 and 1.9. In this condition, the triangular facets are approximately tangential to two half spheres.

The results for the normalized second vertical derivative (see Appendix 4) using a bipole source over a model shown in Fig.15 are shown from Fig.16 to Fig.23 for different reflection coefficients. This model is simulated by 128 triangular facets. The sources are arranged such that the positive current electrode is closer to the buried bodies than the negative one is. The results show that there is a high value of the normalized second vertical derivative over the buried conducting body, while there is a low value of that over the insulating body. The position of the maximum value for the conducting case shifts toward sources, while the position of the minimum value for the insulating case shifts away from sources. For $K=+0.3$, the maximum response is about 30 percent of the primary field. For $K=+1.0$, the maximum response is about 120 percent of the

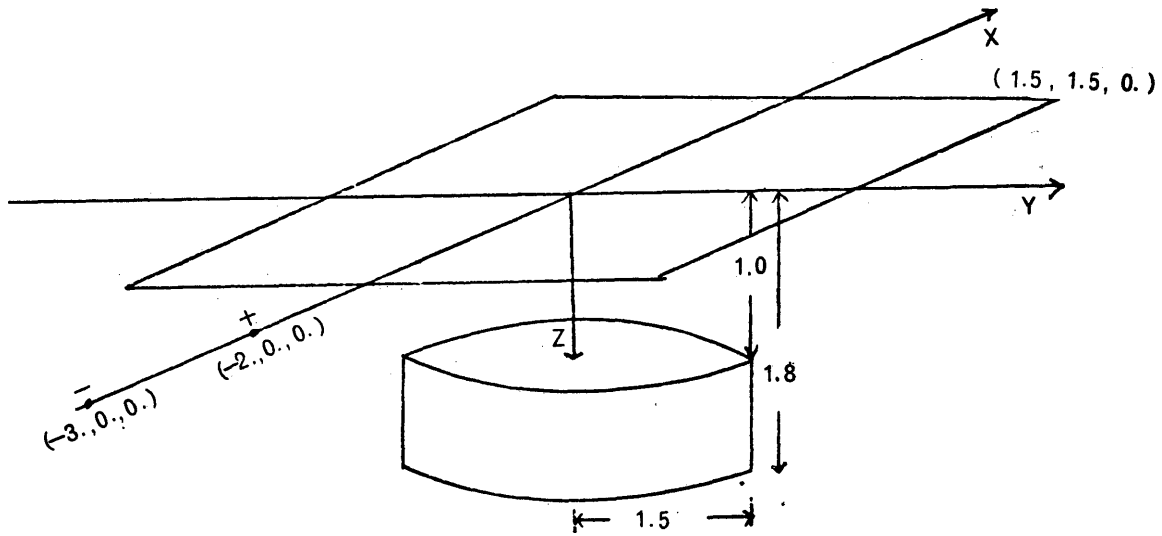


Fig. 15: The above shows the model and the source locations from which the responses of the Bipole-Pole array have been calculated. The receivers are on the grid points of the square area shown above.

S. V. D. T., NORM., K=0.3.

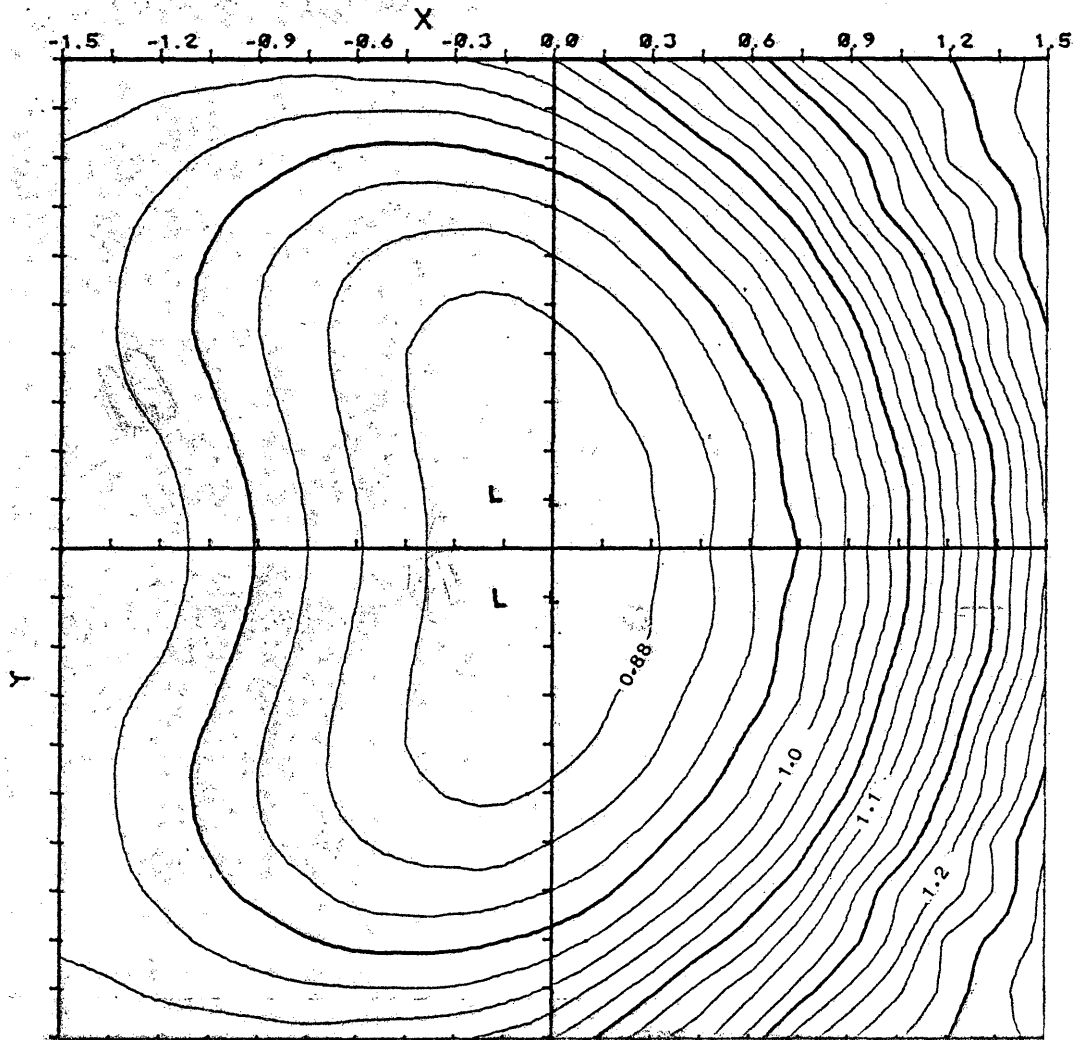


Fig. 16

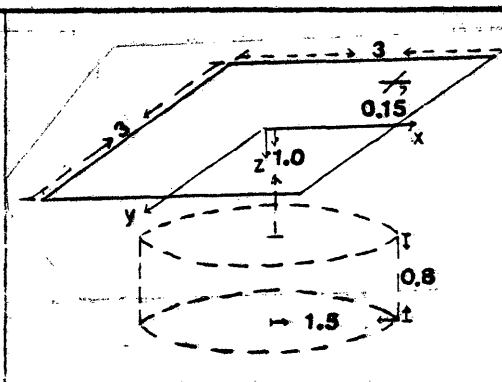
Reflection coefficient:

$K = 0.3$

Coord. of the sources :

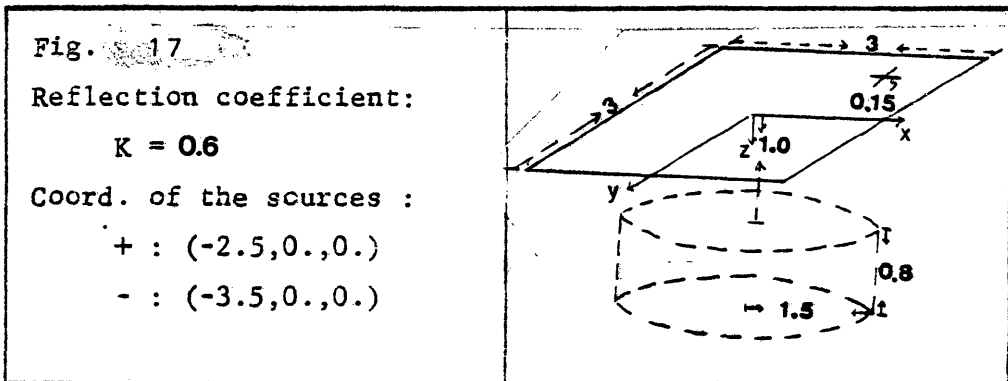
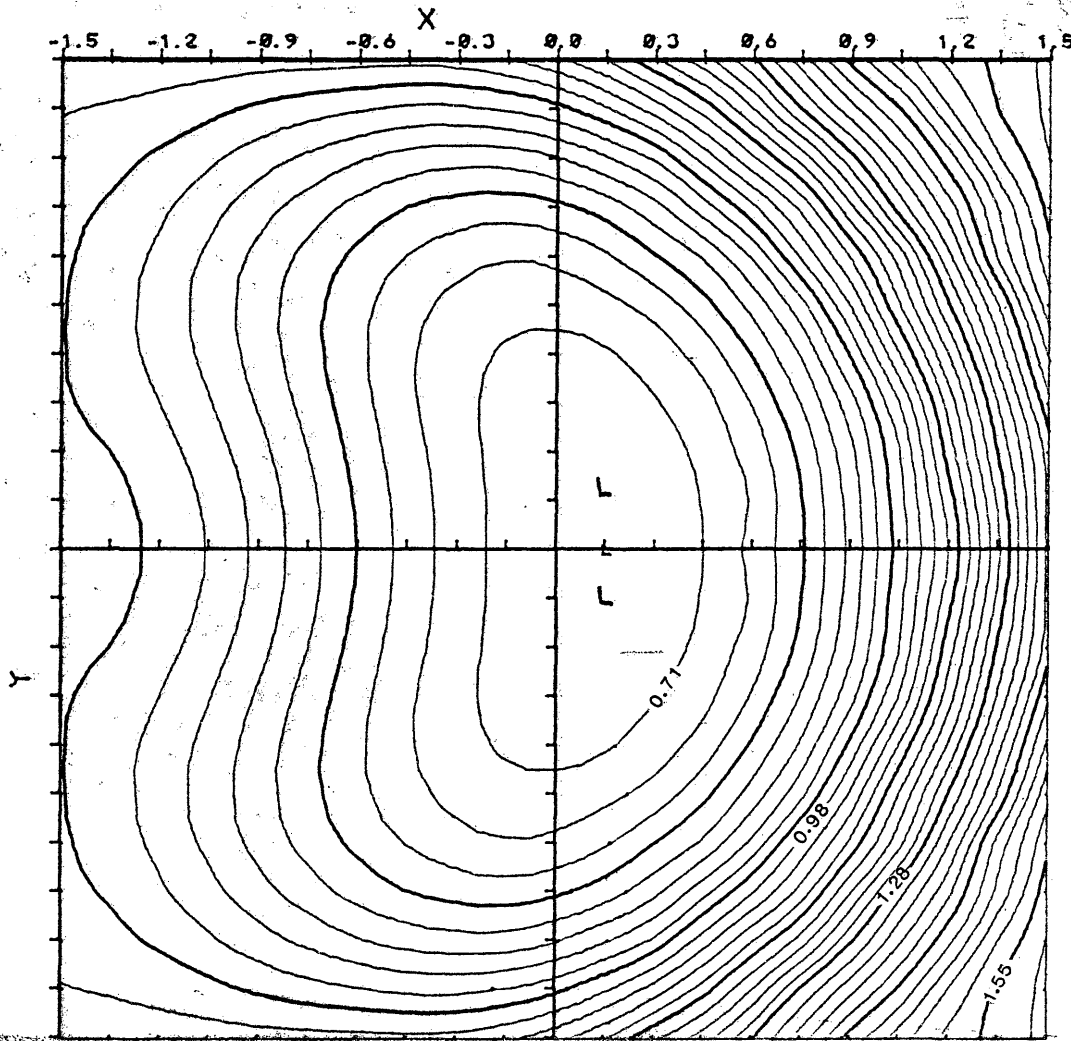
+ : (-2.5, 0., 0.)

- : (-3.5, 0., 0.)



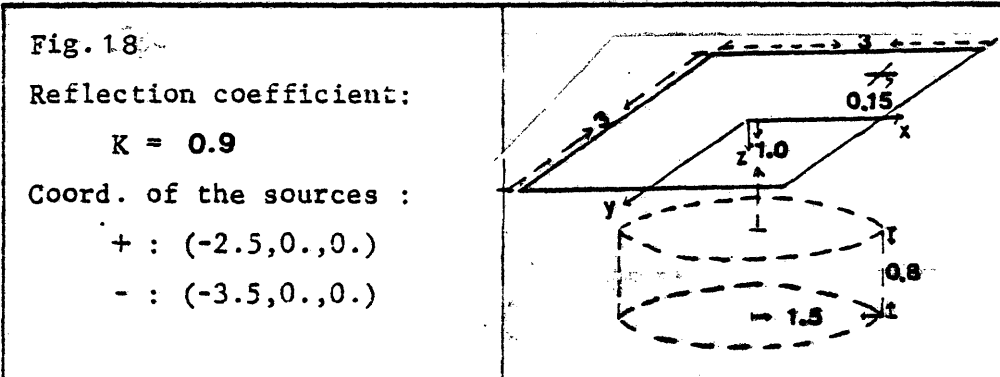
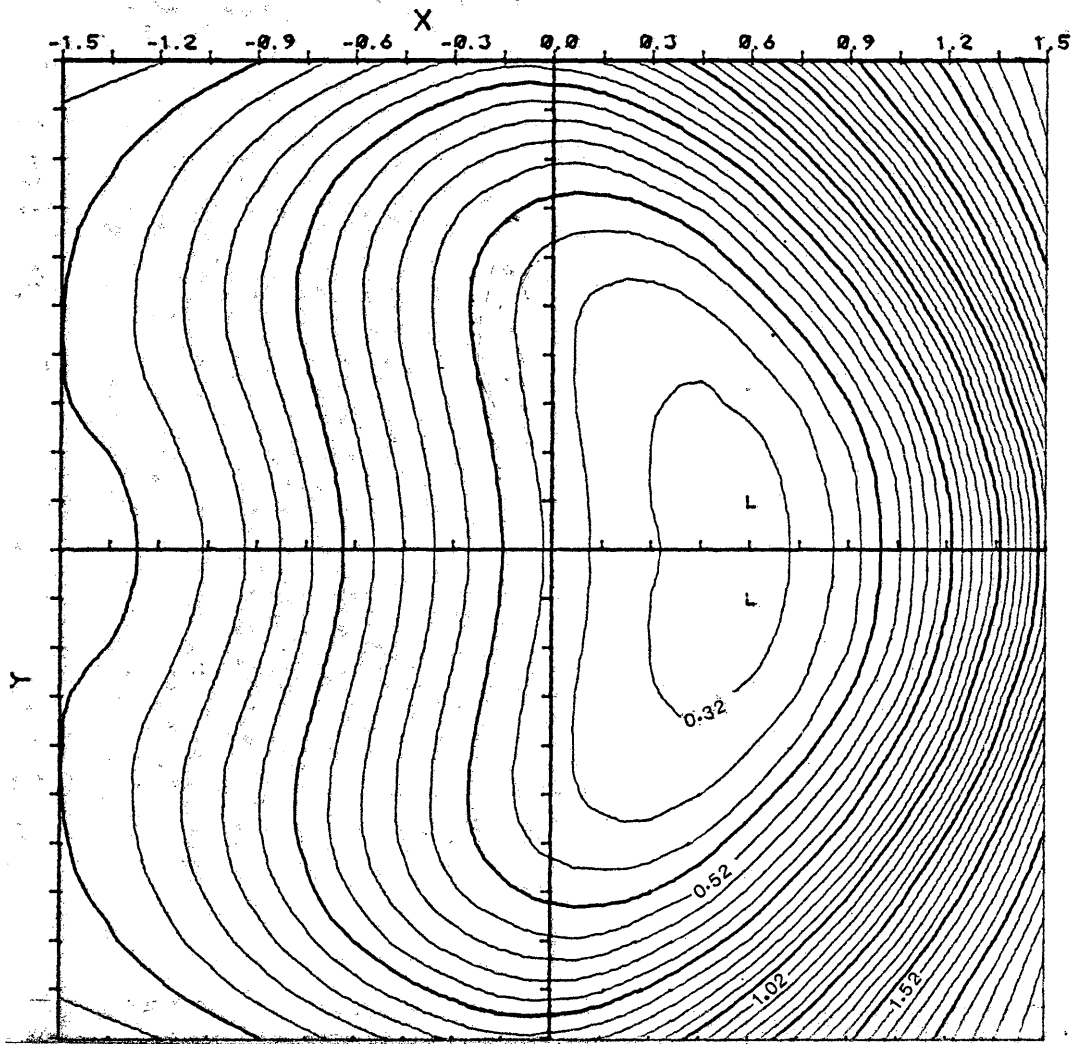
Contour map of the normalized second vertical derivative for the model shown above.

S.V.D.T., NORM., $K=0.6$



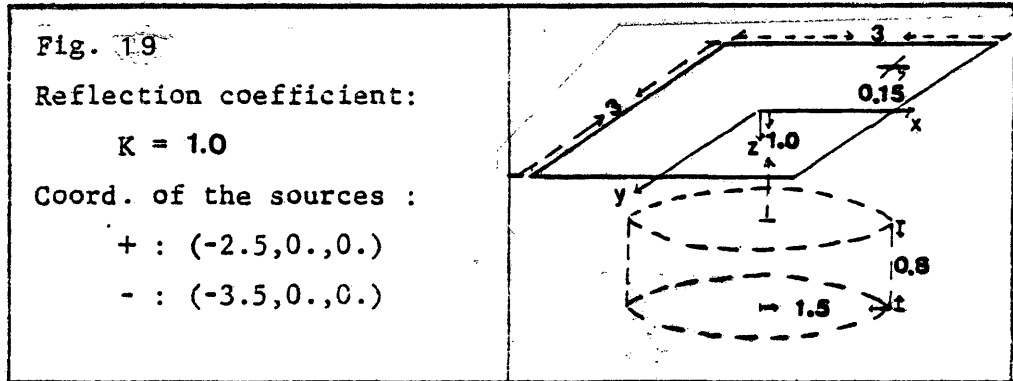
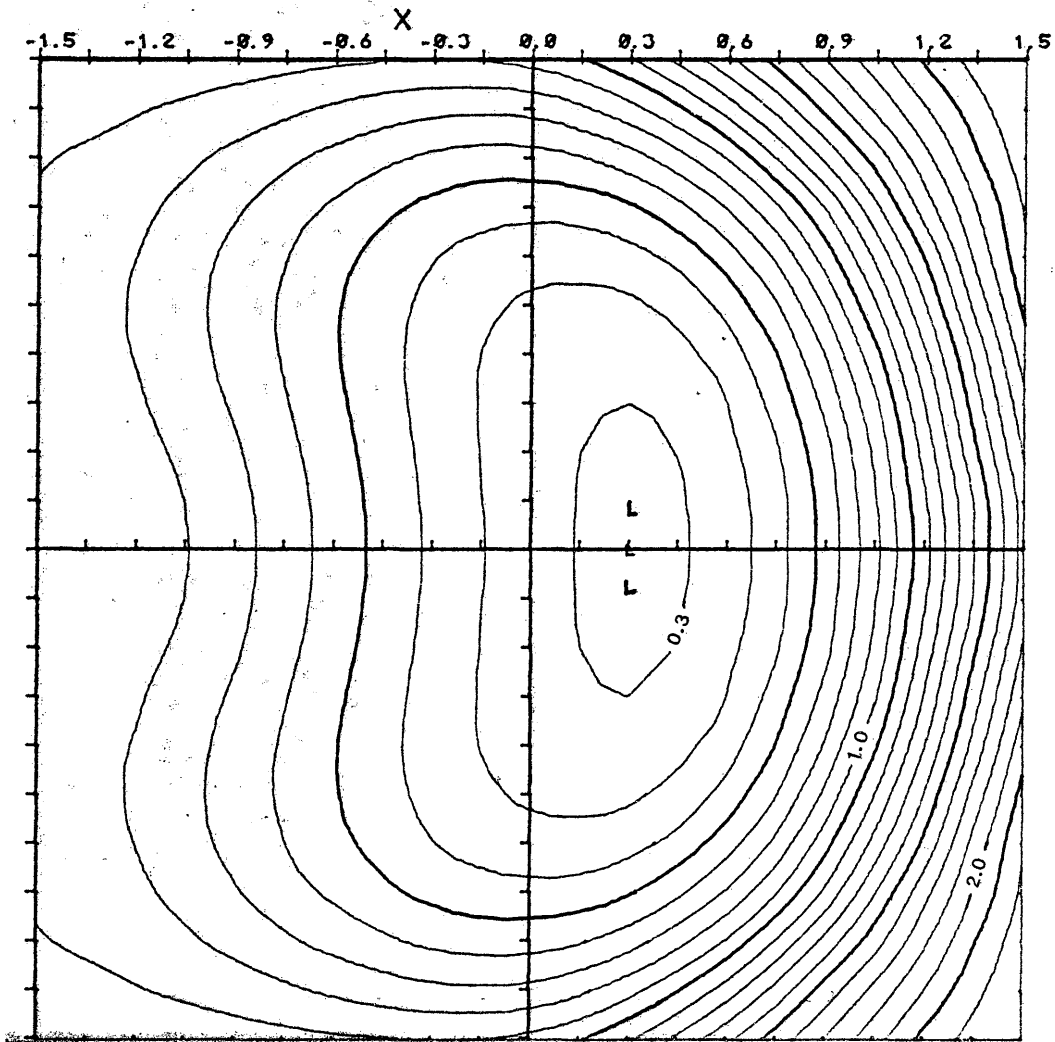
Contour map of the normalized second vertical derivative for the model shown above.

S.V.D.T., NORM., $K=0.9$



Contour map of the normalized second vertical derivative for the model shown above.

S.V.D.T., NORM., K=1.0



Contour map of the normalized second vertical derivative for the model shown above.

S.V.D.T. NORM. $K = -0.3$

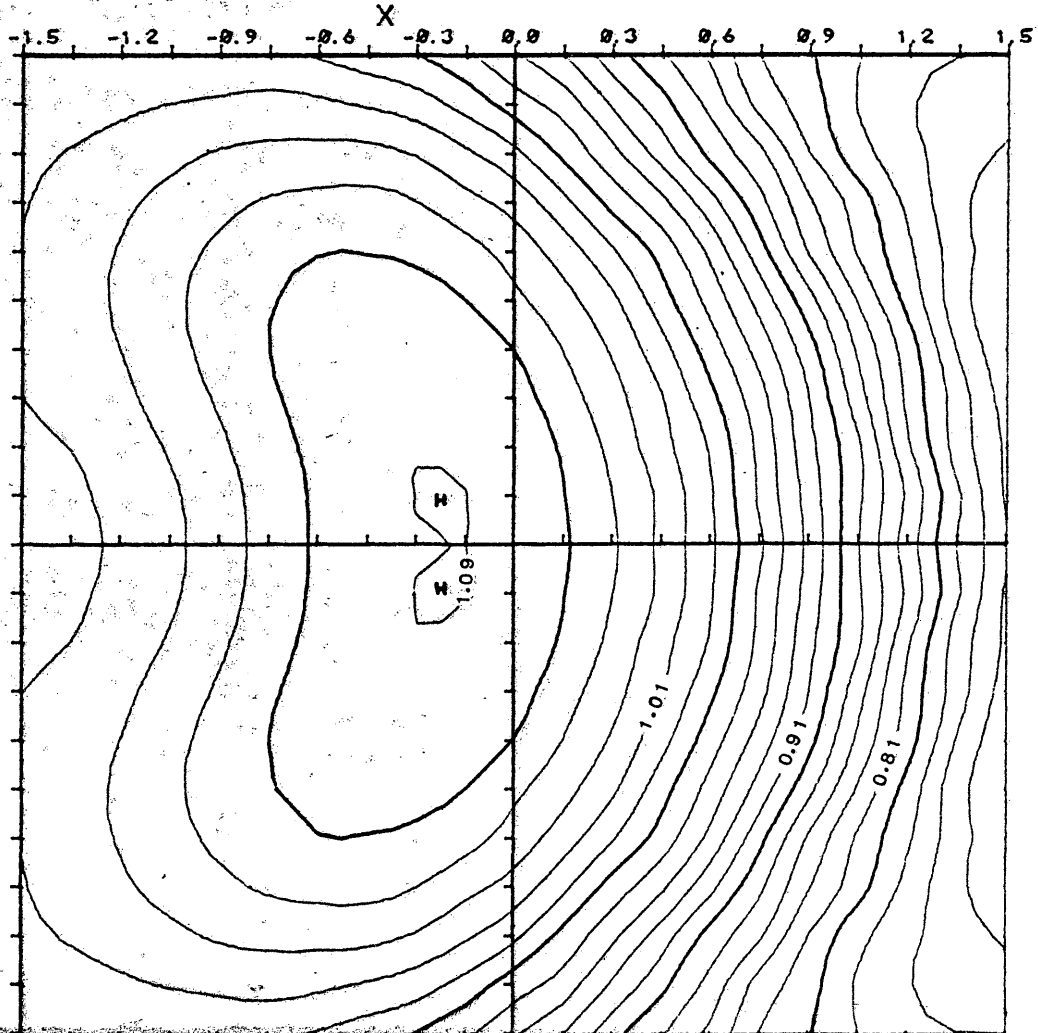


Fig. 20

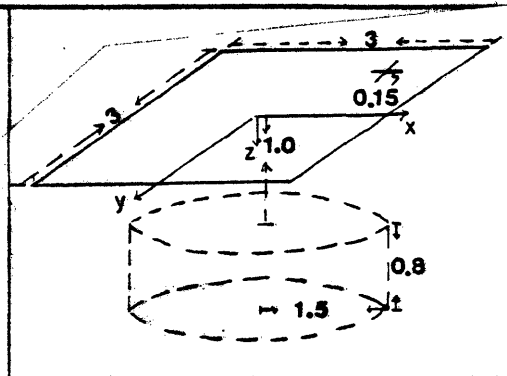
Reflection coefficient:

$$K = -0.3$$

Coord. of the sources :

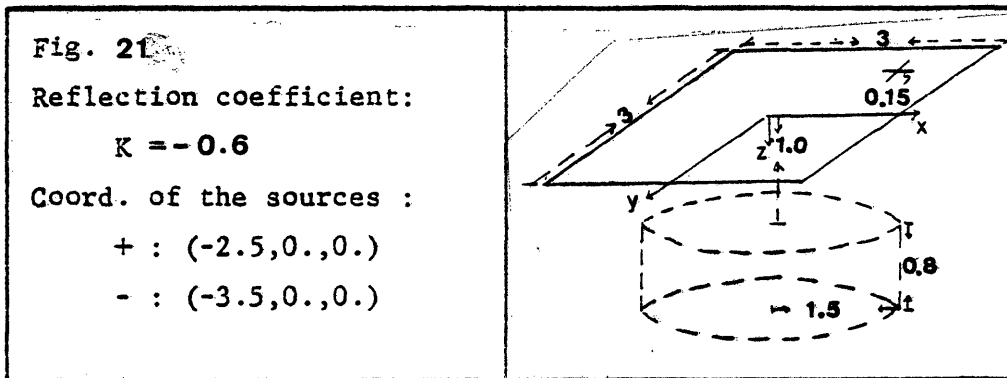
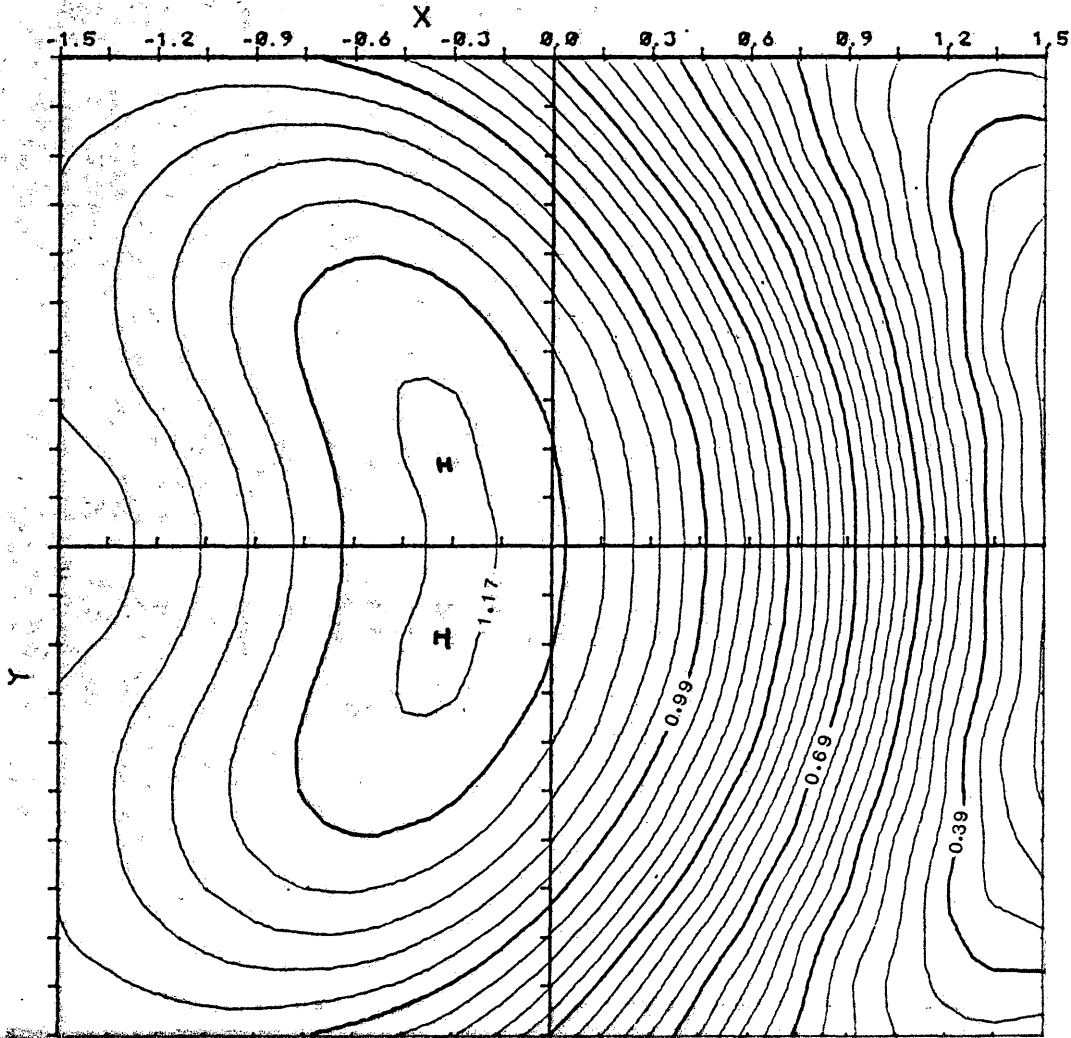
$$+ : (-2.5, 0., 0.)$$

$$- : (-3.5, 0., 0.)$$



Contour map of the normalized second vertical derivative for the model shown above.

S.V.D.T., NORM., $K = -0.6$



Contour map of the normalized second vertical derivative for the model shown above.

S.V.D.T., NORM., $K = -0.9$

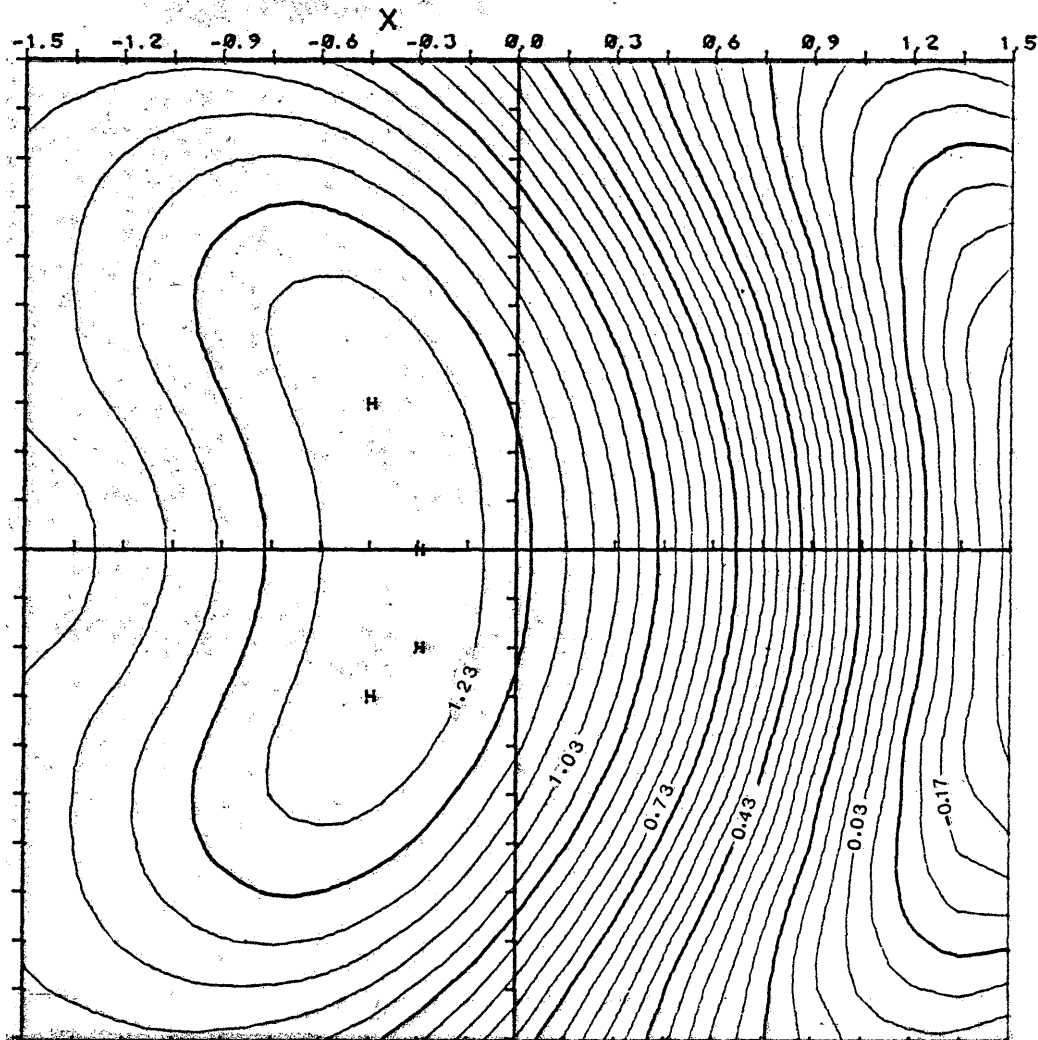


Fig. 22

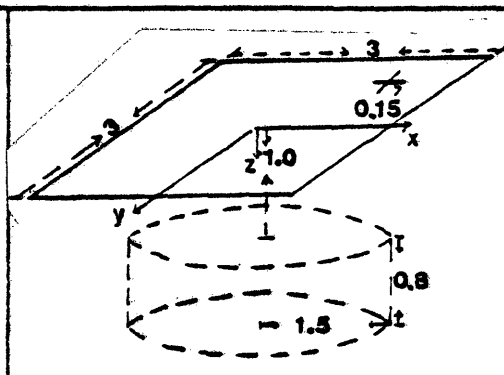
Reflection coefficient:

$$K = -0.9$$

Coord. of the sources :

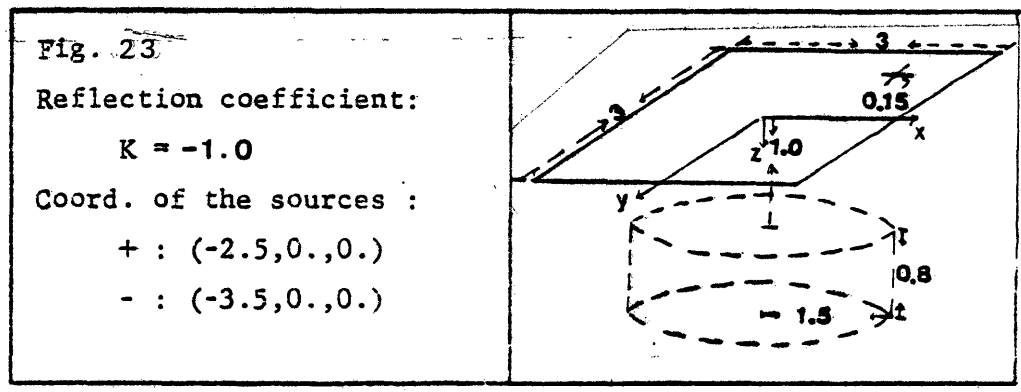
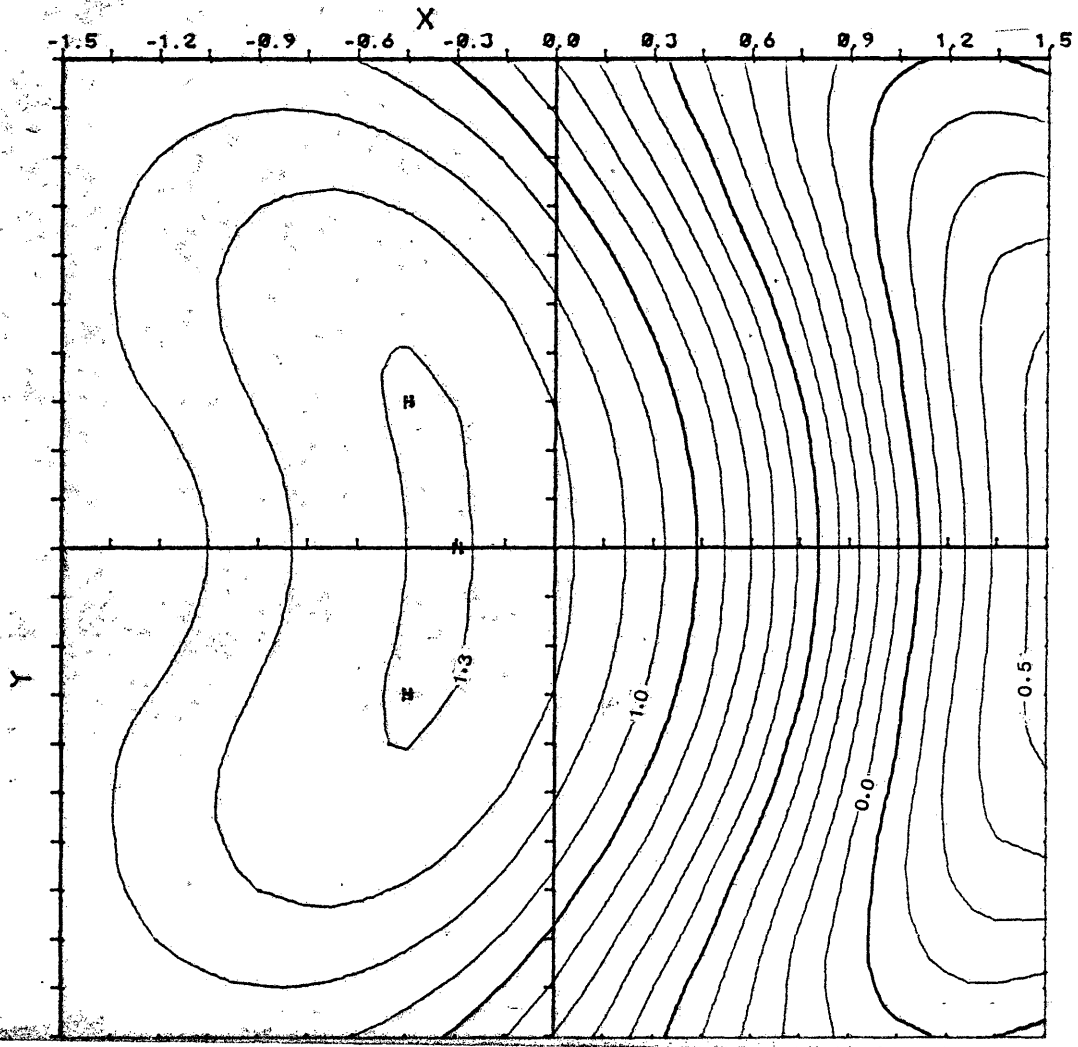
$$+ : (-2.5, 0., 0.)$$

$$- : (-3.5, 0., 0.)$$



Contour map of the normalized second vertical derivative for the model shown above.

S.V.D.T., NORM., K=-1.0



Contour map of the normalized second vertical derivative for the model shown above.

primary field. Measuring the second vertical derivative thus possesses a high resolving capability.

Imperfect Thin Insulators

In order to test the accuracy of the program which is to model the response of arbitrarily shaped three-dimensional thin insulators, we use an imperfect thin half sphere, as shown in Fig.24, as our testing model and compute the potentials along the x axis. The analytical expression for the potential subjected to an uniform primary field is shown in Appendix 1.

In the numerical computation for the testing model, the half sphere is simulated by 32 trapezoid facets which are tangential to the sphere of radius one. Each trapezoid is then approximated by a rectangular. The comparisons of the numerical results with the analytical ones are shown from Fig.25 to Fig.29. The numerical results are accurate even for large T values.

The modelings over a horizontally circular thin insulator for the second vertical derivative have been tested for different geometrical and electrical parameters. In the numerical computations, the circular disks are

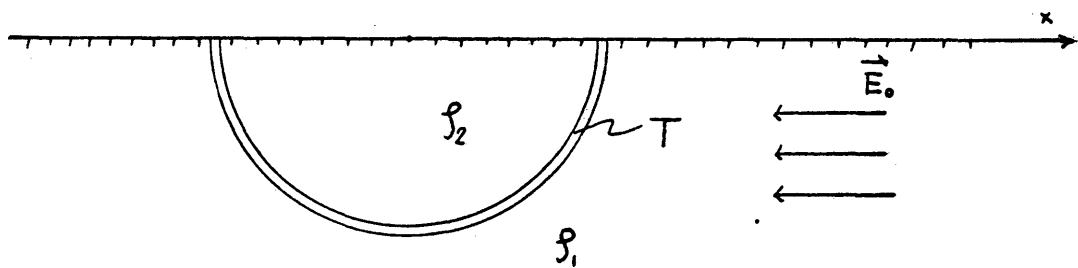


Fig. 24: an imperfect thin half sphere buried just beneath the surface and subjected to an uniform primary electrical field.

SOLID LINE: ANALYTIC SOL.
 $T=0.3$

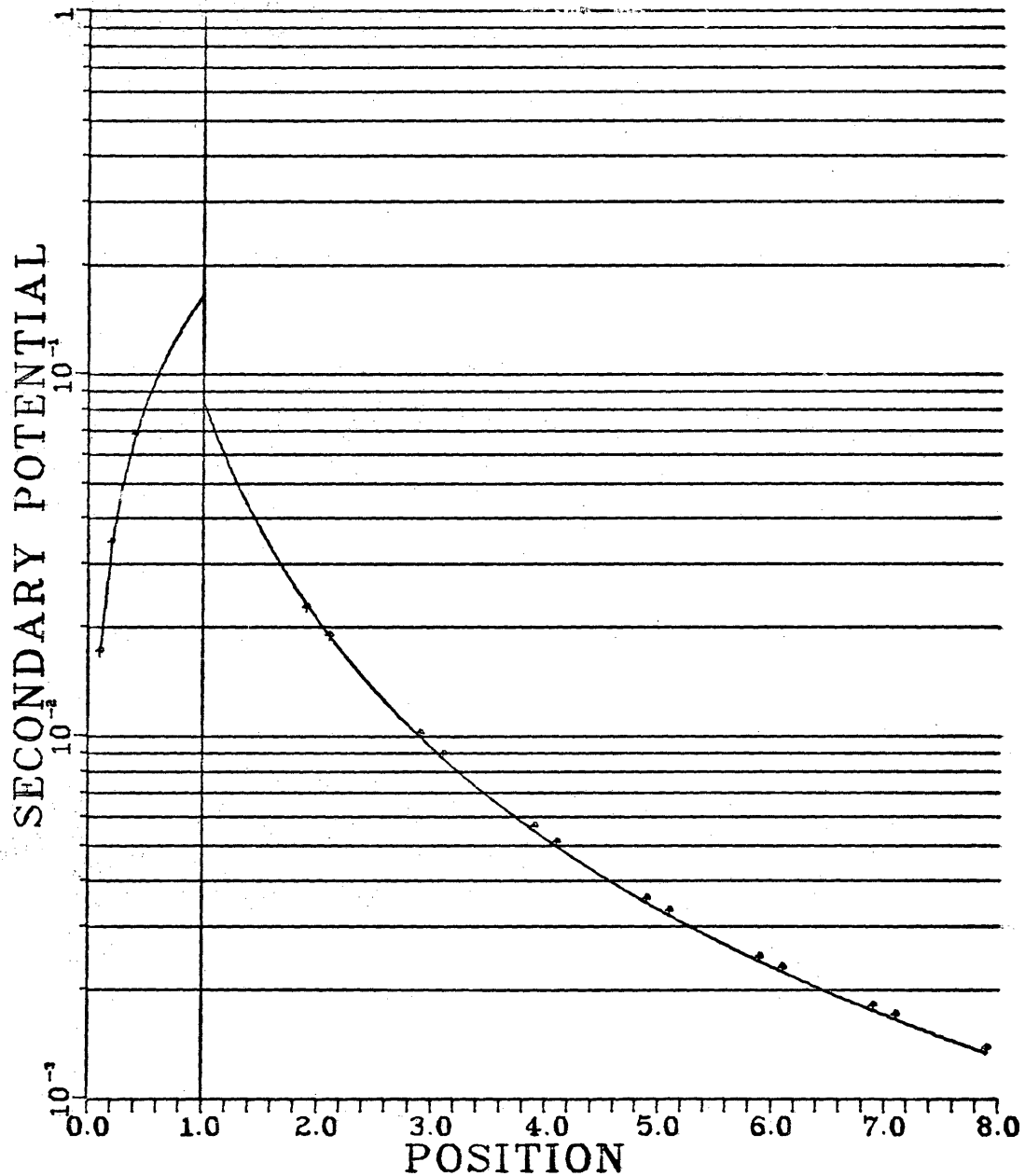


Fig. 25 : The symbols represent the numerical results of the modeling for an imperfect thin half sphere. The solid line represents the analytic solution. The radius of the half sphere is one. The values of the secondary potential inside the half sphere are negative. The above shown their absolute values. T represents the insulating factor.

SOLID LINE: ANALYTIC SOL.
 T=1.0

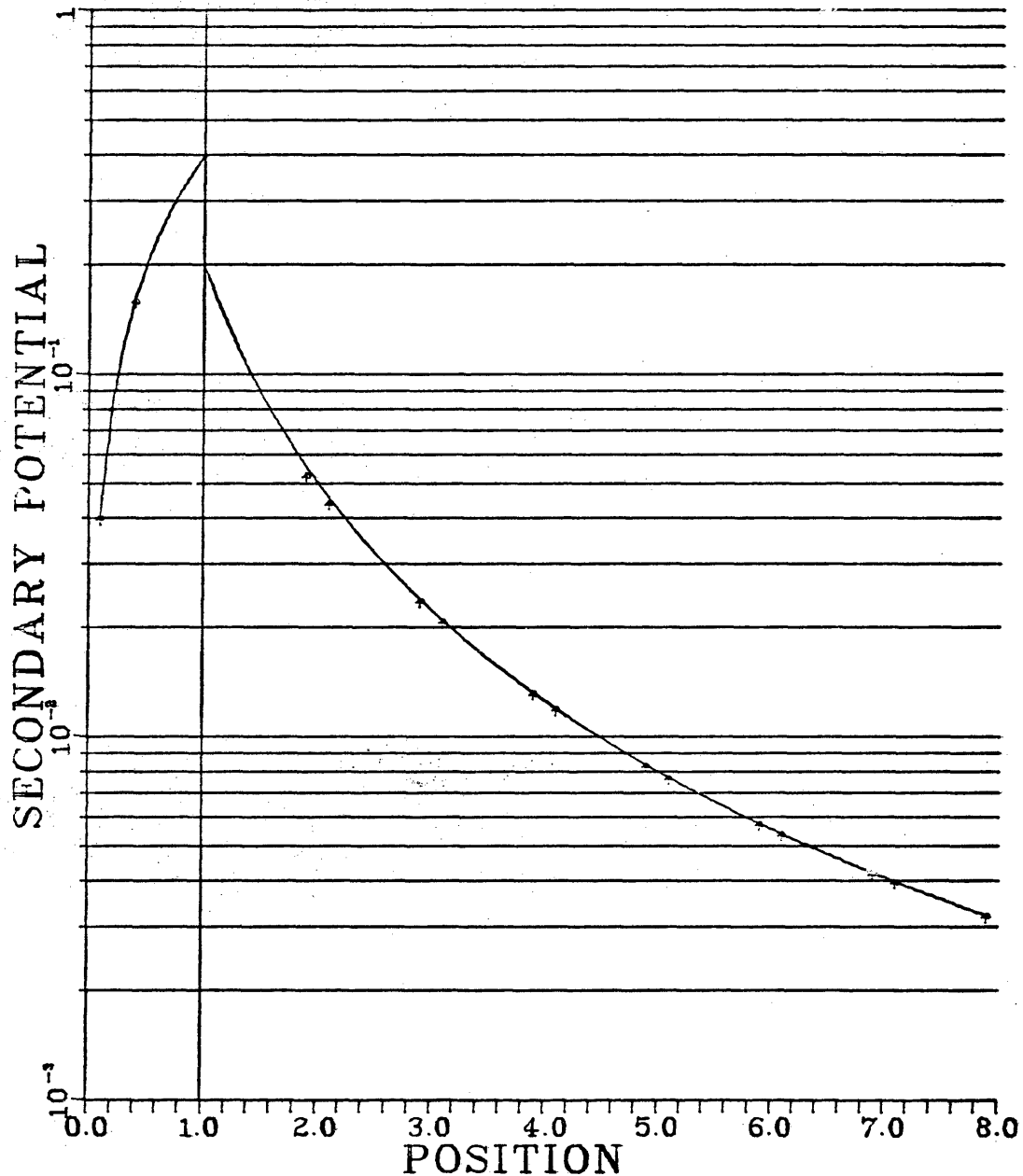


Fig. 26: The symbols represent the numerical results of the modeling for an imperfect thin half sphere. The solid line represents the analytic solution. The radius of the half sphere is one. The values of the secondary potential inside the half sphere are negative. The above shown their absolute values. T represents the insulating factor.

SOLID LINE: ANALYTIC SOL.
 $T=3.0$

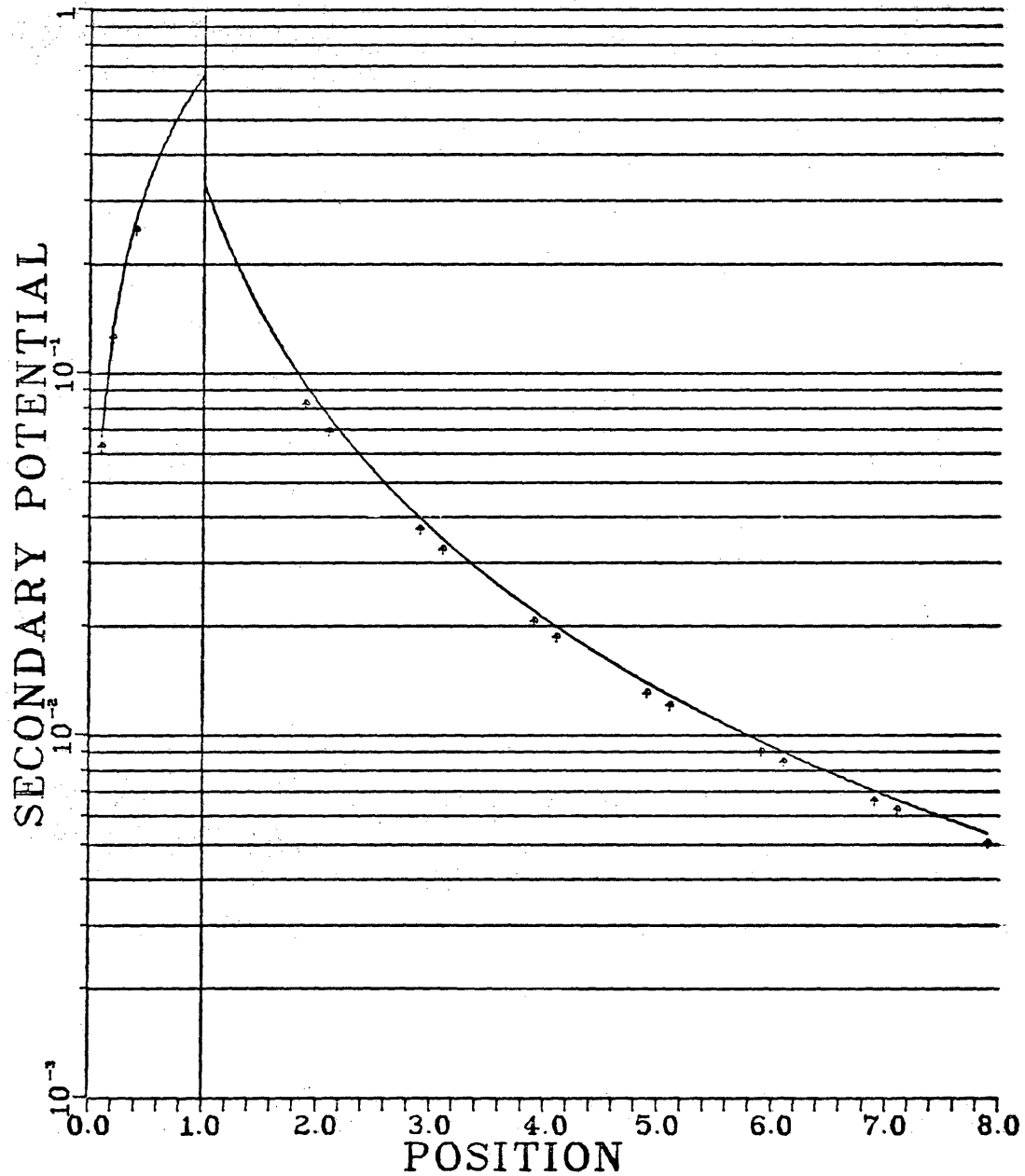


Fig. 27 : The symbols represent the numerical results of the modeling for an imperfect thin half sphere. The solid line represents the analytic solution. The radius of the half sphere is one. The values of the secondary potential inside the half sphere are negative. The above shown their absolute values. T represents the insulating factor.

SOLID LINE: ANALYTIC SOL.
 T=6.0

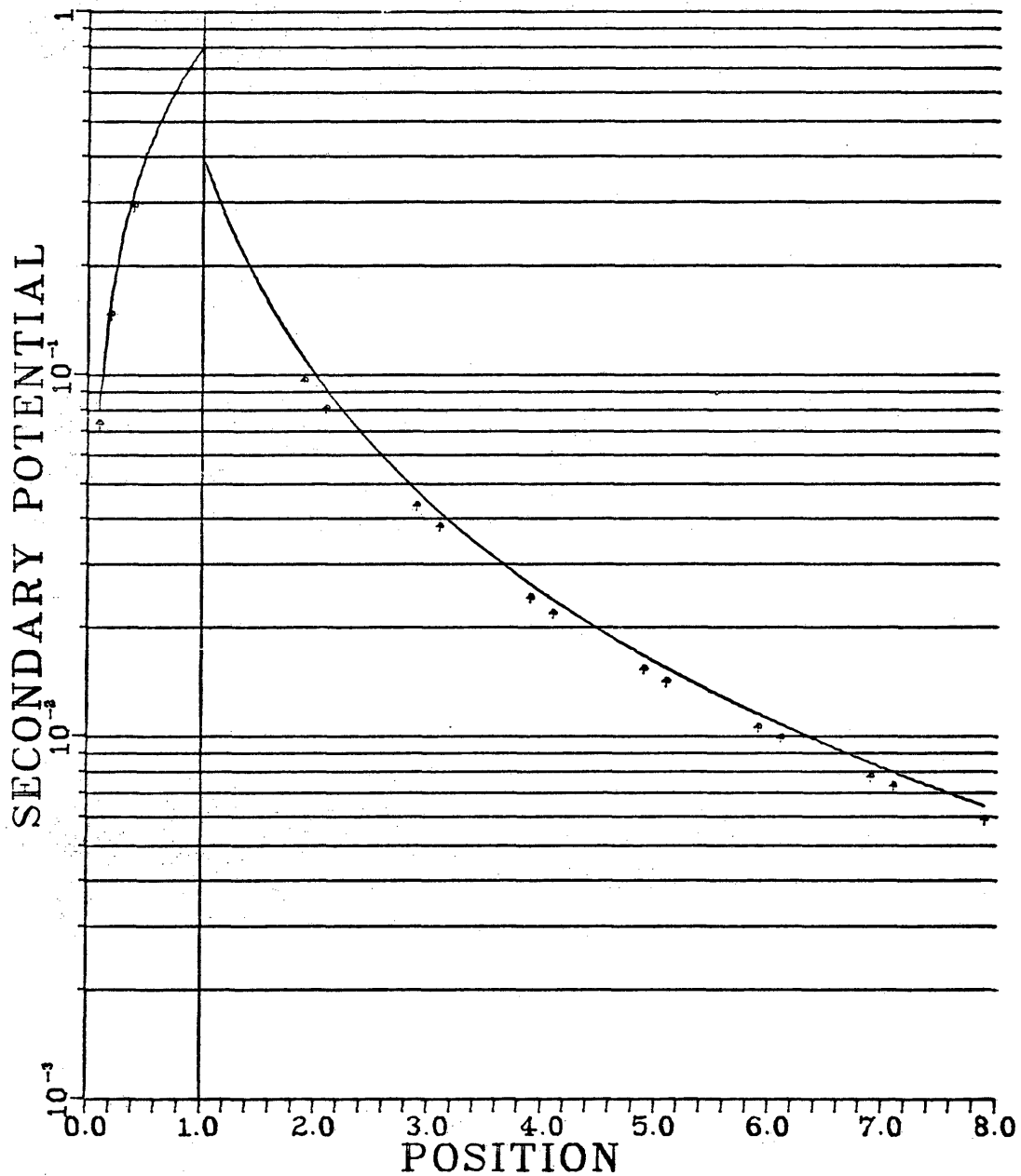


Fig. 28: The symbols represent the numerical results of the modeling for an imperfect thin half sphere. The solid line represents the analytic solution. The radius of the half sphere is one. The values of the secondary potential inside the half sphere are negative. The above shown their absolute values. T represents the insulating factor.

SOLID LINE: ANALYTIC SOL.
 T=50.0

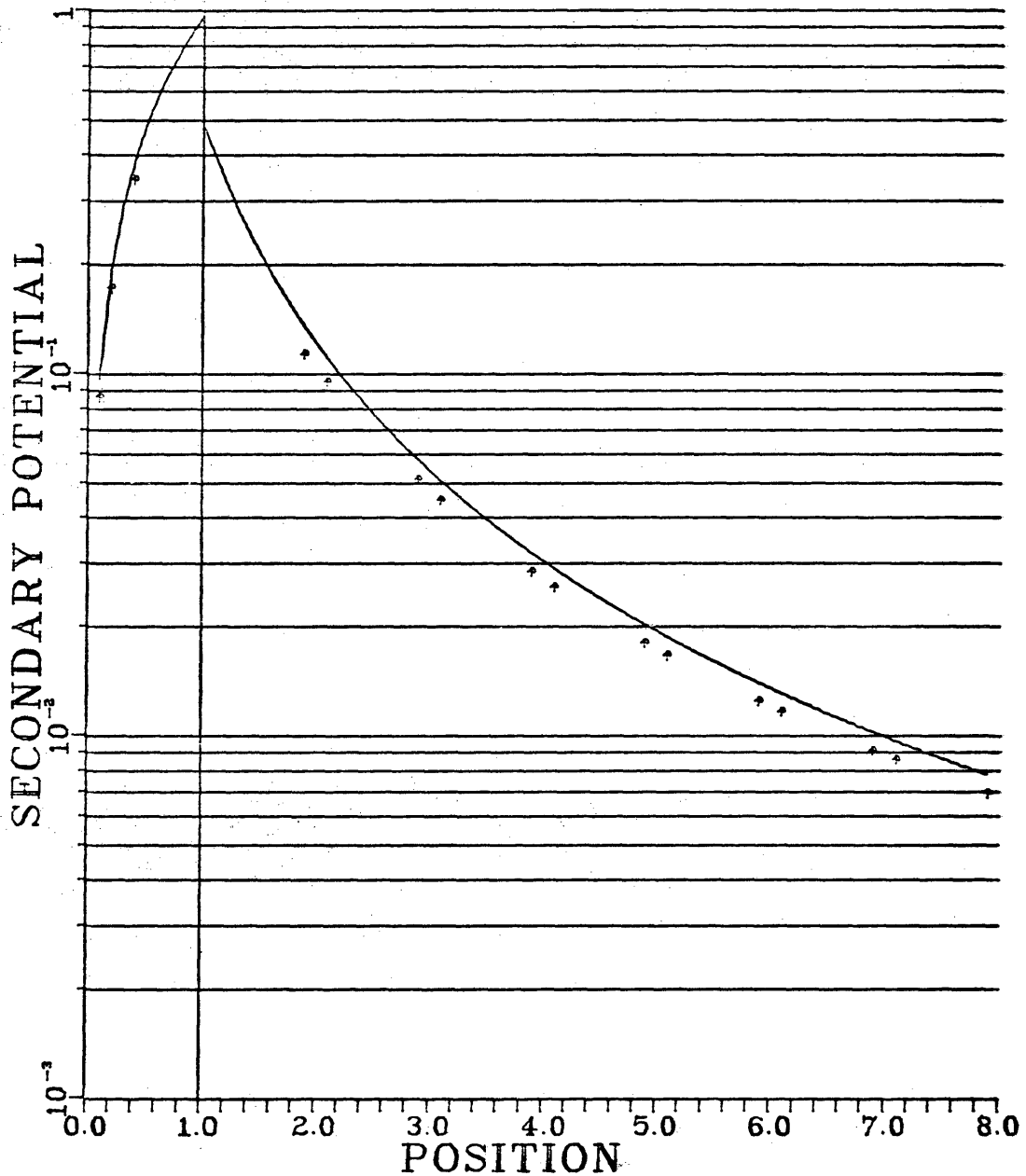


Fig. 29: The symbols represent the numerical results of the modeling for an imperfect thin half sphere. The solid line represents the analytic solution. The radius of the half sphere is one. The values of the secondary potential inside the half sphere are negative. The above shown their absolute values. T represents the insulating factor.

simulated by 52 rectangular facets, as shown in Fig. 30. When buried current electrode is used, the disk is simulated by 68 rectangular facets, as shown in Fig.30.

Table 1 shows the maximum second vertical derivatives of the total potentials for different T values, which have been normalized with respect to that of the primary field. The depth to the disk is unity and the diameter of the disk is two. The source and the receiver configurations are shown in Fig.31. From table 1, the maximum responses for those with T value greater than 3 is about 20 percent of the primary field. The contour maps of the second vertical derivatives for different T values are shown from Fig.32 to Fig.37. The results show that the positions of the minimum values of the second vertical derivatives shift toward the sources and that the contours are in peanut-like shape around the minimum values. At right parts of the contour maps, there are relatively high values. Note also that the contours with unity value are approximately at the same position for different T values.

Let the diameter of the circular disk be unity instead of two. The maximum responses of the normalized second vertical derivatives of the total potentials are shown in

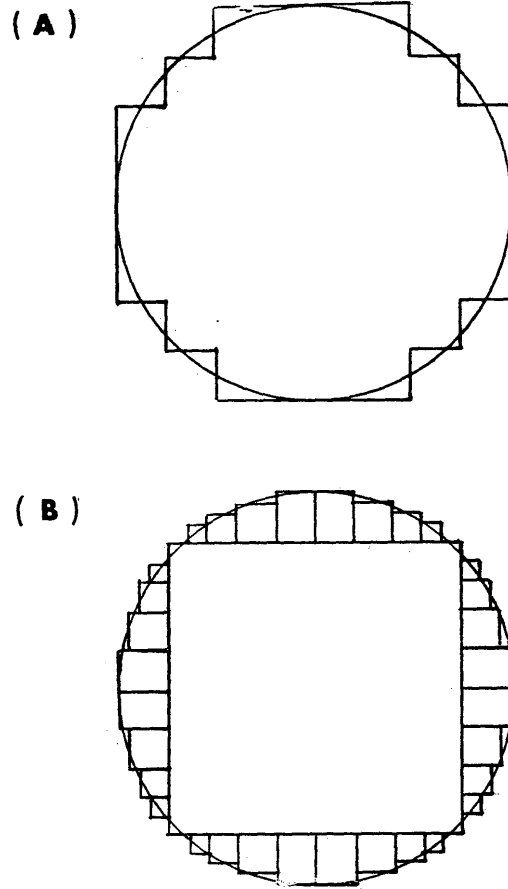


Fig. 30: The thin circular disk is simulated by 52 rectangular facets as shown in (A). When buried current electrode is used, it is simulated by 68 rectangular facets as shown in (B).

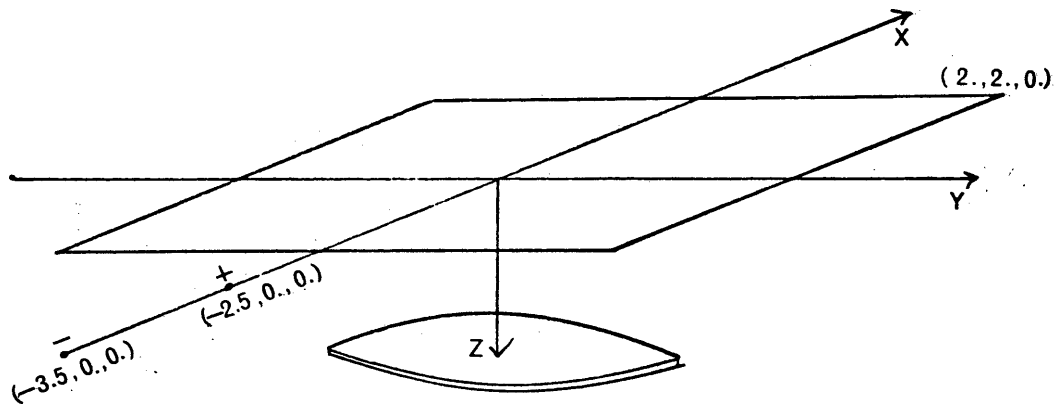
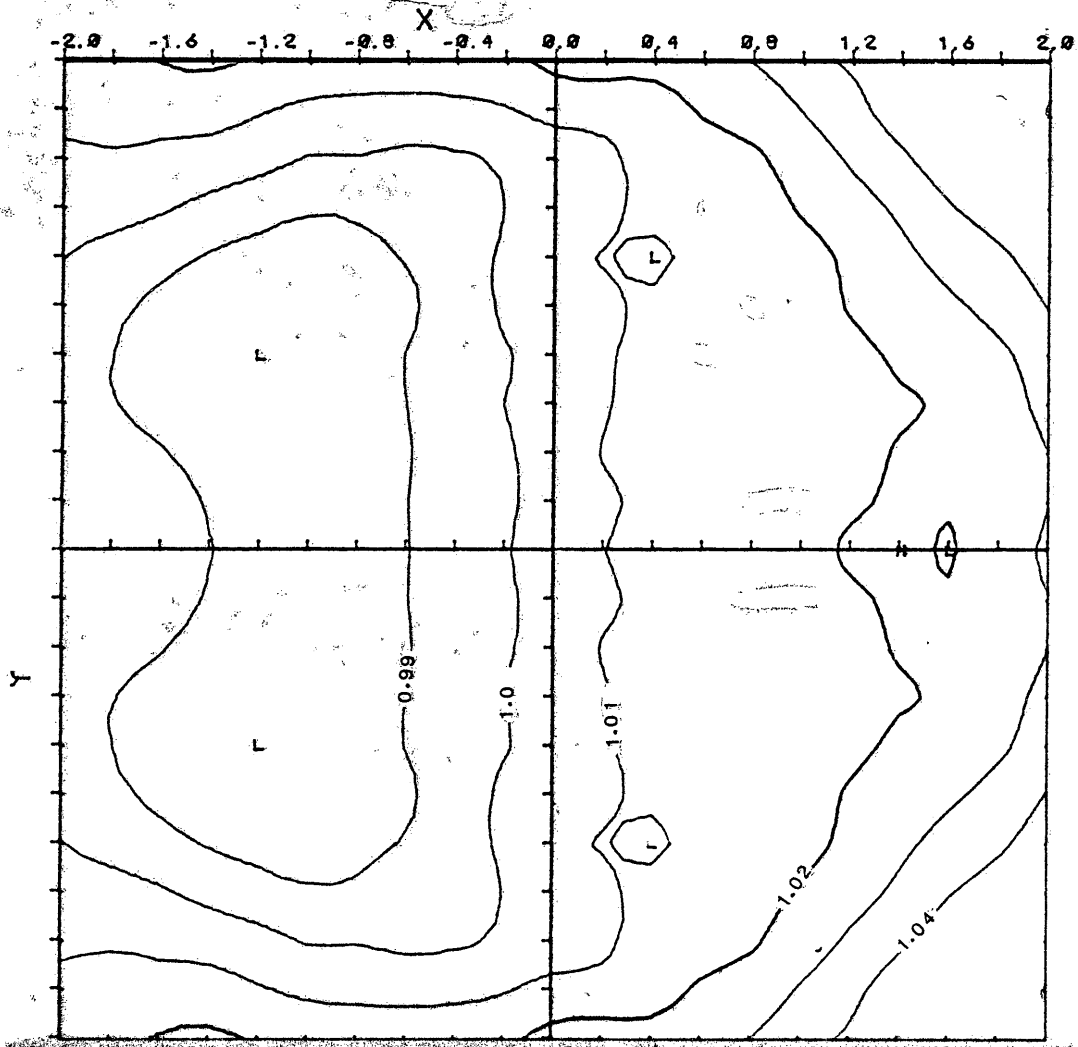


Fig. 31: The above shows the thin disk and the source locations, from which the responses of the Bipole-Pole array have been calculated. The receivers are on the grid points of the square area shown above.

S.V.D.T., NORM., T=0.1



<p>Fig: 32</p> <p>Diameter of the disk : 2</p> <p>Depth to the disk : 1</p> <p>Trans. res. of the disk: 0.1</p> <p>Coord. of the source(s):</p> <p>+ : (-2.5, 0., 0.)</p> <p>- : (-3.5, 0., 0.)</p>	<p>The diagram shows a 3D coordinate system with x, y, and z axes. A horizontal rectangle represents a disk with a diameter of 4.0 units. The depth to the disk is 1.0 unit. Two source locations are indicated: a '+' sign at (-2.5, 0., 0.) and a '-' sign at (-3.5, 0., 0.).</p>
--	---

Contour map of the normalized second vertical derivative for the model shown above.

S.V.D.T, NORM., T=0.3

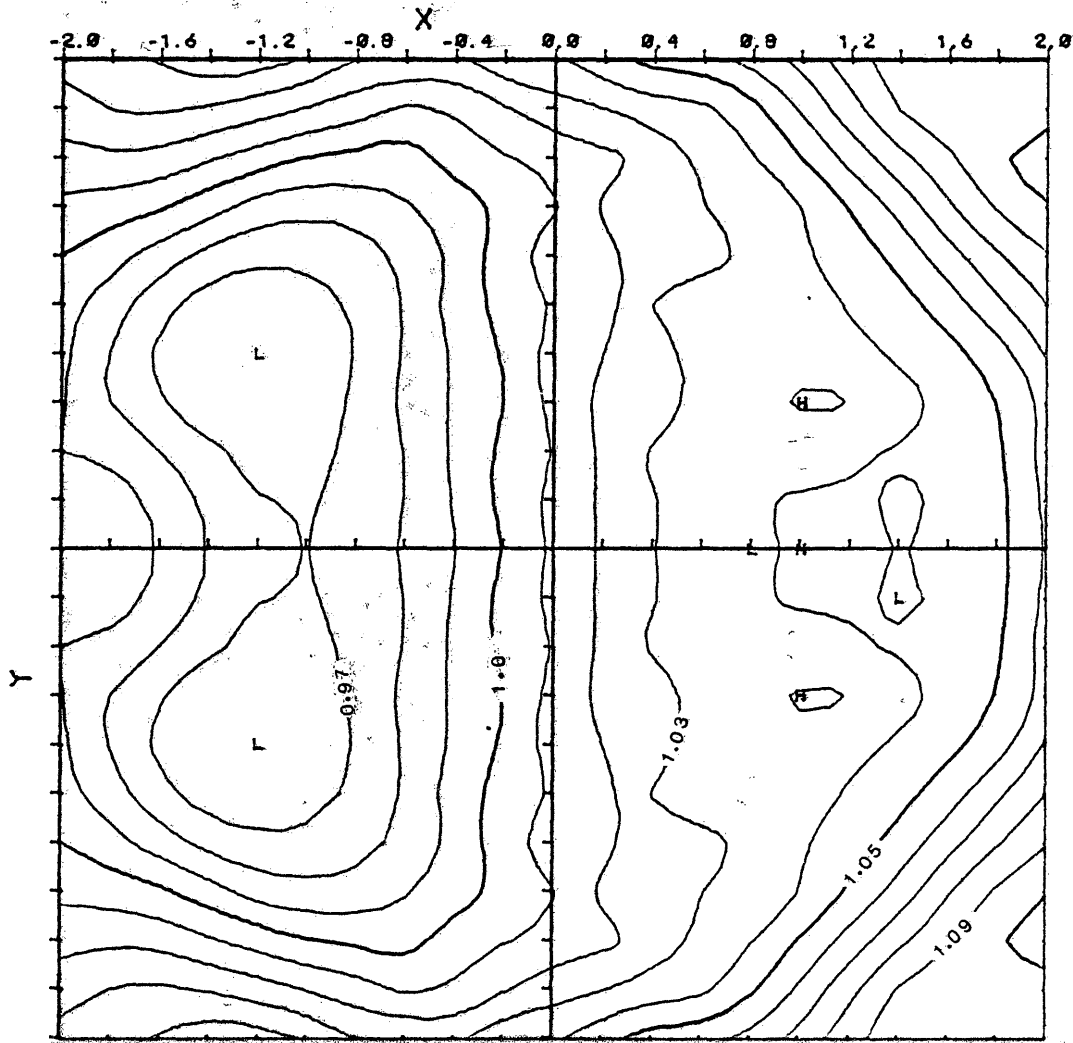
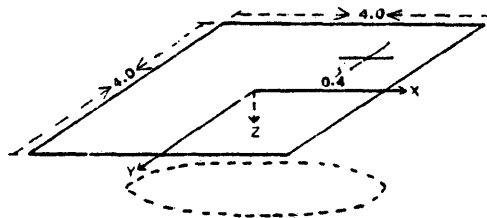


Fig: 33

Diameter of the disk : 2
 Depth to the disk : 1
 Trans. res. of the disk: 0.3
 Coord. of the source(s):
 + : (-2.5,0.,0.)
 - : (-3.5,0.,0.)



Contour map of the normalized second vertical derivative for the model shown above.

S.V.D.T., NORM. T=1.0

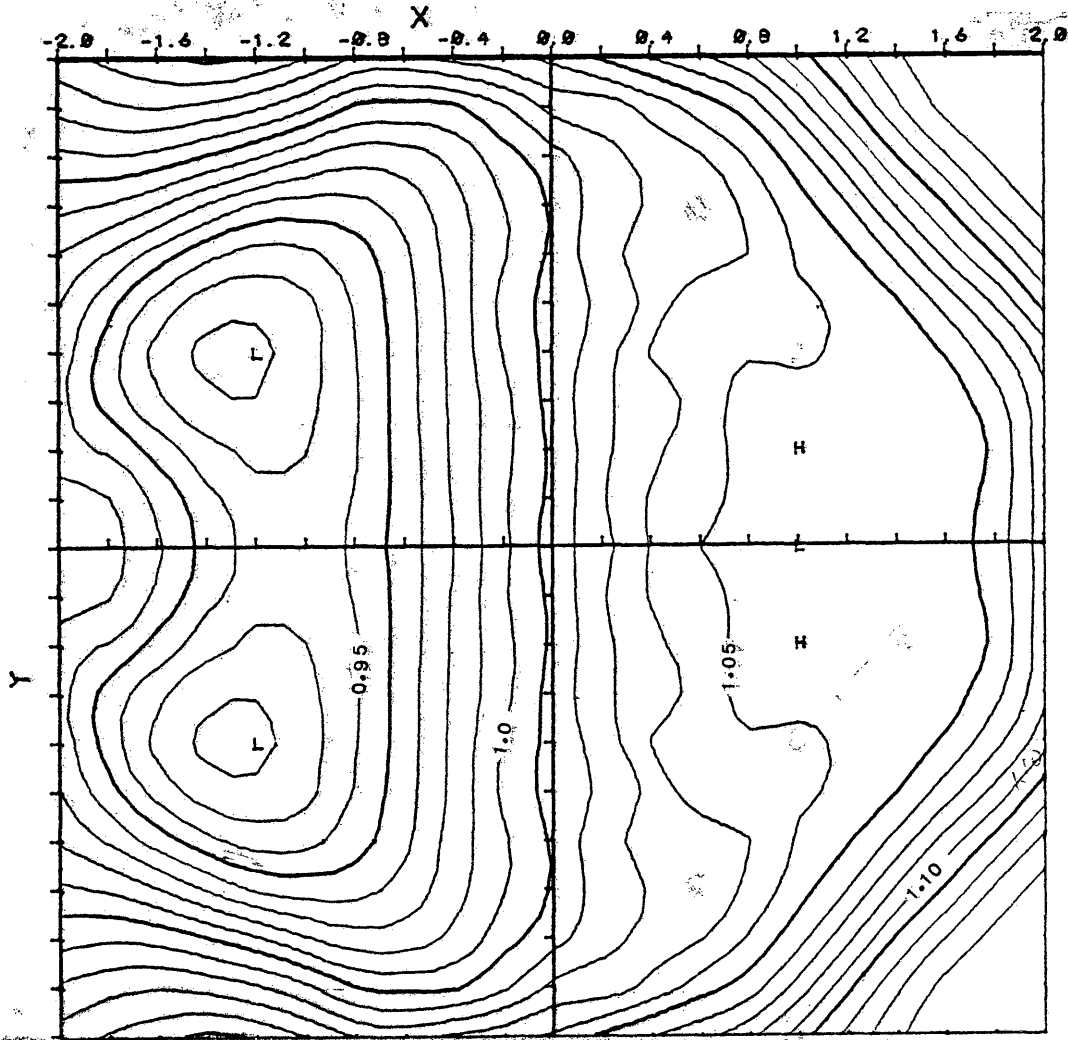
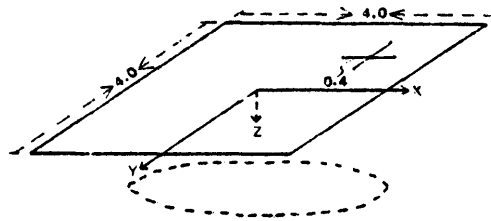


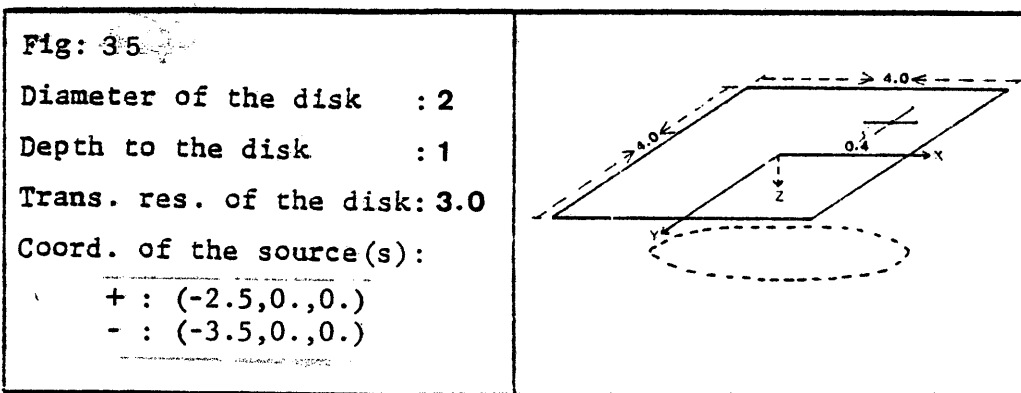
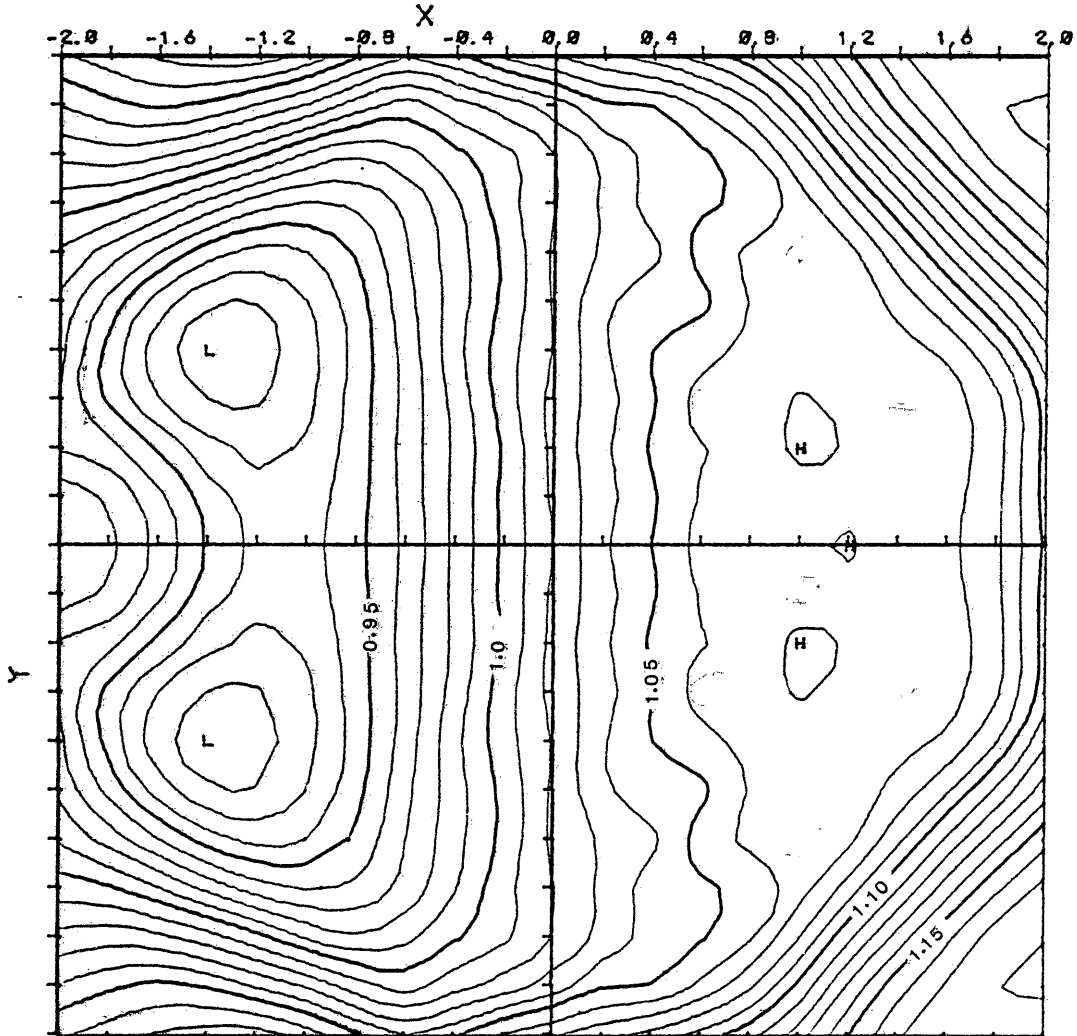
Fig: 34.

Diameter of the disk : 2
 Depth to the disk : 1
 Trans. res. of the disk: 1.0
 Coord. of the source(s):
 + : (-2.5, 0., 0.)
 - : (-3.5, 0., 0.)



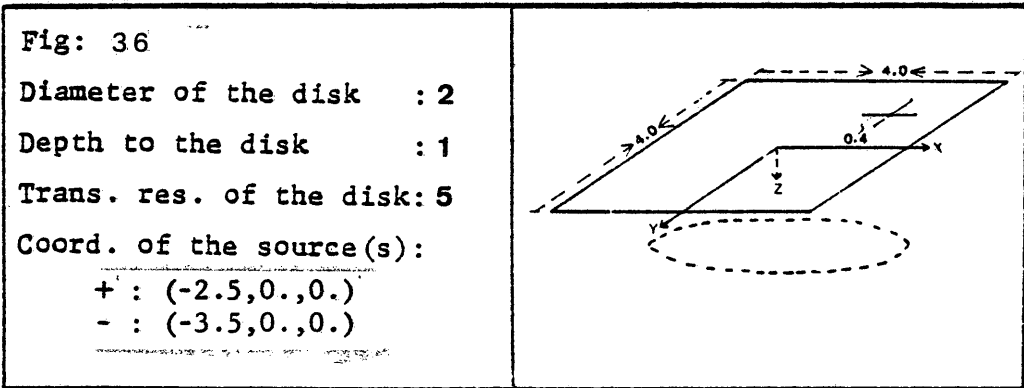
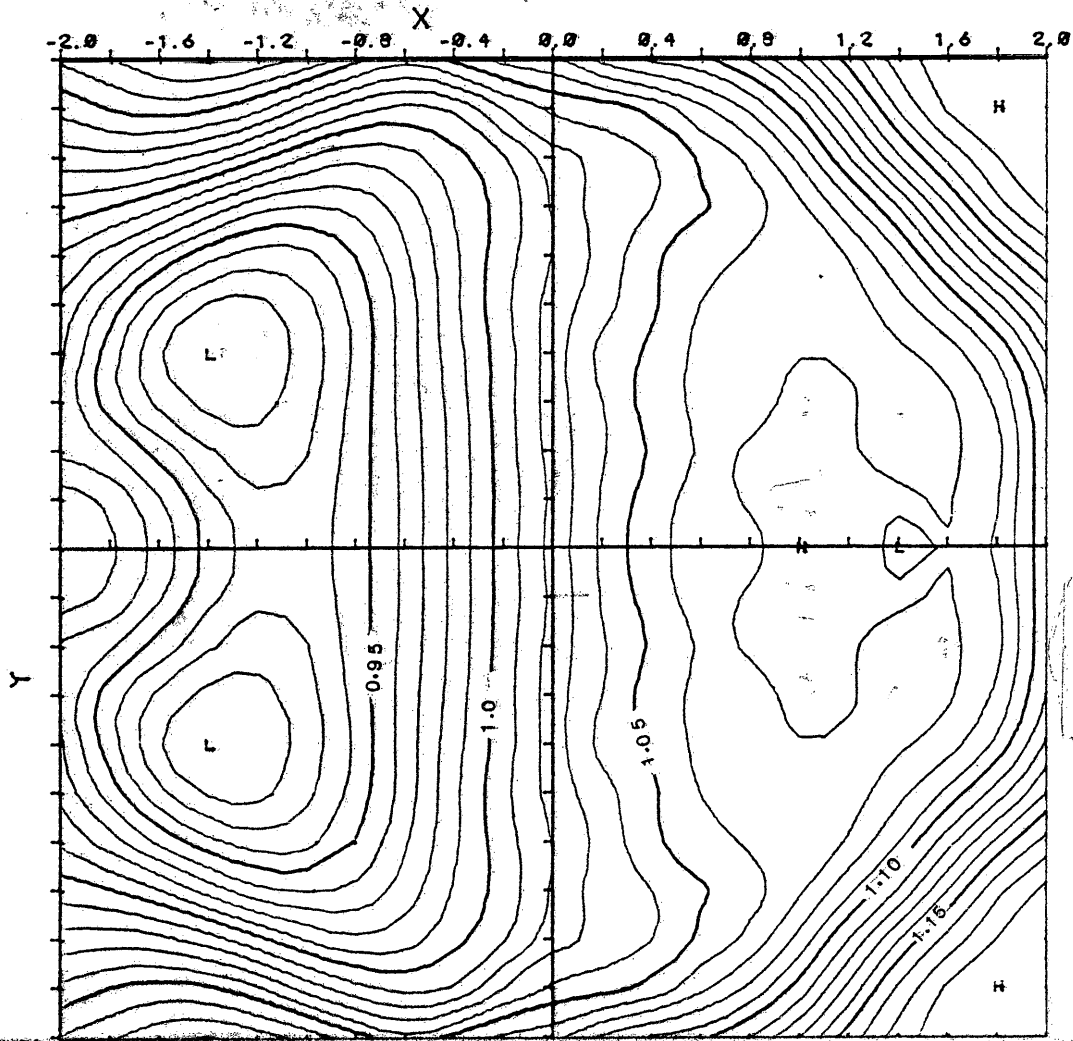
Contour map of the normalized second vertical derivative for the model shown above.

S.V.D.T., NORM., T=3.0



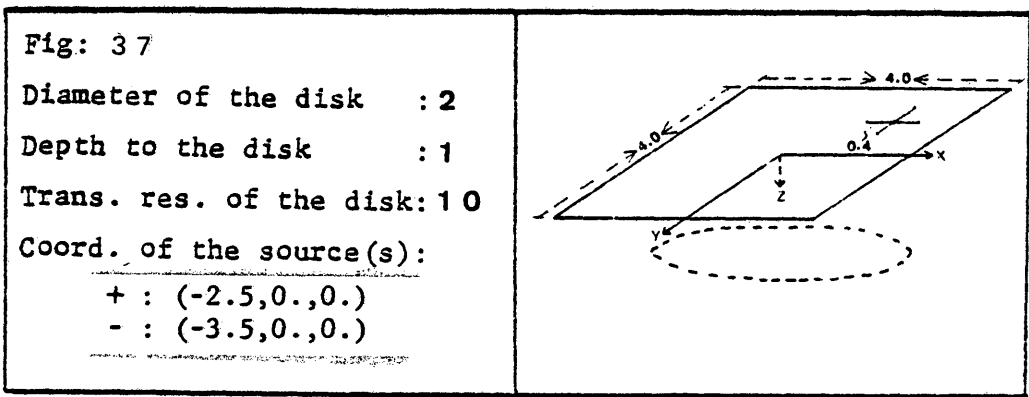
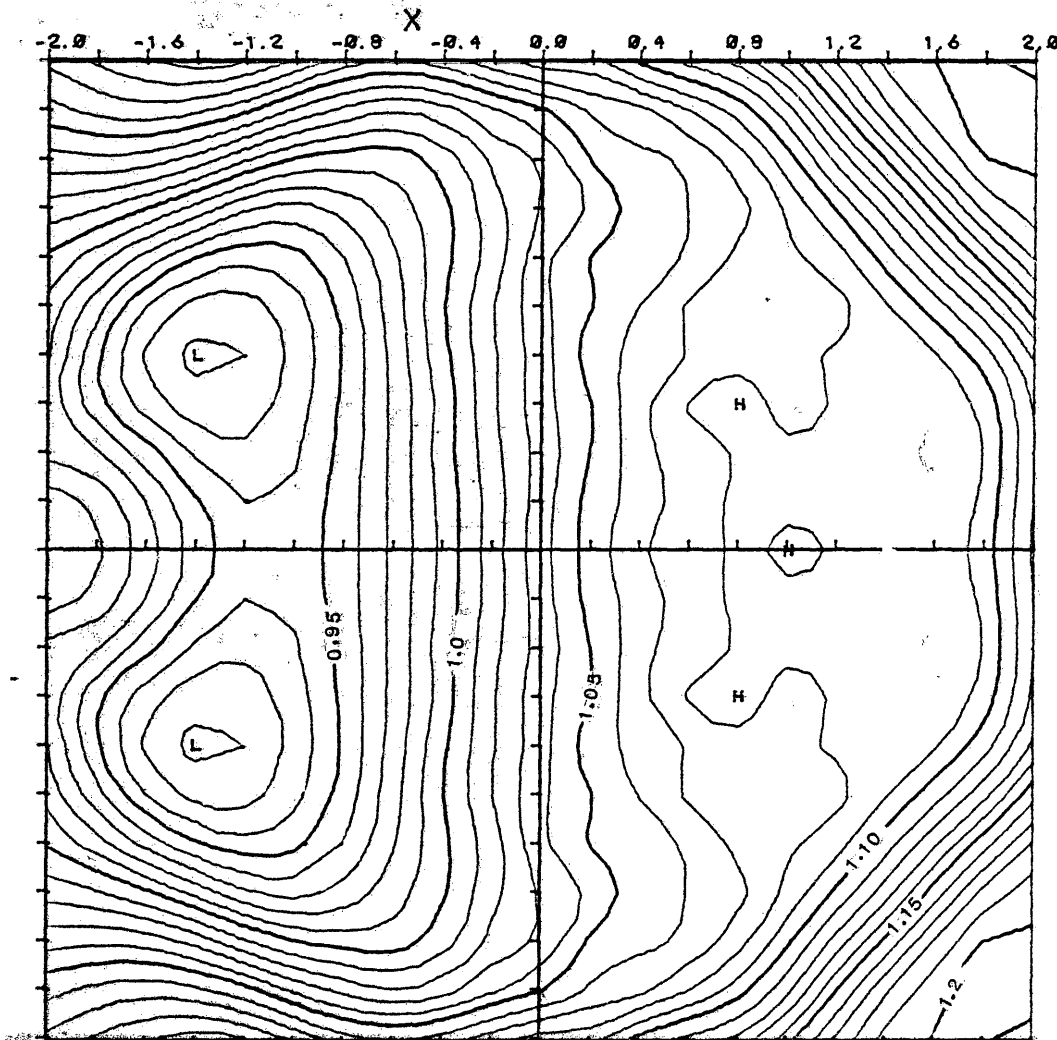
Contour map of the normalized second vertical derivative for the model shown above.

S.V.D.T., NORM., T=5.0



Contour map of the normalized second vertical derivative for the model shown above.

S.V.D.T., NORM., T=10.



Contour map of the normalized second vertical derivative for the model shown above.

table 2. The maximum response for those with T value greater than 5 is about 7 percent of the primary field. The contour maps of the second vertical derivatives for different T values are shown from Fig.38 to Fig.43. The positions of the minimum values of the second vertical derivatives are near the center of the top over the disk. The contours with unity value are approximately at the same position for different T values. These lines which contain informations about the edge of the disk are shifted toward the source. For the disks of radius two, as shown from Fig.32 to Fig.37, these lines have shifted a greater amount than that of radius one and are located at the left part of the contour maps.

When the thin layer becomes infinitely extended. The normalized second vertical derivative is shown in Fig.43 - A for $T=0.3$ case. Fig.43 - B and 43 - C show that for the thin disks with the radii of the disks being two and one respectively. We see that when the thin layer is infinitely extended, the contours are all surrounding the current electrodes. While that for the confined one, there are closed contours excluding the current electrodes.

The physical model for the electrical field of the primary and secondary sources for the thin disk is shown in Fig.44. The contours of value one correspond to those points where the secondary electrical field are perpendicular to the surface. Since the second vertical derivative is essentially associated with the curvature of tangential component of the electrical field, at those points the second vertical derivative of the total field is the same as that of the primary field. That is the normalized second vertical derivative is one at those

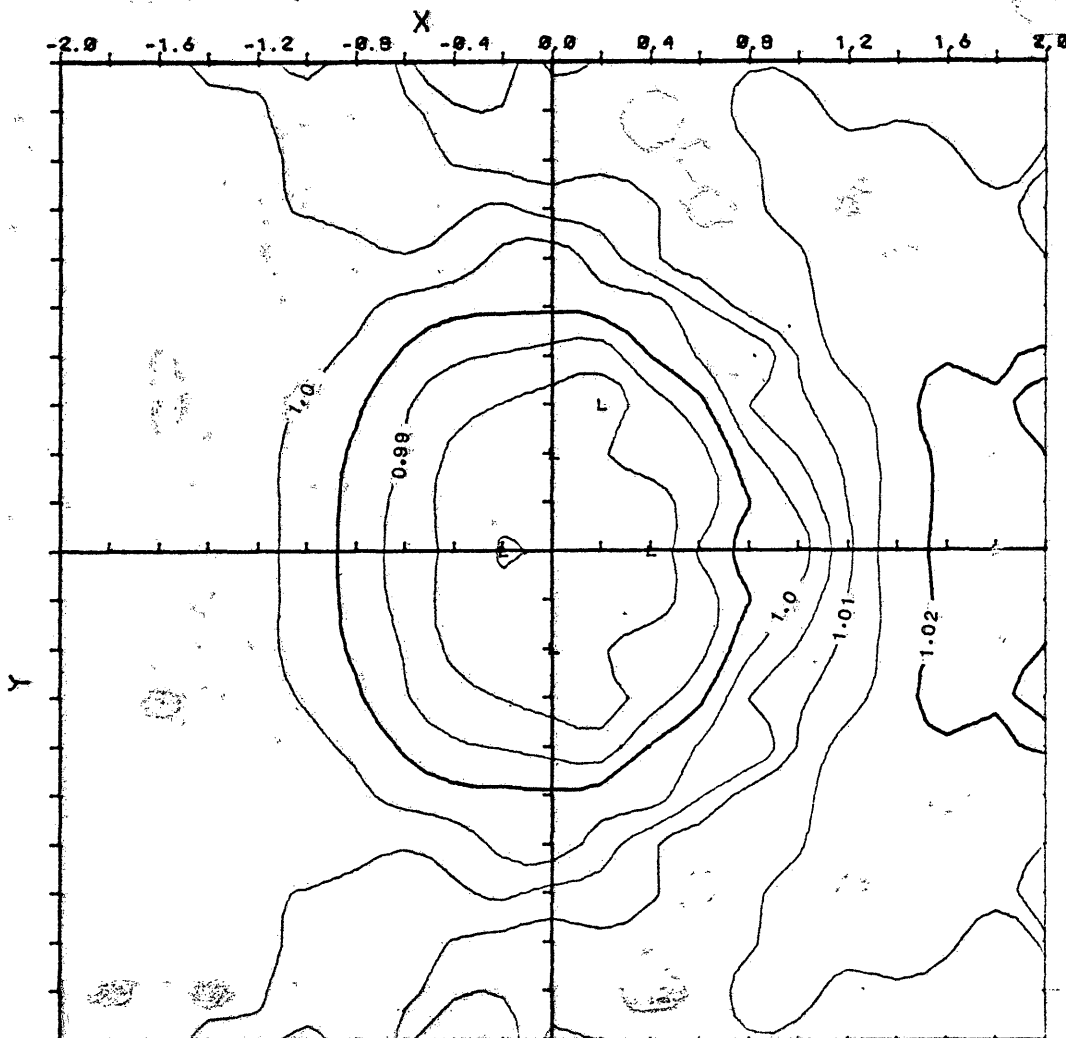
Table 1: The maximum values of the normalized secondary vertical derivative of the total field for the model shown in figure 31. The diameter of the disk is two.

T	N.S.V.D.
0.1	1.050
0.3	1.103
1.0	1.160
3.0	1.192
5.0	1.199
10.0	1.205

Table 2: The maximum values of the normalized secondary vertical derivative of the total field for the model shown in figure 31. The diameter of the disk is one.

T	N.S.V.D.
0.1	1.017
0.3	1.035
1.0	1.056
3.0	1.062
5.0	1.070
10.0	1.072

S.V.D.T., NORM., T=0.1



<p>Fig: 38</p> <p>Diameter of the disk : 1</p> <p>Depth to the disk : 1</p> <p>Trans. res. of the disk: 0.1</p> <p>Coord. of the source(s):</p> <p>+ : (-2.5, 0., 0.)</p> <p>- : (-3.5, 0., 0.)</p>	
---	--

Contour map of the normalized second vertical derivative for the model shown above.

S.V.D.T., NORM., T=0.3

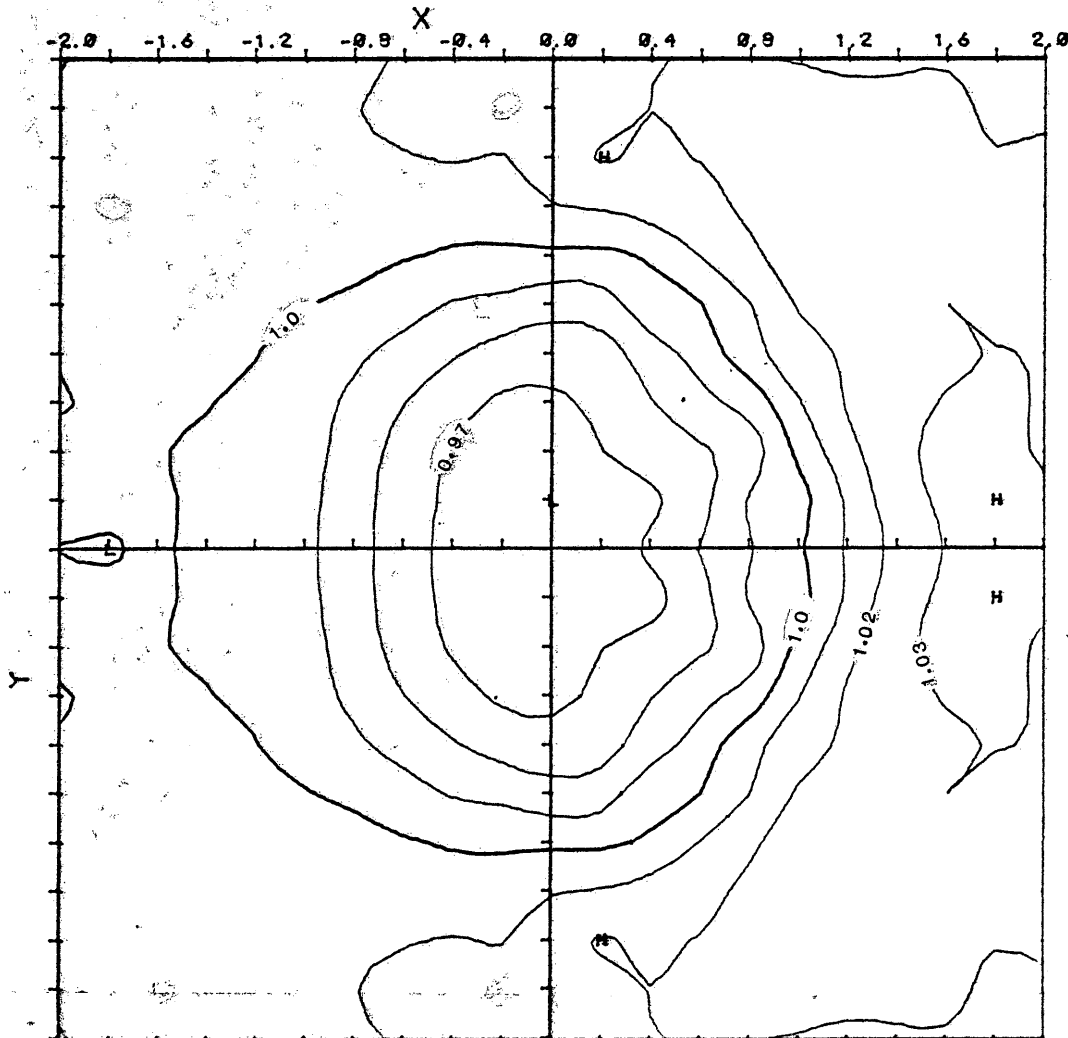
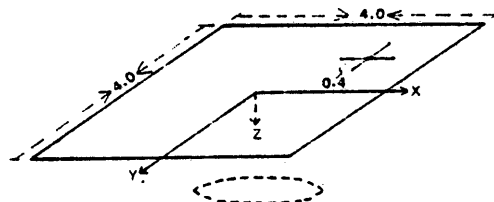


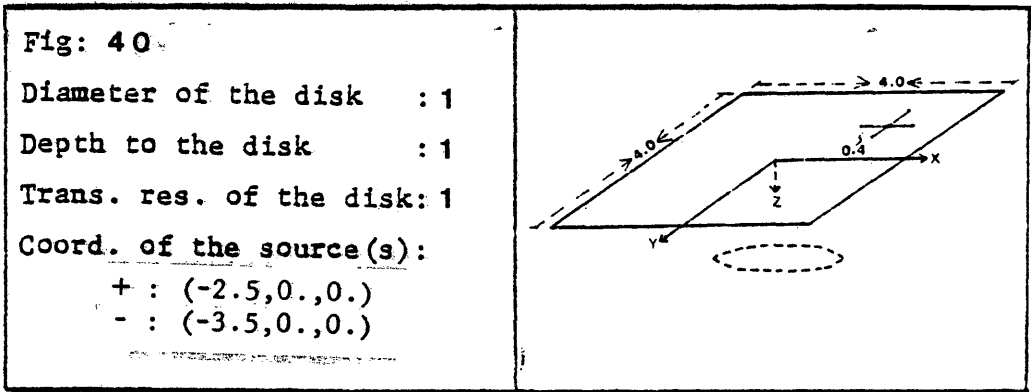
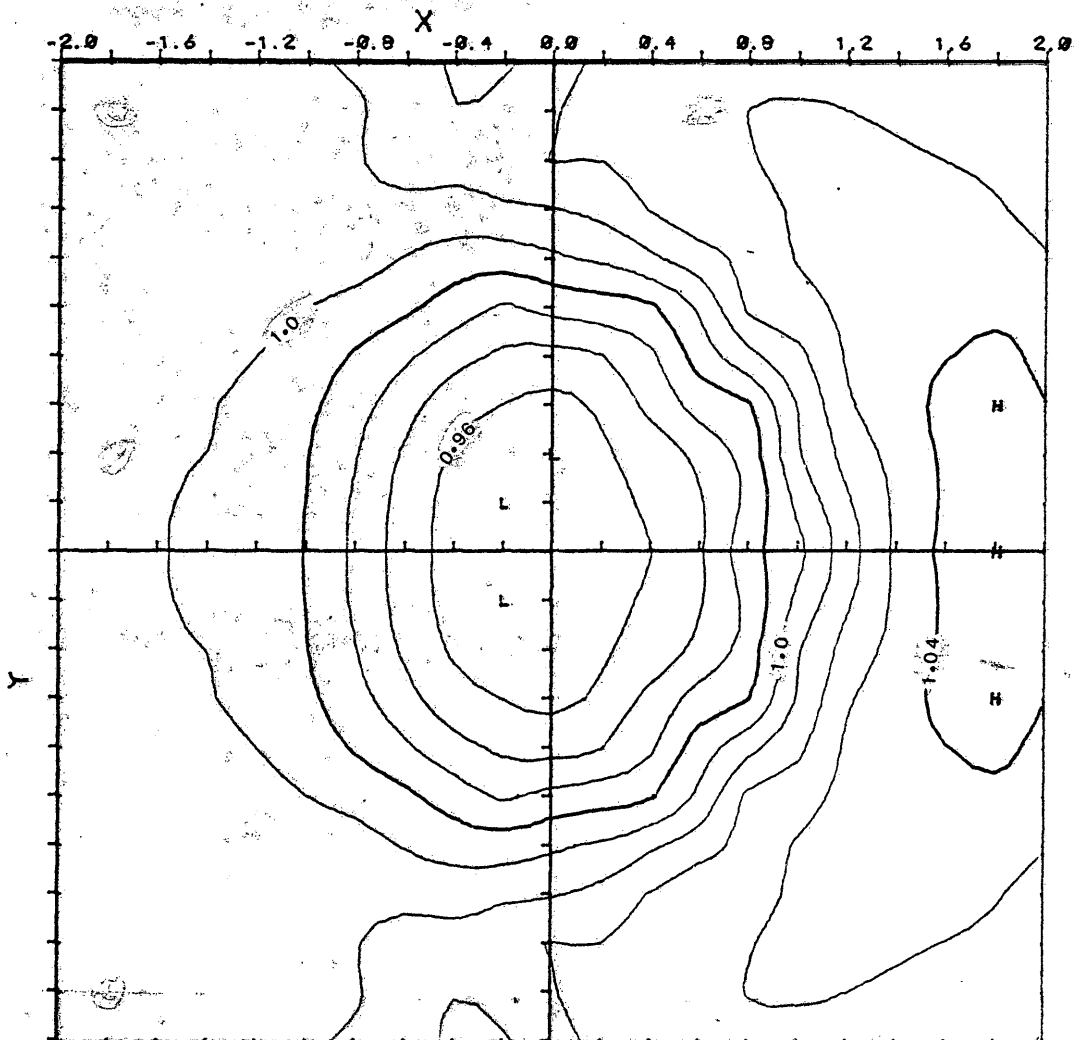
Fig: 39

Diameter of the disk : 1
 Depth to the disk : 1
 Trans. res. of the disk: 0.3
 Coord. of the source(s):
 + : (-2.5, 0., 0.)
 - : (-3.5, 0., 0.)



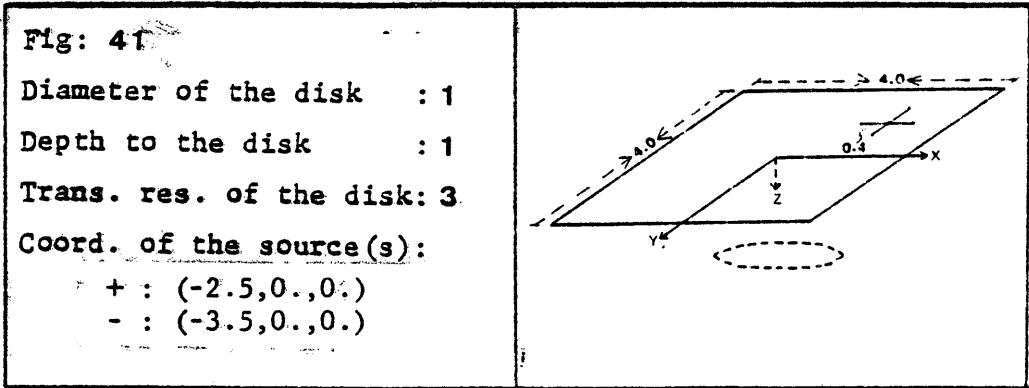
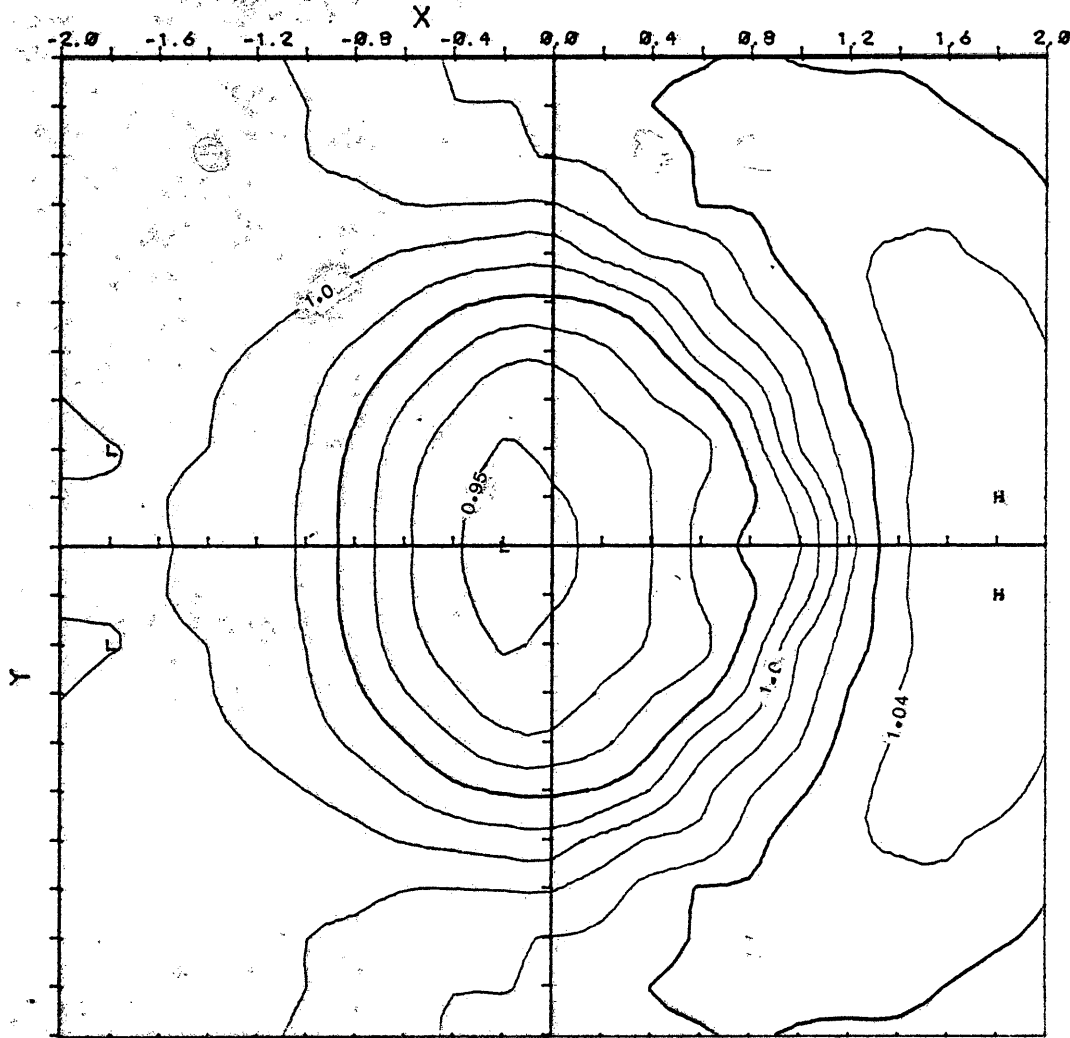
Contour map of the normalized second vertical derivative for the model shown above.

S.V.D.T., NORM., T=1.0



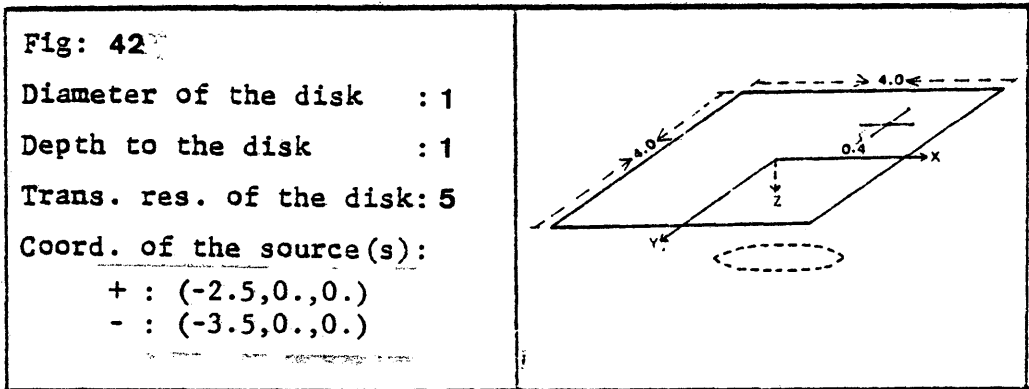
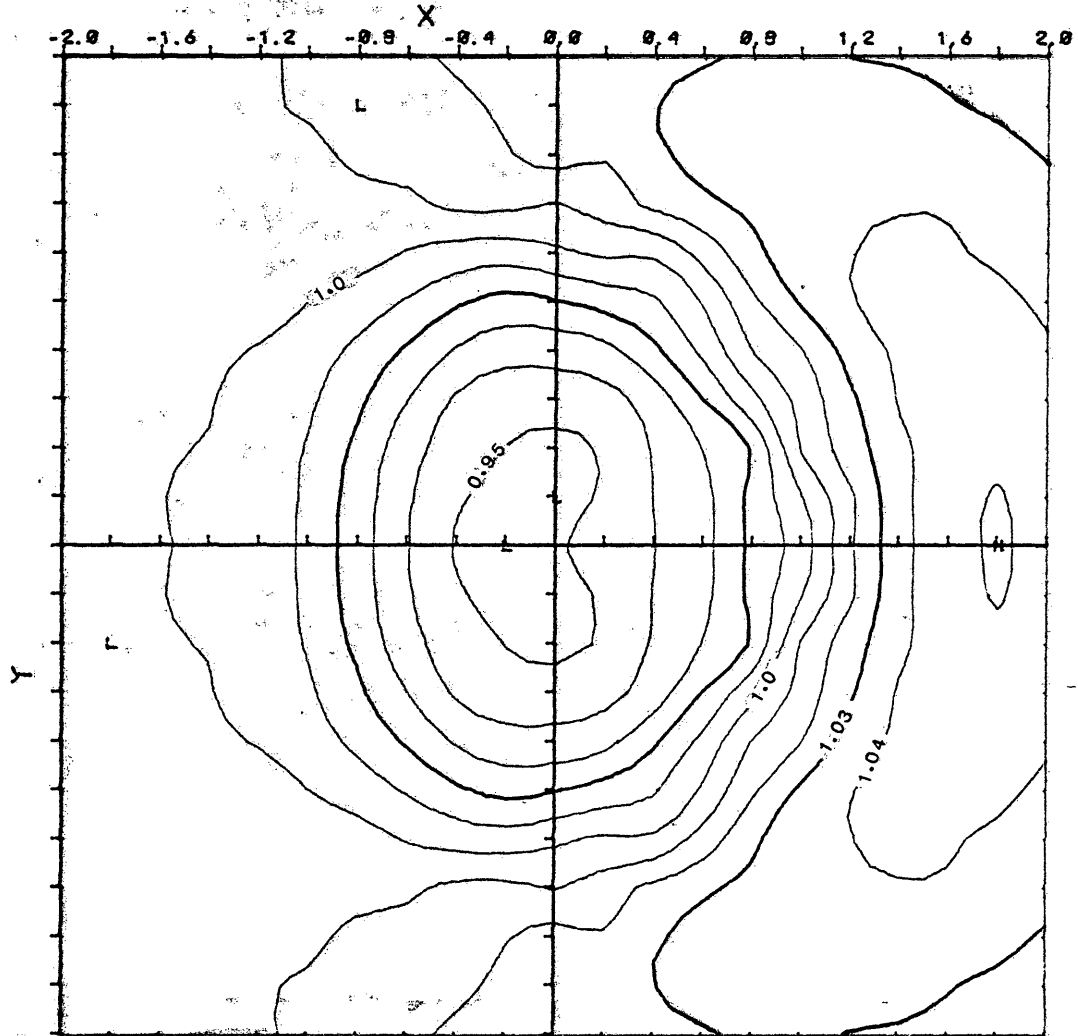
Contour map of the normalized second vertical derivative for the model shown above.

S.V.D.T., NORM., T=3.0



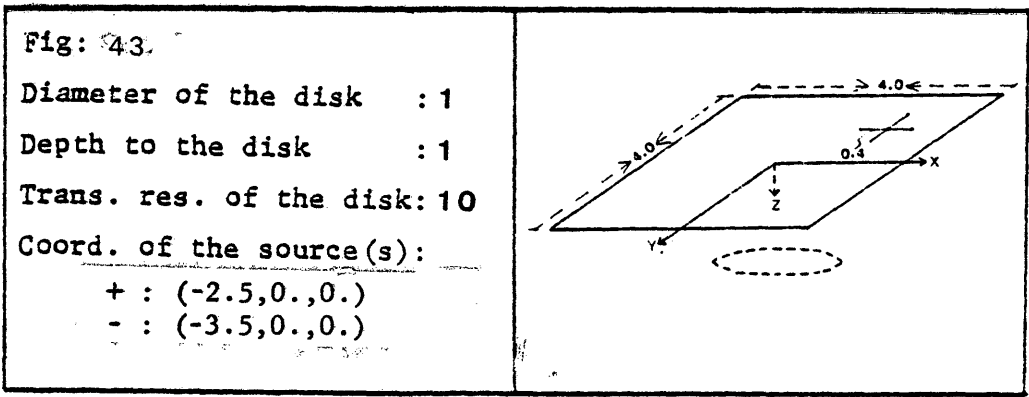
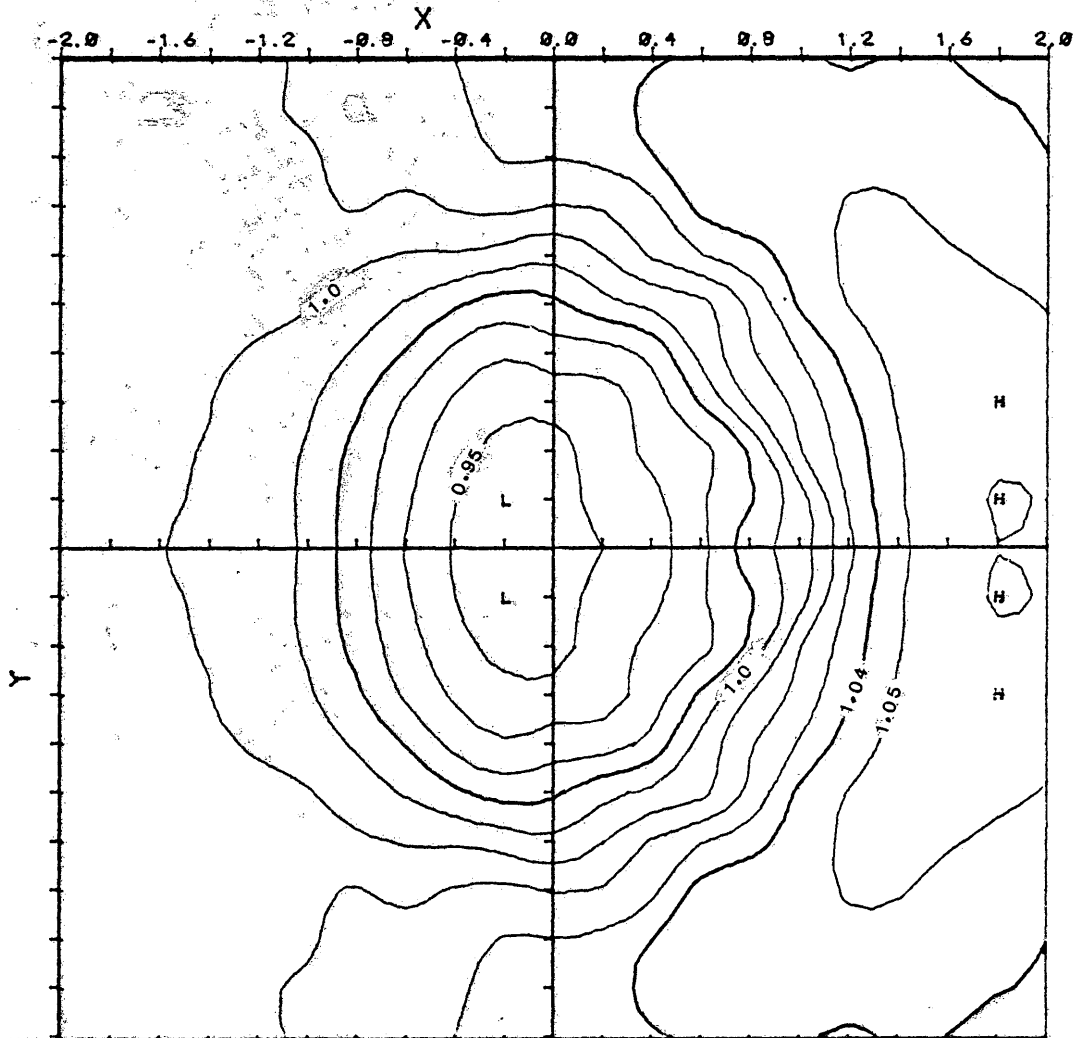
Contour map of the normalized second vertical derivative for the model shown above.

S.V.D.T., NORM., T=5.0



Contour map of the normalized second vertical derivative for the model shown above.

S.V.D.T., NORM., T=10.



Contour map of the normalized second vertical derivative for the model shown above.

S.V.D.T.T=0.3

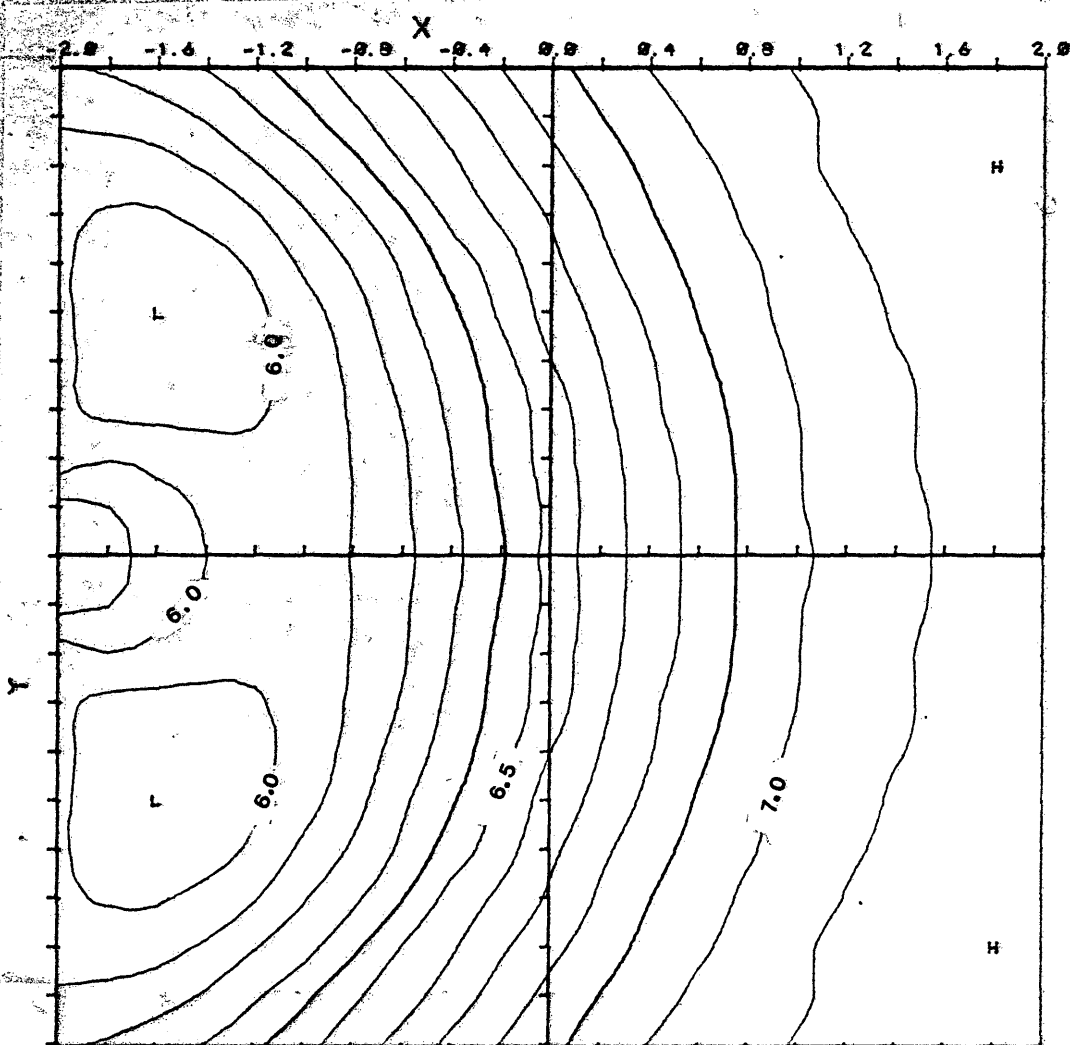


Fig.43A: Contour map of the normalized second vertical derivative for a thin horizontal layer. The depth to the layer is unity. The transverse resistance of the layer is 0.3. Source coordinates: $(-2.5, 0, 0)$, $(-3.5, 0, 0)$.

S.V.D.T, NORM., T=0.3

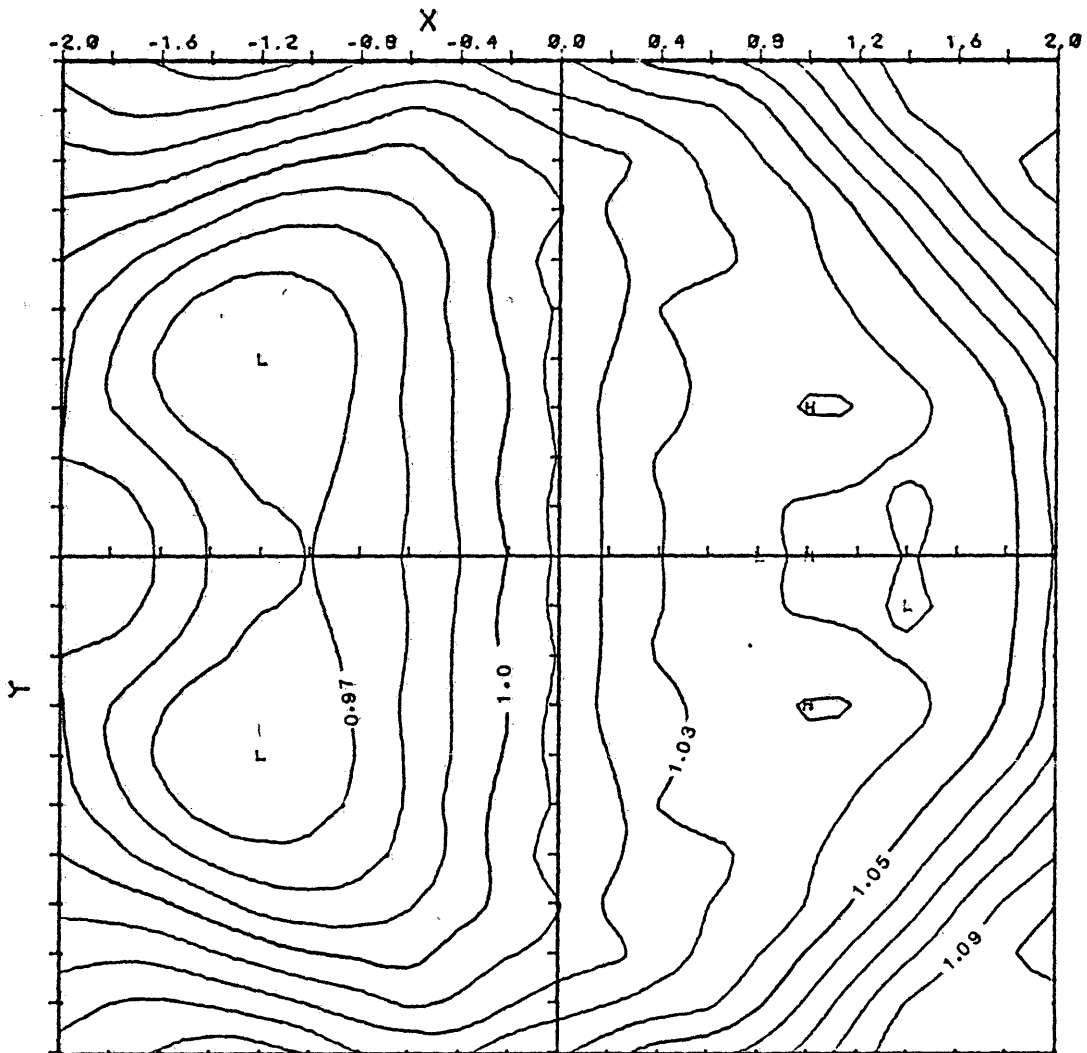
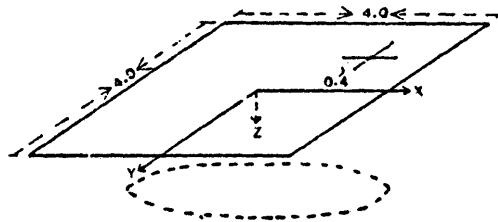


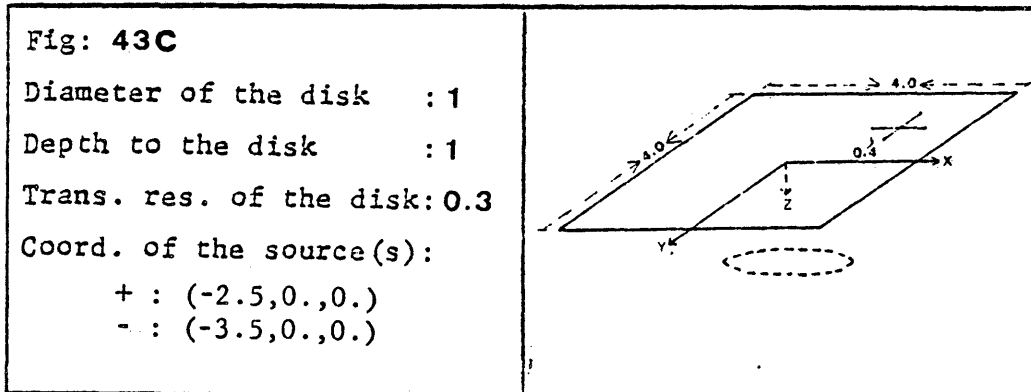
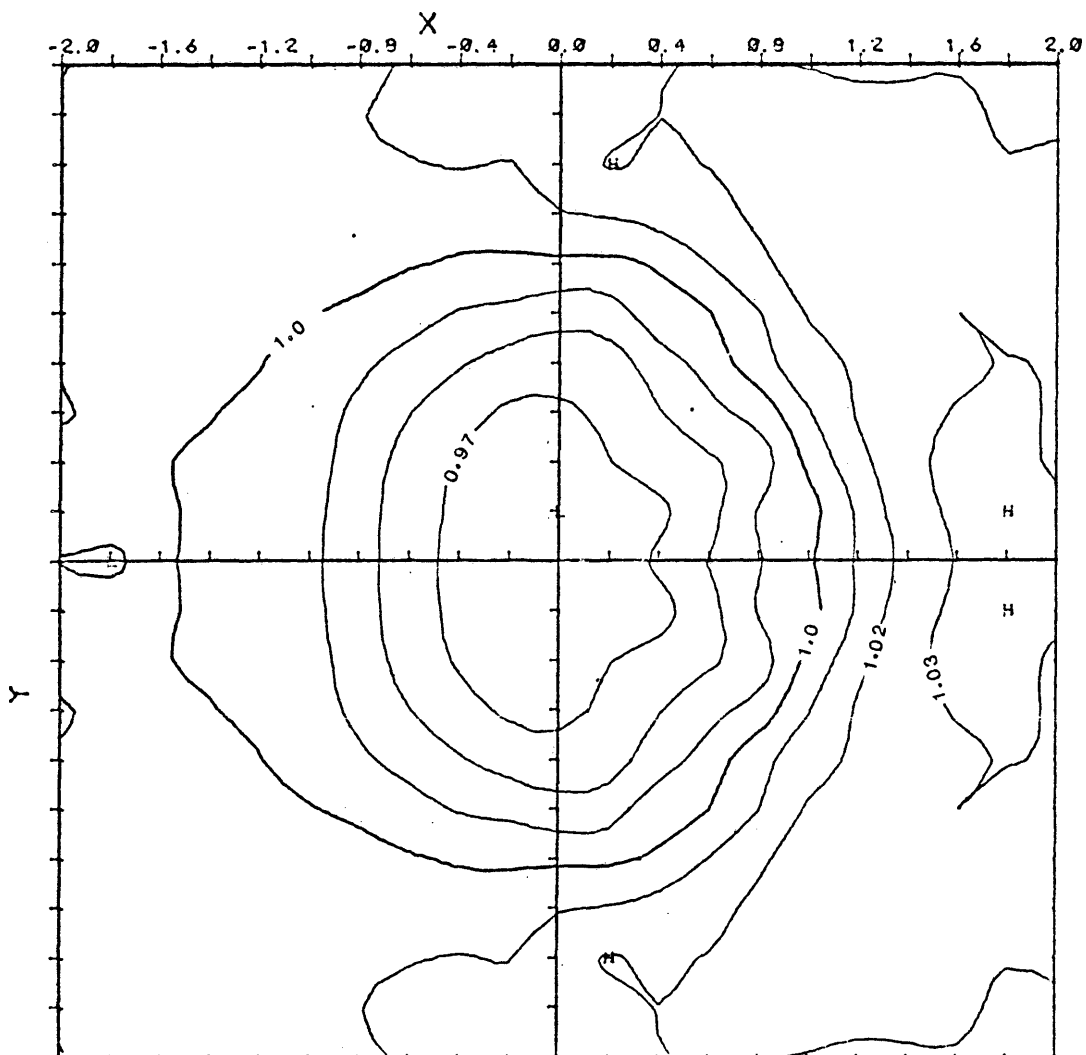
Fig: 43B

Diameter of the disk : 2
 Depth to the disk : 1
 Trans. res. of the disk: 0.3
 Coord. of the source(s):
 + : (-2.5,0.,0.)
 - : (-3.5,0.,0.)



Contour map of the normalized secondary vertical derivative for the model shown above.

S.V.D.T., NORM., $T=0.3$



Contour map of the normalized secondary vertical derivative for the model shown above.

points.

For the case of radius one, the density of the secondary electrical lines is more sparse on the surface and the shape of the contour with value one is more comparable with the shape and the position of the disk.

There is another possible index for the edge of the disk. That is the zero contour of the second vertical derivative of the total field. Note that at the surface just about the top of the edge of the disk, the tangential components of the total electrical fields are shown in Fig.44. Since the second vertical derivative is associated with the curvature of the tangential electrical field, there will be a zero contour along those points which have relative extreme values. These zero contours have been used in the potential theory to delineate the boundary of the buried targets (Peters, 1945). However, in our cases, the secondary field seems to be too small to create relative extreme points. It is then hard to get zero contours on the second vertical derivative of the total field. Therefore it will be better to examine the contours of unity value in the normalized map to get the information about the disk.

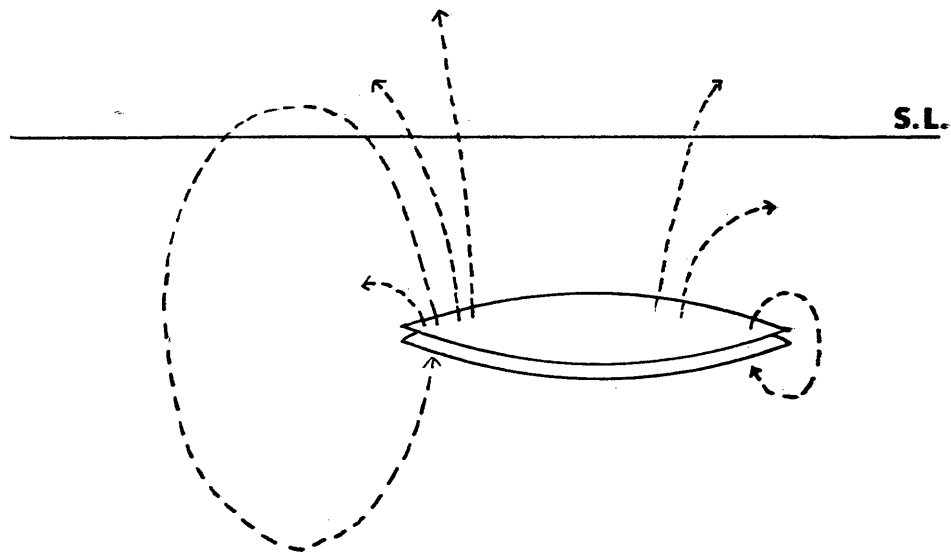
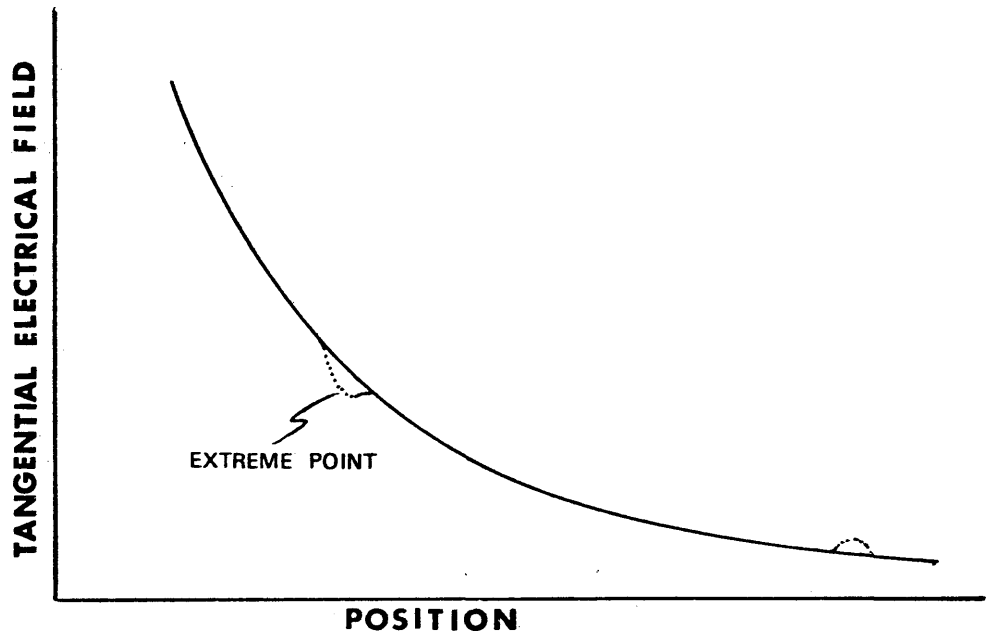


Fig.44: Physical model of the secondary electrical field from the thin disk.

T-2231

Table 3 shows the relations between the normalized vertical derivatives and the locations of the sources. Both the depth to the disk and diameter of the disk are unity. The results show the closer the sources to the disk, the greater the response. Let the current electrode be located in a downhole just above the center of the disk as shown in Fig.45. The contour maps are shown from Fig.46 to Fig.49. For those points which are located approximately on the circle of radius 0.77, the values increase sharply. Note that the second vertical derivative of the primary field has value of zero along the circle of radius 0.77 approximately as shown in Fig.50. The normalized values hence have singularities along the circle. There are two closed contours with unity value, which again are corresponding to the places where the secondary electrical field is perpendicular to the surface. The outer contour with unity value is comparable to the edge of the disk. Increase the radius of the disk to two, Fig.51 shows that there still exists two closed contours with unity value. The outer contour with unity value is now within the edge of the disk.

Let the current source be at the coordinate of $(-1.5, 0., 0.5)$ and the diameter of the disk be one. The contour map of the normalized second vertical derivative is

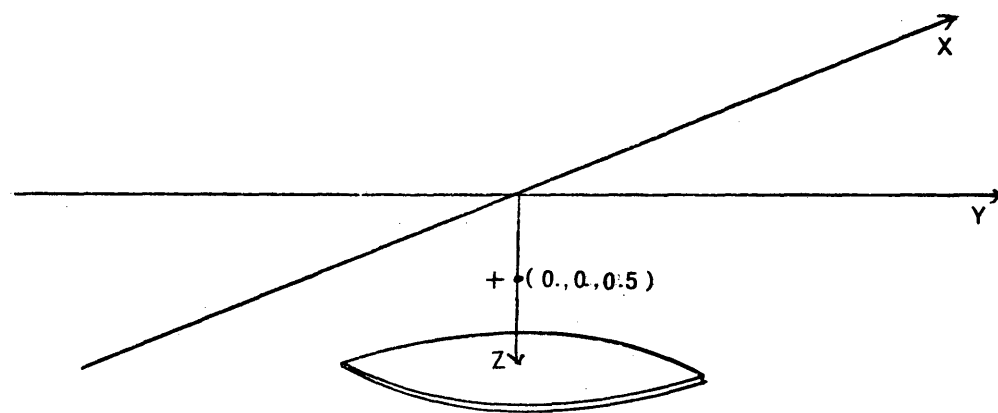
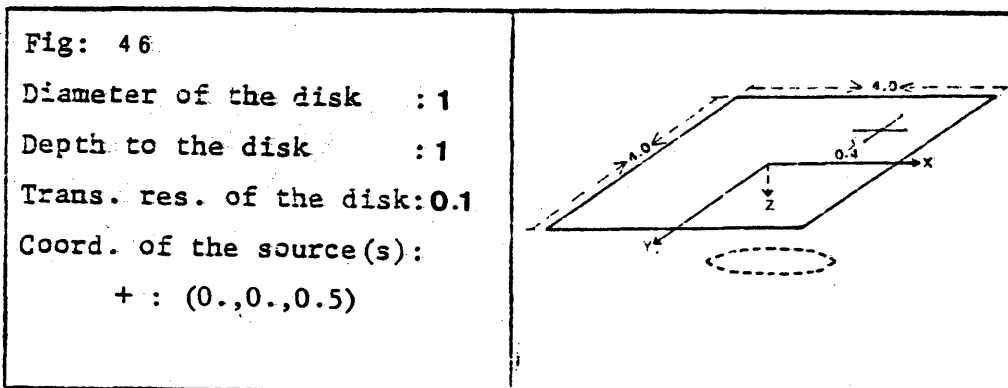
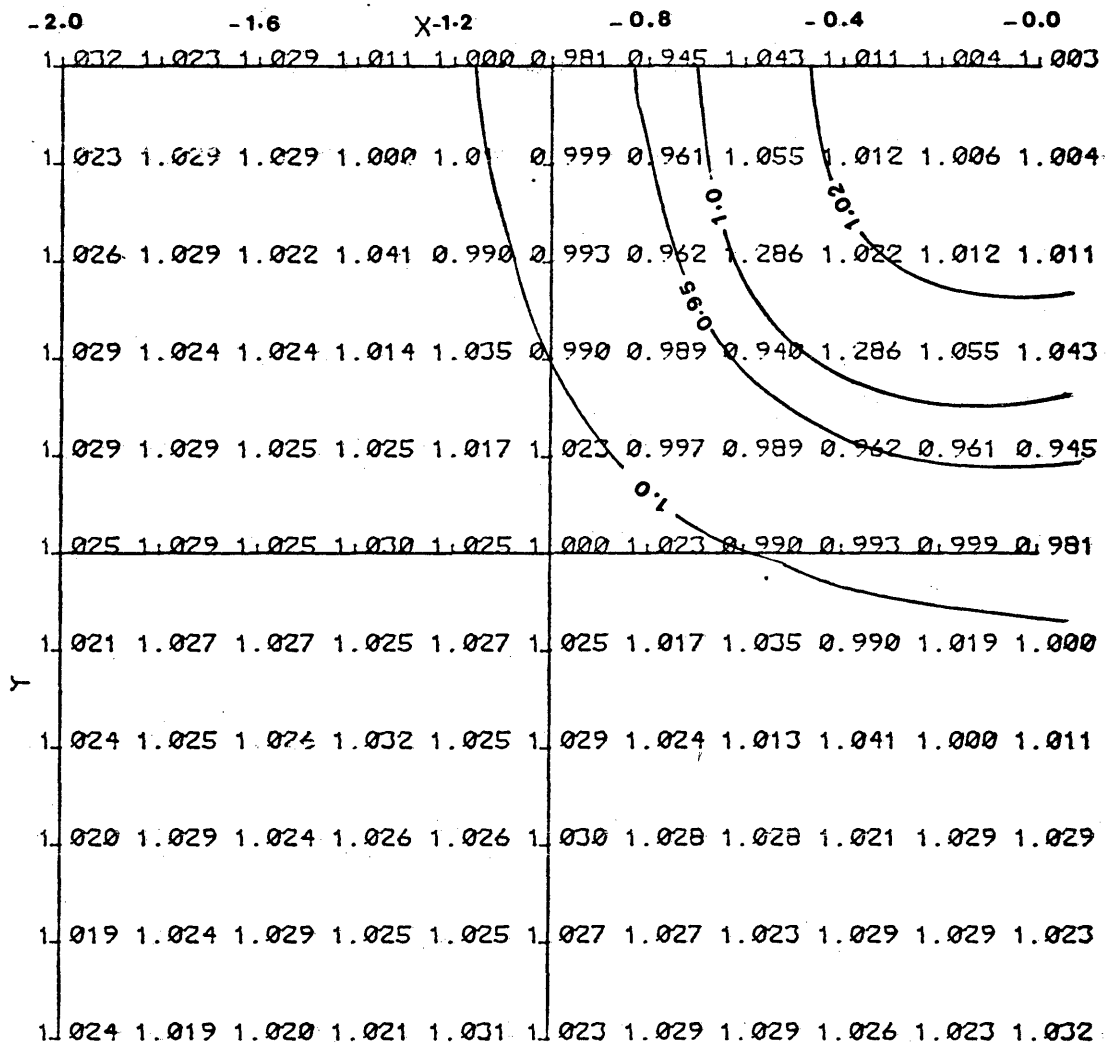


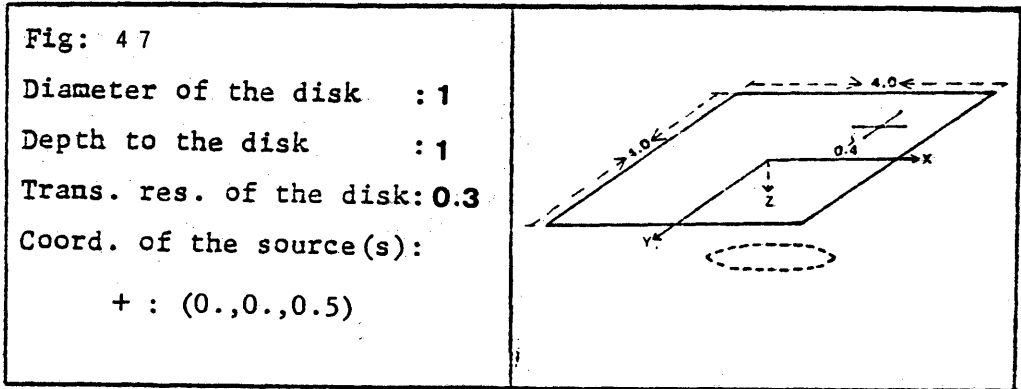
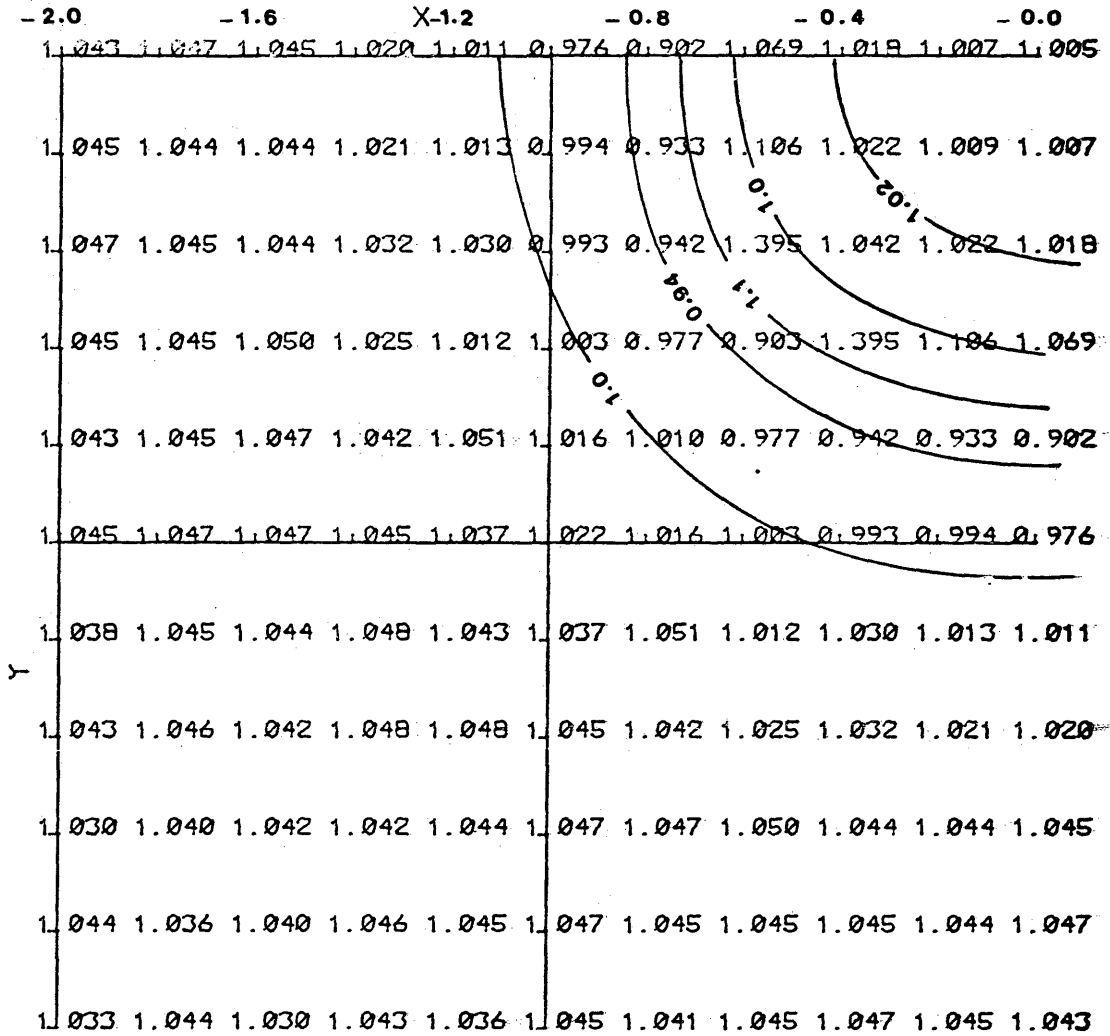
Fig. 45 : The above shows a buried current electrode and the thin disk. The second vertical derivatives are computed on the surface.

S. V. D. T. NORM. T=0.1, ZS=.5



Contour map of the normalized second vertical derivative for the model shown above.

S.V.D.T. NORM. T=0.3, ZS=-.5



Contour map of the normalized second vertical derivative for the model shown above.

T-2231

S. V. D. T. NORM. T=1.0, ZS=.5

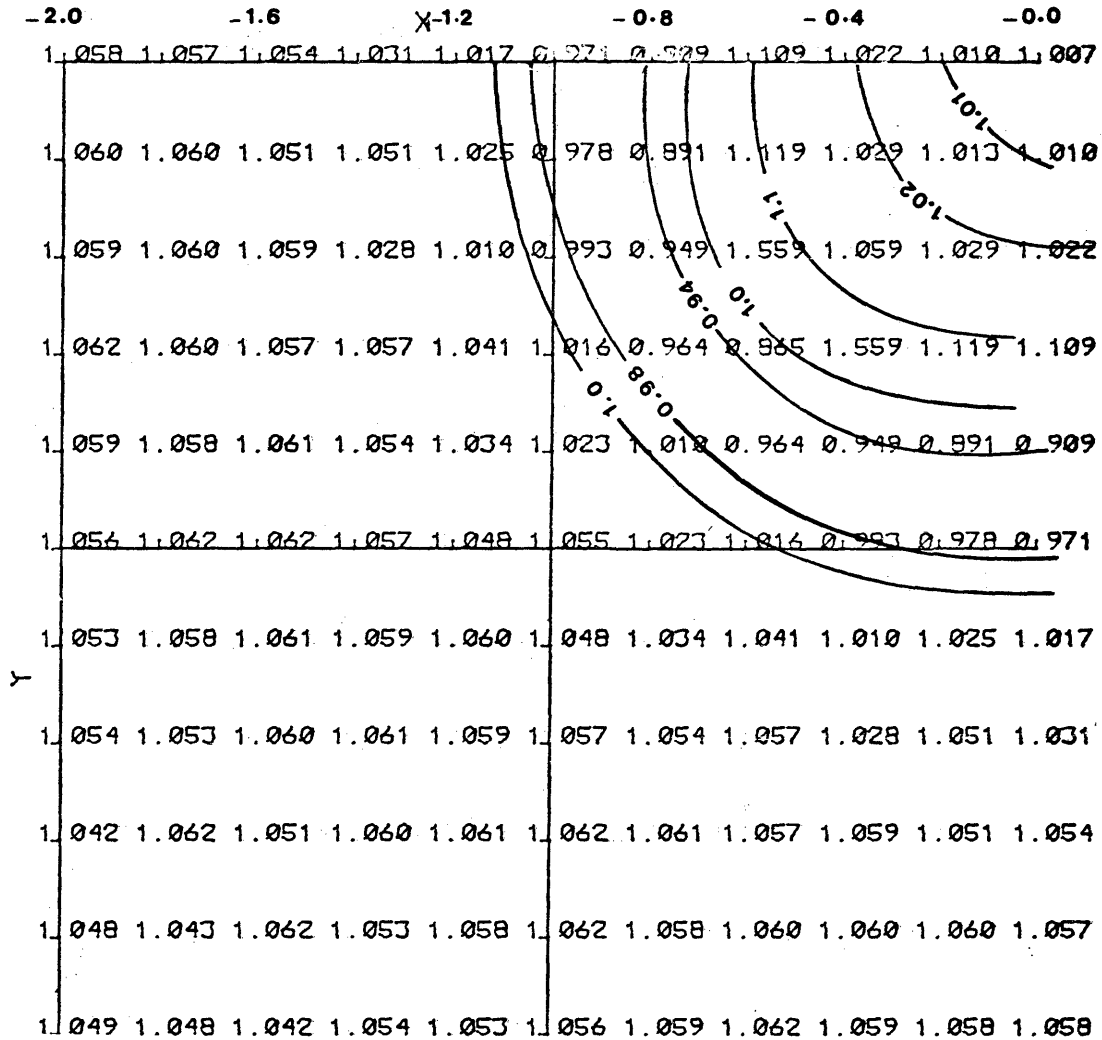
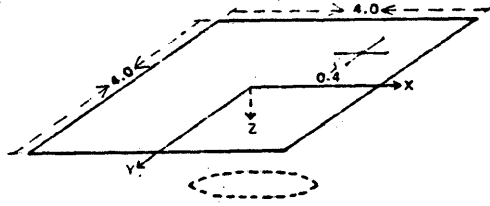


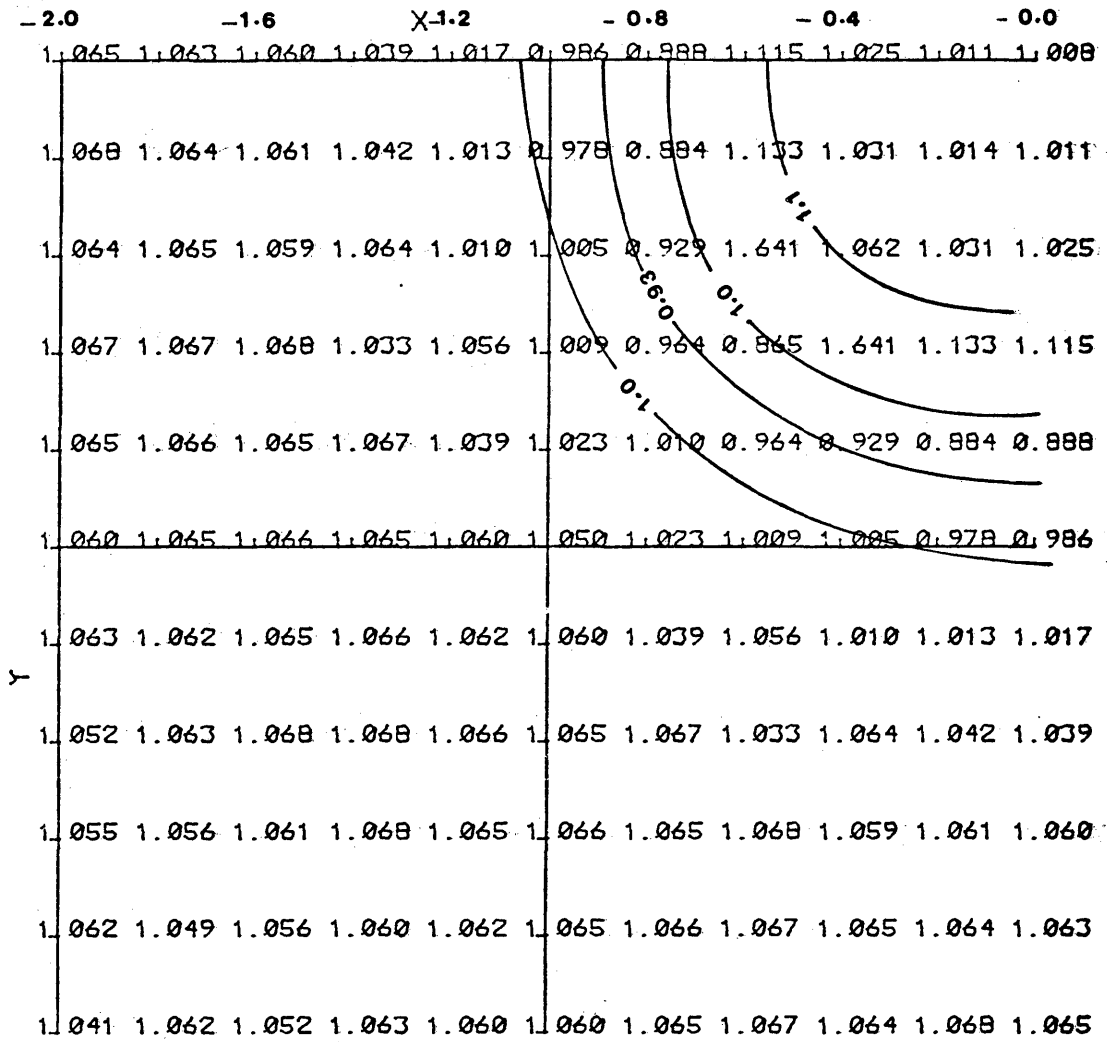
Fig: 48

Diameter of the disk : 1
 Depth to the disk : 1
 Trans. res. of the disk: 1
 Coord. of the source(s):
 + : (0.,0.,0.5)



Contour map of the normalized second vertical derivative for the model shown above.

S.V.D.T.NORM.T=3.,ZS=.5



<p>Fig: 49</p> <p>Diameter of the disk : 1</p> <p>Depth to the disk : 1</p> <p>Trans. res. of the disk: 3</p> <p>Coord. of the source(s): + : (0.,0.,0.5)</p>	
--	--

Contour map of the normalized second vertical derivative for the model shown above.

S. V. D. OF UNIF. EARTH

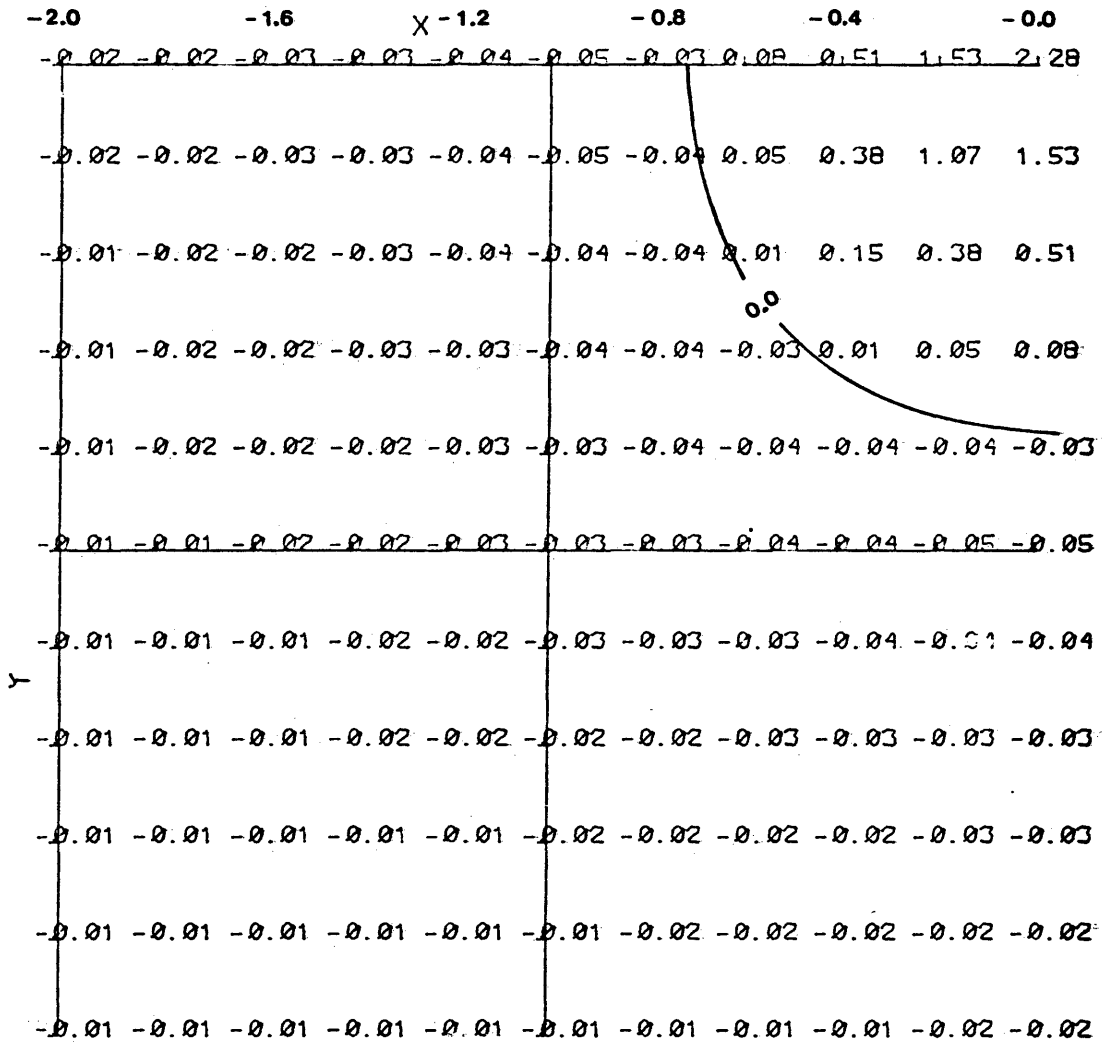


Fig. 50: The contour map of the second vertical derivative for an uniform earth. The current electrode is buried at (0.,0.,0.5).

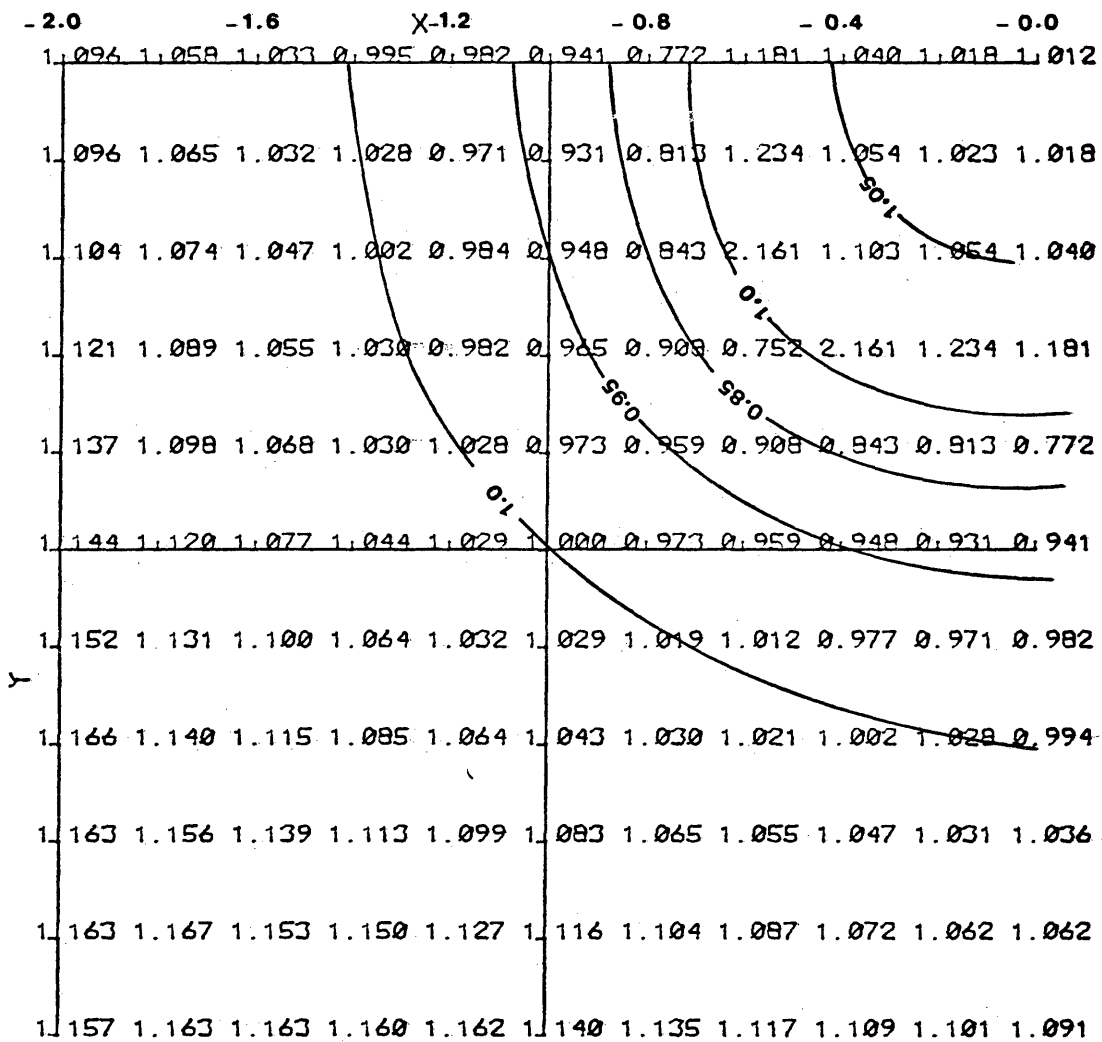
Table 3: The relations between the maximum values of the normalized secondary vertical derivatives and the sources' locations. The model is as figure 31. The transverse resistence of the disk is one.

sources' location	N.S.V.D.
-:(-2.5, 0., 0.)	1.160
-:(-3.5, 0., 0.)	
-:(-3.5, 0., 0.)	1.115
-:(-4.5, 0., 0.)	
-:(-4.5, 0., 0.)	1.094
-:(-5.5, 0., 0.)	

Table 4: The minimum values of the normalized secondary vertical derivative of the total field for the model shown in figure 31 with different T values. The current electrode is buried.

T	N.S.V.D.
0.1	0.940
0.3	0.902
1.0	0.865
3.0	0.865

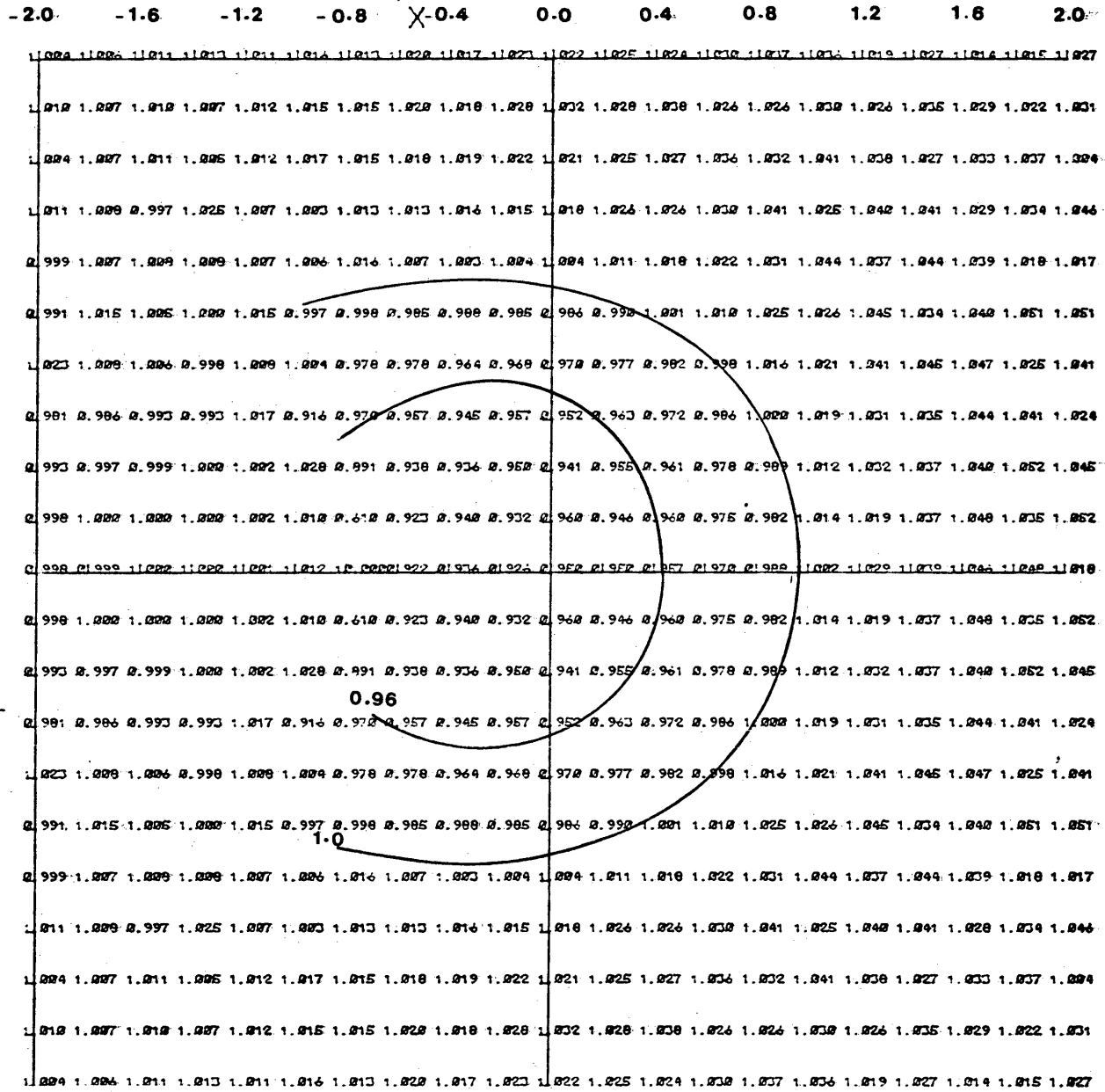
S.D.V.T.ZS=.5,T=1.



<p>Fig: 51</p> <p>Diameter of the disk : 2</p> <p>Depth to the disk : 1</p> <p>Trans. res. of the disk: 1</p> <p>Coord. of the source(s):</p> <p>+ : (0.,0.,0.5)</p>	
---	--

Contour map of the normalized second vertical derivative for the model shown above.

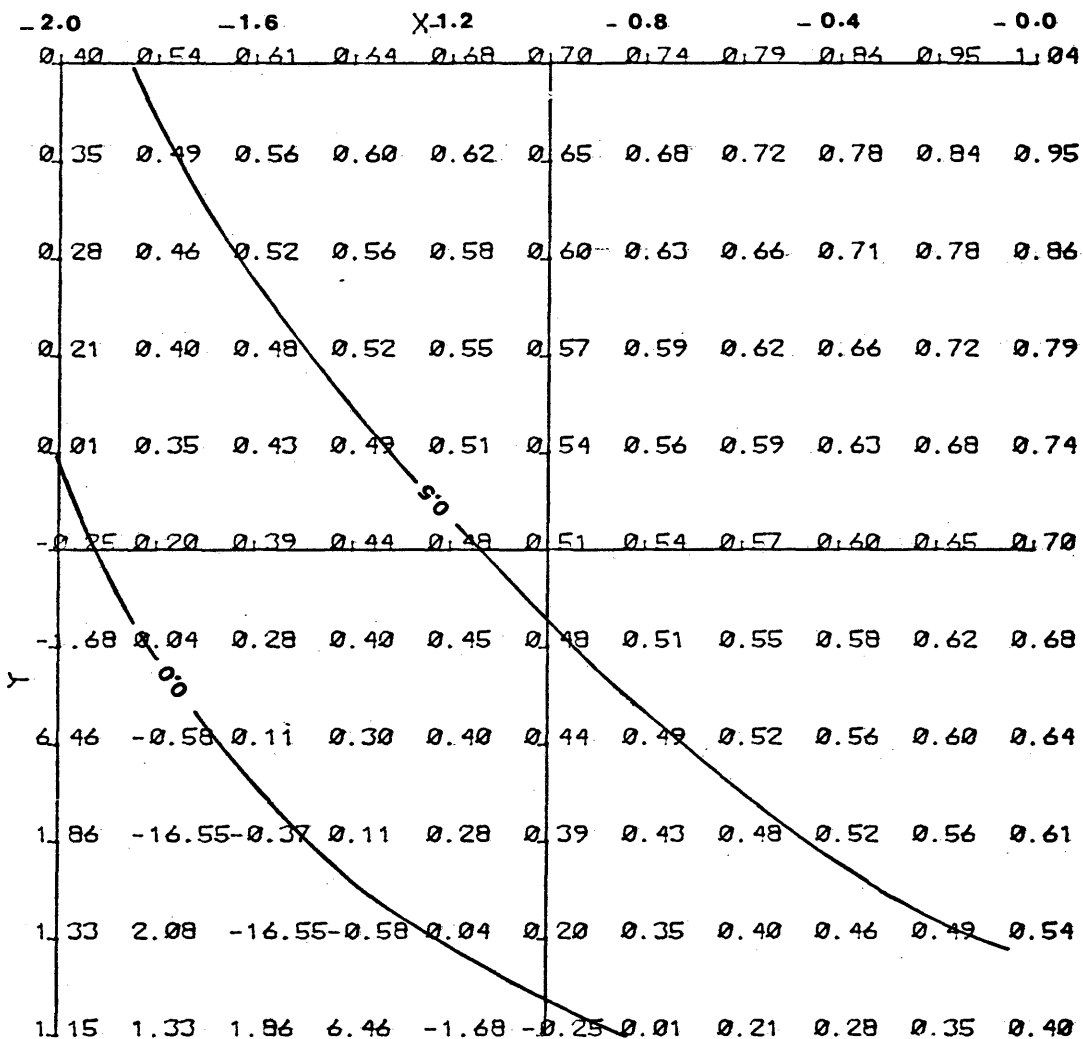
$S=(-1.5, 0, .5), T=1.$



<p>Fig. 52</p> <p>Diameter of the disk : 1</p> <p>Depth to the disk : 1</p> <p>Trans. res. of the disk: 1</p> <p>Coord. of the source(s): + : (-1.5, 0., 0.5)</p>	
--	--

Contour map of the normalized second vertical derivative for the model shown above.

$S=(0.,0.,1.5)$.S.V.D.T. , $T=0.1$



<p>Fig: 53</p> <p>Diameter of the disk : 1</p> <p>Depth to the disk : 1</p> <p>Trans. res. of the disk: 0.1</p> <p>Coord. of the source(s):</p> <p style="padding-left: 40px;">+ : (0.,0.,1.5)</p>	
--	--

Contour map of the normalized second vertical derivative for the model shown above.

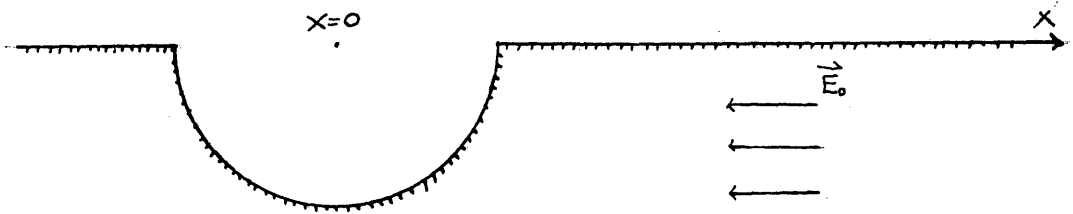


Fig. 54: The above shows the testing model for calculating the topography response.

TOPOGRAPHY EFFECT
SOLID LINE: ANALYTIC

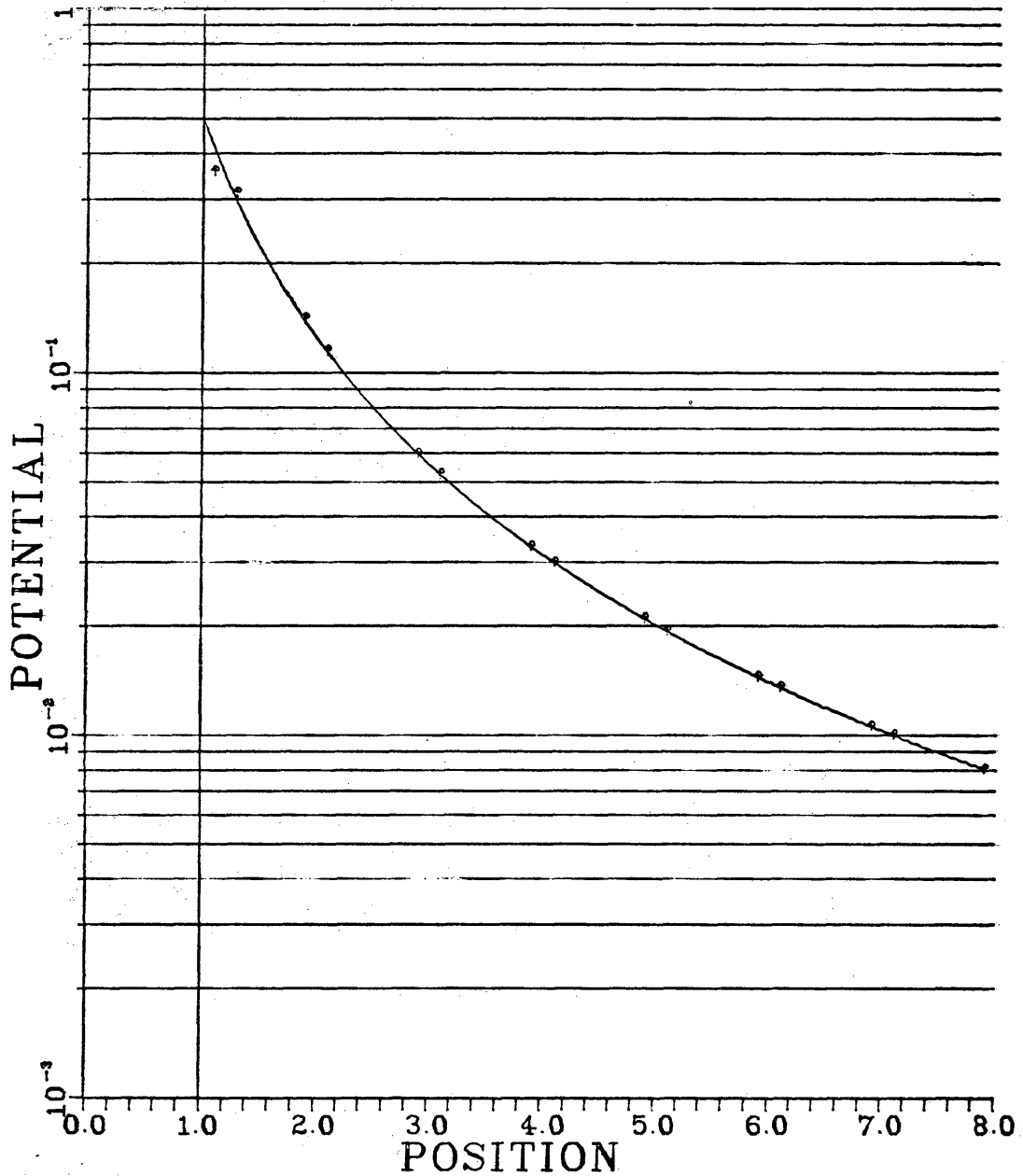


Fig. 55. The symbols represent the numerical results of the modeling for irregular surface as shown in Fig. 55. The solid line represents the analytic solution.

shown in Fig.52. There is now only one contour with unity value, which is comparable to the edge of the disk. Fig.53 is the case that the current electrode is buried deeper than the thin layer. The secondary electrical fields are strong enough compared with the primary field to create relative extreme points which correspond to the zero contour of the map.

Uniform Earth with Irregular Surface

In order to test the accuracy of the program which is to model the response of an uniform earth with irregular surface, we use the model as shown in Fig.54. The analytical solution can be considered as a special case of either the one shown in Appendix 1 or the one shown in Appendix 2. The comparison of the numerical result with the analytical solution is shown in Fig.55. The corrected geometric factor is defined as the response of an uniform earth with irregular surface. The program can be applied for obtaining the corrected geometric factor. However, it is not our intension to discuss the topography correction in this paper.

CHAPTER 9: CONCLUSIONS

Contour maps of the normalized second vertical derivative for arbitrarily shaped three dimensional thin layers can be produced. A positive response depends on the transverse resistance, the depth and the extent of the thin layer and the locations of the current sources. The greater the value of the transverse resistance and the greater the extent of the layer, the stronger the response. The deeper the disk and the farther the sources, the smaller the response. Two contours have been suggested for delineating the boundary of the thin layer from the maps. They are the contours of unity and zero values. However the interpretation from these contours needs some imagination about the secondary electrical field of the targets. The rule of thumb is that the further the current sources are away from the disk, the better the contour of unity value matches with the edge of the disk. The zero contours more likely occur when using the buried current electrodes, especially for the case in which the current electrode is buried deeper than the targets.

In the integral equation approach, the sources on the surface of the thin layer are expressed in terms of dipoles.

on a single sheet to which the thin layer approaches. The sheet is then divided into rectangular facets. When the sheet has curvature, it is divided into trapezoids which are then approximated by simultaneous linear equations which can be solved by standard matrix techniques. The program calculates the potential at any point once the sources are set at any point far away from the thin layer compared with the thickness of the layer.

The fields shown in this thesis are computed using the second vertical derivative of the potential. Since the second vertical derivative is essentially a high pass filter and since the signal from the surrounding medium is predominantly in the low spacial harmonics, the signal from the confined target is enhanced.

All the results shown are for thin bodies in a homogeneous earth. The theory for the thin layer along the boundaries of two media can be developed. However, due to the infinite extent of the boundaries of the media and the limitation of the computer storage, it is difficult to program on a Digital Equipment Corporation PDP-10 computer. It would be a relatively simple extension to model the response for a two dimensional case.

Practical limitations of the applications of the integral equation approach are set by the size and speed of the available computer. The method provides a powerful means of modeling the resistivity response of arbitrarily shaped thin layers, for which formal analytical solutions can not be derived and for which the numerical results from resistivity modeling programs for arbitrarily shaped bodies can not be obtained accurately.

APPENDIX 1: ANALYTIC SOLUTION OF AN IMPERFECT THIN SPHERE
IN AN UNIFORM FIELD

In order to check the accuracy of the numerical results about the imperfect thin insulators, we will consider the analytical solution of an imperfect thin insulating half sphere immersed just below a homogeneous half space subjected to a point charge located on the earth surface, as shown in figure 24. From the image theory, the field due to the above half space configuration is the same as that due to an imperfect thin insulating sphere in a homogeneous whole space subjected to a point charge which has twice amount of charges as that for the half space case.

The analytic solution for a sphere which has different resistivity from that of the surrounding homogeneous medium subjected to a point charge can be seen in many textbooks (e.g. page 204, Stratton, 1941). The solutions for the fields outside and inside the sphere are expressed by two series associated with Legendre functions separatedly. The coefficients of the series are found by matching the boundary conditions across the surface of the sphere. The analytic solution for the case of an imperfect thin insulating sphere can also be got in the same way except

that the coefficients of the series are now found by matching different boundary conditions.

If the point charge is located very far away from the sphere, the electric field around the sphere due to the point charge can be considered as uniform. The series of the analytic solution of the total potential around the sphere is then reduced to one term only.

In the following, we will consider a more general case which we will allow the resistivities inside and outside the imperfect thin insulator to be different. As can be seen from many textbooks, the potential inside and outside the sphere, in the spherical coordinate system subjected to a uniform field can be expressed by

$$\begin{aligned} U^+ &= U_s^+ + U_p^+ \\ &= \sum_{n=0}^{\infty} \frac{b_n}{r^{n+1}} P_n(\cos \theta) + E_0 r \cos \theta \end{aligned} \tag{A1-1}$$

$$U^- = \sum_{n=0}^{\infty} a_n r^n P_n(\cos \theta) \tag{A1-2}$$

where the point charge is located at $\theta=90^\circ$ axis and a_n , b_n are coefficients, and

U_s^+ represents the secondary field outside the sphere

U_p^* represents the primary field outside the sphere

P_n are the Legendre functions of n-th order

E_0 is the uniform primary electric field.

A manipulation of the coefficients from the boundary conditions, Eq.(6-10) and (6-11), leads to

$$a_0 = b_0 = 0 \quad (A1-3)$$

$$a_n = b_n = 0 \quad n > 0 \quad (A1-4)$$

$$a_1 = \frac{\rho_2}{\rho_1} \left(-2 \frac{TE_0 - E_0 R (\rho_1 - \rho_2)}{2T + R(\rho_1 + 2\rho_2)} + E_0 \right) \quad (A1-5)$$

$$b_1 = \frac{TE_0 - E_0 R (\rho_1 - \rho_2)}{\frac{2T}{R^3} + \frac{1}{R^2} (\rho_1 + 2\rho_2)} = \frac{TR^3 - R^4(\rho_1 - \rho_2)}{2T + R(\rho_1 + 2\rho_2)} E_0 \quad (A1-6)$$

where R is the radius of the sphere and T is the transverse resistance of the thin layer.

If the resistivities inside and outside the sphere are the same, then Eq.(A1-5) and (A1-6) can be reduced to

$$a_1 = \frac{-2TE_0}{R \left(\frac{2T}{\rho_1 R} + 3 \right)} + E_0 \quad (A1-7)$$

$$b_1 = \frac{\frac{T}{\rho_1} E_0}{2 \frac{T}{\rho_1 R} + 3} R^2 \quad (A1-8)$$

If the transverse resistance is zero, Eq.(A1-5) and (A1-6) then can be reduced to:

$$a_1 = \frac{3 \rho_2}{\rho_1 + 2 \rho_2} E_0 \quad (A1-9)$$

$$b_1 = \frac{\rho_2 - \rho_1}{\rho_1 + 2 \rho_2} R^3 E_0 \quad (A1-10)$$

which are exactly the solutions around a sphere having a different resistivity from that of the surrounding homogeneous medium subjected to an uniform primary field.

In the numerical computation of the potential, we have assumed that the potentials at infinity from the sources are zero. For the case of the uniform primary field, the sources are located at infinity. The fields due to the primary sources are no longer regular at infinity for both the analytic case and the numerical case. However, the secondary fields of the numerical results are calculated on the basis that the fields vanish at infinity. The secondary field of the analytic results are expressed in spherical harmonic series which vanish at infinity. Thus, for the secondary fields both the analytic case and the numerical case have reference point at infinity.

T-2231

Now we are going to investigate the zero order term of the induced dipole on the sphere subjected to an uniform primary field. That is to find the new expression for the first term on the right hand side of Eq.(3-43) while the primary field is uniform. For the point primary source, the amount of charge in the equivalent whole space case is $2I\rho_e$. The electric field at point m is

$$E_m = \frac{2I\rho_e}{4\pi} \frac{\vec{r}}{r_{Am}^2} \quad (\text{A1-11})$$

The zero order dipole moments induced at point m are

$$\xi_m^0 = -\frac{T}{\rho_e} \vec{E}_m \cdot \vec{n}_m \quad (\text{A1-12})$$

where \vec{n}_m is the normal direction of the surface at point m, which points outward from the body. With \vec{E} being uniform, we get

$$\xi_m^0 = -\frac{T}{\rho_e} E \vec{v} \cdot \vec{n}_m \quad (\text{A1-13})$$

where \vec{v} is the unit vector along the direction of the uniform field.

Substituting Eq.(A1-13) into the first term on the right hand side of Eq.(3-43), and solving it, we will get the field due to the sphere subjected to an uniform field.

APPENDIX 2: ANALYTIC SOLUTIONS OF TWO CO-ORIGIN SPHERES IN AN UNIFORM FIELD

The manipulation procedures in appendix 1 can be extended to evaluate the solutions for a two co-origin spheres in homogeneous medium subjected to an uniform primary field as shown in figure 10. The resistivity inside the inner sphere is different from that inside the outer sphere. The expressions for the potentials in spherical harmonic series are

$$U^e = E_0 r P_1(\cos\theta) + \sum_{n=0}^{\infty} b_n \frac{P_n(\cos\theta)}{r^{n+1}} \quad (A2-1)$$

for the points outside the outer sphere, and

$$U^{im} = \sum_{n=0}^{\infty} \left[C_n r^n P_n(\cos\theta) + d_n \frac{P_n(\cos\theta)}{r^{n+1}} \right] \quad (A2-2)$$

for the points outside the inner sphere and inside the outer sphere, and

$$U^i = \sum_{n=0}^{\infty} a_n r^n P_n(\cos\theta) \quad (A2-3)$$

for the points inside the inner sphere.

The boundary conditions across the surface of the sphere are that the potentials and the normal components of the current density are continuous. After some

manipulations of fitting the boundary conditions, we are able to find the coefficients of the series as follows:

$$a_0 = b_0 = c_0 = d_0 = 0 \quad (A2-4)$$

$$a_n = b_n = c_n = d_n = 0 \quad \text{for } n \geq 2 \quad (A2-5)$$

$$d_1 = \frac{3 E_0 R_2^3 R_1^3 \rho_2 (\rho_3 - \rho_2)}{R_2^3 (2\rho_2 + \rho_1)(2\rho_3 + \rho_2) + 2R_1^3 (\rho_3 - \rho_2)(\rho_2 - \rho_1)} \quad (A2-6)$$

$$c_1 = \frac{3 E_0 R_2^3 \rho_2 (2\rho_3 + \rho_2)}{R_2^3 (2\rho_2 + \rho_1)(2\rho_3 + \rho_2) + 2R_1^3 (\rho_3 - \rho_2)(\rho_2 - \rho_1)} \quad (A2-7)$$

$$b_1 = \frac{E_0 R_2^6 (2\rho_3 + \rho_2)(\rho_2 - \rho_1) + E_0 R_2^3 R_1^3 (\rho_3 - \rho_2)(\rho_2 + 2\rho_1)}{R_2^3 (2\rho_2 + \rho_1)(2\rho_3 + \rho_2) + 2R_1^3 (\rho_3 - \rho_2)(\rho_2 - \rho_1)} \quad (A2-8)$$

$$a_1 = \frac{9 E_0 R_2^3 \rho_2 \rho_3}{R_2^3 (2\rho_2 + \rho_1)(2\rho_3 + \rho_2) + 2R_1^3 (\rho_3 - \rho_2)(\rho_2 - \rho_1)} \quad (A2-9)$$

where R_1 and R_2 are the radii of the inner sphere and the outer sphere respectively, ρ_1 , ρ_2 , ρ_3 are the resistivities of the homogeneous earth, outer sphere and inner sphere respectively.

By the same token as that in appendix 1, we make the reference point at infinity and compare the secondary fields

of the numerical results with those of the analytic ones.

The zero order term in Eq.(2-6) is

$$\sigma_0 = \frac{K \rho_e I}{\pi} \frac{\partial}{\partial n_m} \left(\frac{1}{r_{Am}} \right) = -2 K \vec{E}_m \cdot \vec{n}_m \quad (\text{A2-10})$$

which is induced by a point charge at point A with amount of charge $2I\rho_e$, and where \vec{n}_m points outward from the body. With E being uniform, we get

$$\sigma_0 = -2 K E \vec{\nu} \cdot \vec{n}_m \quad (\text{A2-11})$$

where $\vec{\nu}$ is the unit vector along the direction of the uniform field and \vec{n}_m is the normal direction of the surface at point m.

APPENDIX 3: THE INTEGRATION OF THE KERNEL FOR THE THIN INSULATOR CASE OVER A RECTANGLE

The kernel of the integral equation for the imperfect thin insulator case contains two terms. The integration of the first term over a finite facet is approximated by Eq.(6--22) if the geometry of the thin layer is not too complicated. The integration of the second term over a finite facet is

$$\int_{S_n} (\vec{n}_m \cdot \vec{n}_p) \frac{1}{r_{pm}^3} dS_p \quad (A3-1)$$

On the finite plane facet \vec{n}_p is constant, the integration becomes

$$\vec{n}_m \cdot \vec{n}_p \int_{S_n} \frac{1}{r_{pm}^3} dS_p \quad (A3-2)$$

If S_n is a rectangle, the integration can be expressed in a closed form. When point m is not on the plane where S_n is located, the expression is

$$\int_{S_n} = \frac{a-x_m}{|z_m||a-x_m|} \left[\tan^{-1} \frac{|a-x_m|(b-y_m)}{|z_m| \sqrt{(b-y_m)^2 + (a-x_m)^2 + z_m^2}} - \tan^{-1} \frac{|a-x_m|(-b-y_m)}{|z_m| \sqrt{(-b-y_m)^2 + (a-x_m)^2 + z_m^2}} \right] - \frac{-a-x_m}{|z_m||a+x_m|} \left[\tan^{-1} \frac{|a+x_m|(b-y_m)}{|z_m| \sqrt{(b-y_m)^2 + (a+x_m)^2 + z_m^2}} - \tan^{-1} \frac{|a+x_m|(-b-y_m)}{|z_m| \sqrt{(-b-y_m)^2 + (a+x_m)^2 + z_m^2}} \right] \quad (A3-3)$$

where a , b are half the length of the edges of the rectangle, and x_m , y_m , z_m are the coordinates of point m in the coordinate system with the origin at the center of the rectangle and with the axes parallel to the edges of the rectangle.

If point m is on the plane where S_n is located, the expression is

$$\int_{S_n} = - (a-x_m) \left[\frac{\sqrt{(a-x_m)^2 + (b-y_m)^2}}{(a-x_m)^2 (b-y_m)} - \frac{\sqrt{(a-x_m)^2 + (-b-y_m)^2}}{(a-x_m)^2 (-b-y_m)} \right] \\ + (-a-x_m) \left[\frac{\sqrt{(a+x_m)^2 + (b-y_m)^2}}{(-a-x_m)^2 (b-y_m)} - \frac{\sqrt{(a+x_m)^2 + (-b-y_m)^2}}{(-a-x_m)^2 (-b-y_m)} \right] \quad (A3-4)$$

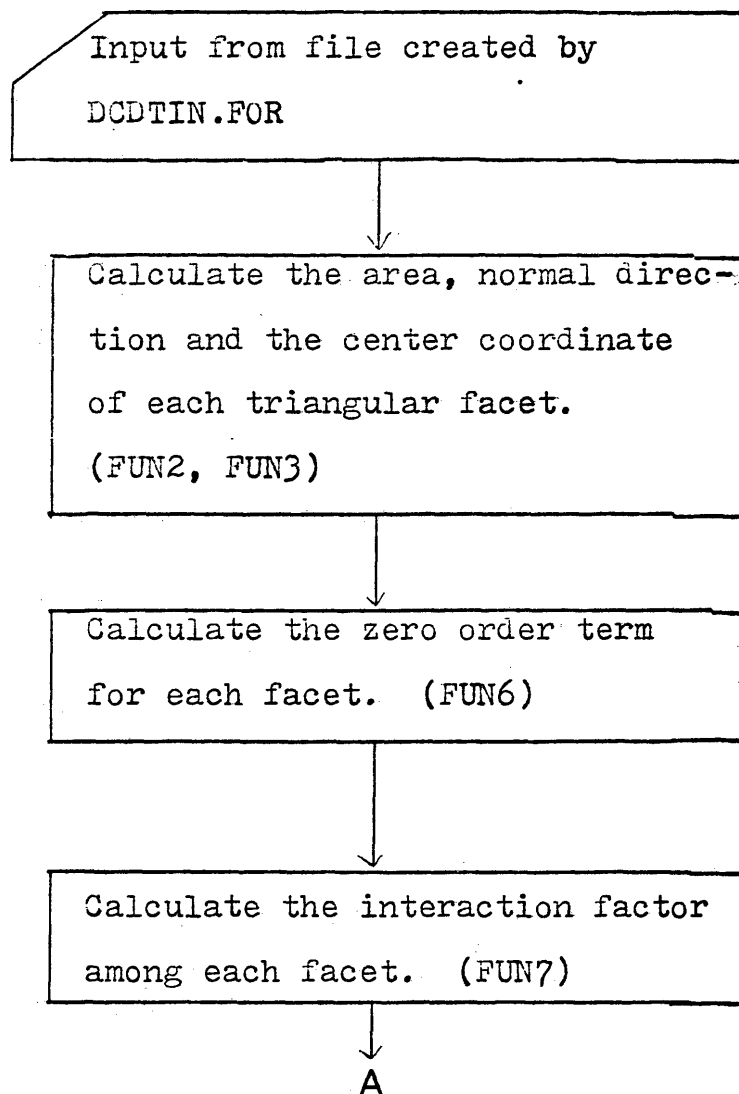
Note that for the singularity case point m is at the center of S_n . The integration can be expressed by (A3-4) for the case of $x_m=y_m=0$ and $\vec{n}_m \cdot \vec{n}_p = 1$.

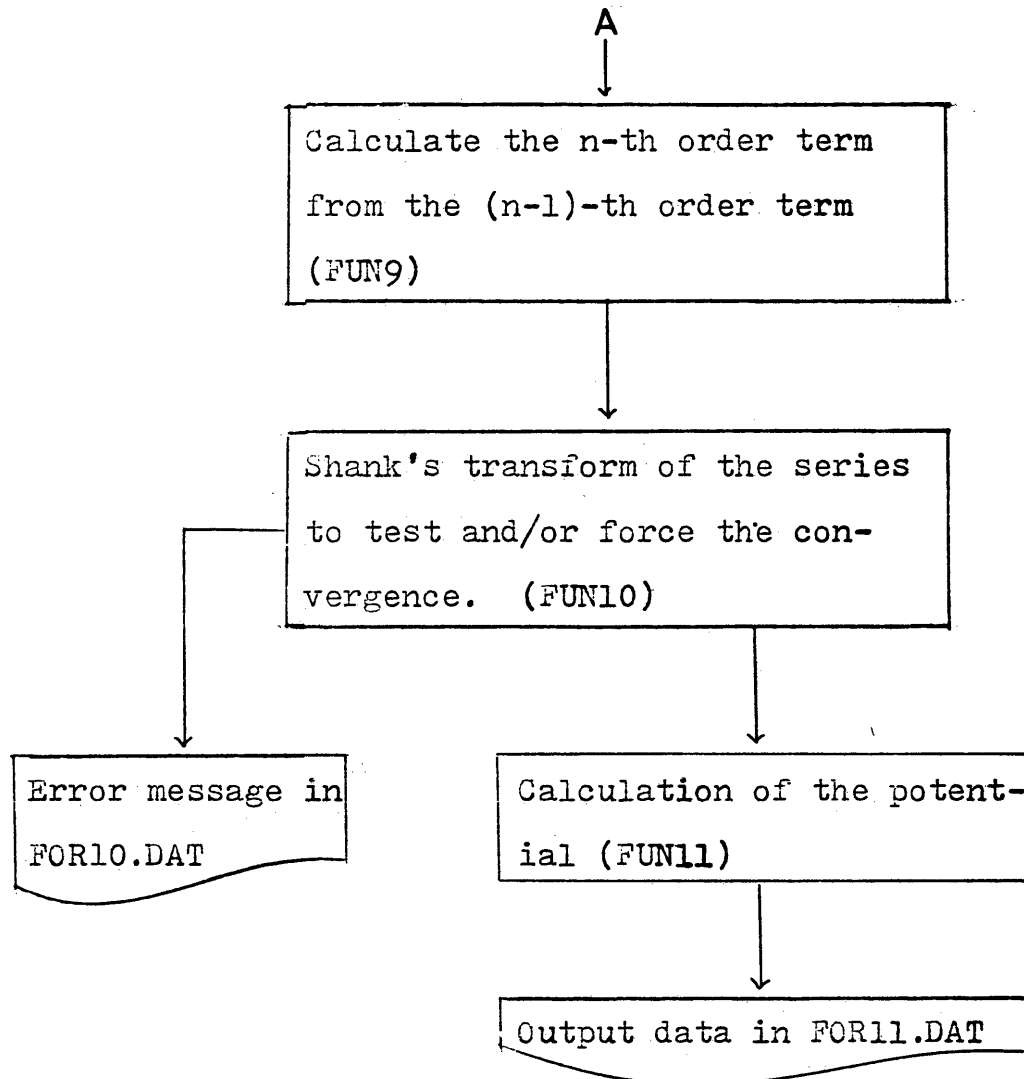
APPENDIX 4: USER'S MANUALS

Three programs have been designed in this thesis. They are DCDT3U.FOR, TOPO3U.FOR and THNR3U.FOR. The first one calculates the response of multiple bodies with the flexibility of multiple reflection coefficients. The second one calculates the potential due to an irregular surface of an uniform earth. The third one calculates the response of thin layers immersed in a homogeneous half space. The input files for DCDT3U.FOR and TOPO3U.FOR are created by DCDTIN.FOR which is a conversation-type program. The follows are the user's manuals for the four programs.

DCDT3U.FOR

This program calculates the potential for multiple bodies with the flexibility of multiple reflection coefficients. The input data file is created by DCDTIN.FOR. The flow chart of this program is shown as follows:





In order to execute this program efficiently, the users are recommended to read the manual for DCDTIN.FOR first.

TOPO3U.FOR

This program calculate the potential on the irregular surface of an uniform earth. The input files are created by DCDTIN.FOR. The irregular surface is simplified by taking a datum surface as an example shown in Fig.A4-1. The datum surface does not have to be simulated by triangles and be read by the program. The main flow chart of this program is the same as that for DCDT3U.FOR except that the extra information of the potential on each facet of the irregular surface is written in FOR12.DAT.

In order to execute this program efficiently, the users are again recommended to read the manual for DCDTIN.FOR first.



Fig. A4-1

DCDTIN.FOR

This program create an input file for DCDT3U.FOR and TOPO3U.FOR. The program is a conversation type. So it is self-explained when it is executed. Those which are not clear and which need special cares are summerized as follows:

1) To create a closed surface, it needs two suspending points as shown in Fig.A4-2. Each suspending point creates an open surface.

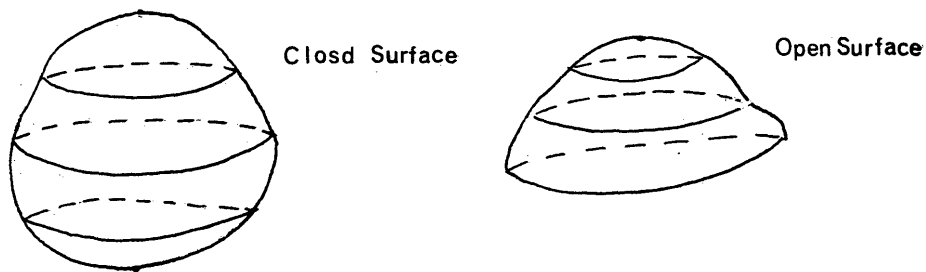


Fig. A4 - 2

2) To create an open surface, it needs the coordinate of the suspending point, the depth to each contour, the number of the vertices on the first contour, the total number of the contours. Each contour is an ellipse with respect to a center point.

3) The number of the vertices on the contours is twice of that of the previous contour. The triangular facets are

created in a way shown in Fig.A4-3.

4) As shown in Fig.A4-3, the number of the vertices of the third contour should be 16. The number of the facets created between the second and the third contours is then 24. However, the program has the flexibility to reset the number of the vertices. As shown in Fig.A4-3, the number of the vertices on contour 2 is reset to 4, and the number of the facets is now 12 instead of 24.

5) For multiple body case, the first body can have different reflection coefficients while those for the other bodies are fixed.

6) The current electrodes can be either located on the surface or buried. To avoid singularity of the computations, when the buried electrodes are used, they must not be on the surface of the buried bodies. For TOPO3U.FOR case, the current electrodes must always be on the datum surface.

7) If the body is to be simulated by triangular facets created by this program, it will be better to make the facets tangential to the bodies.

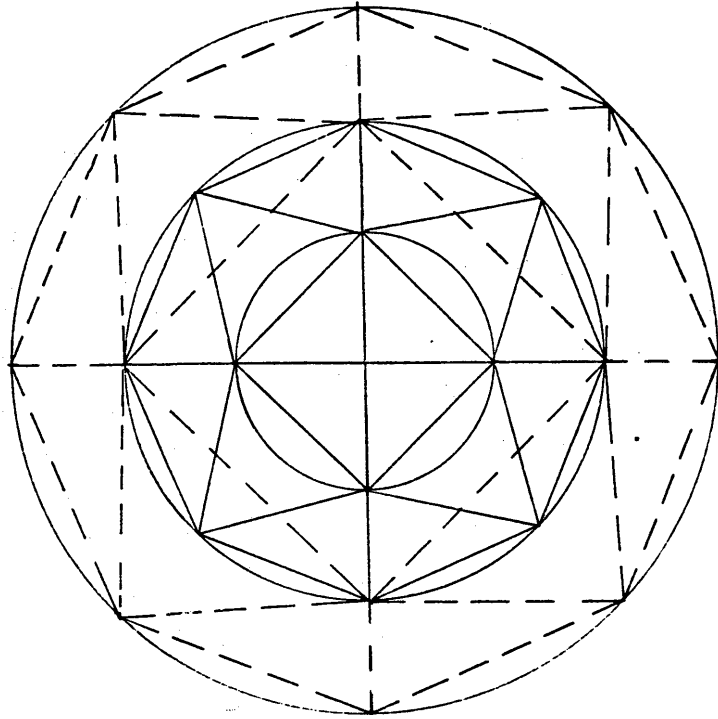
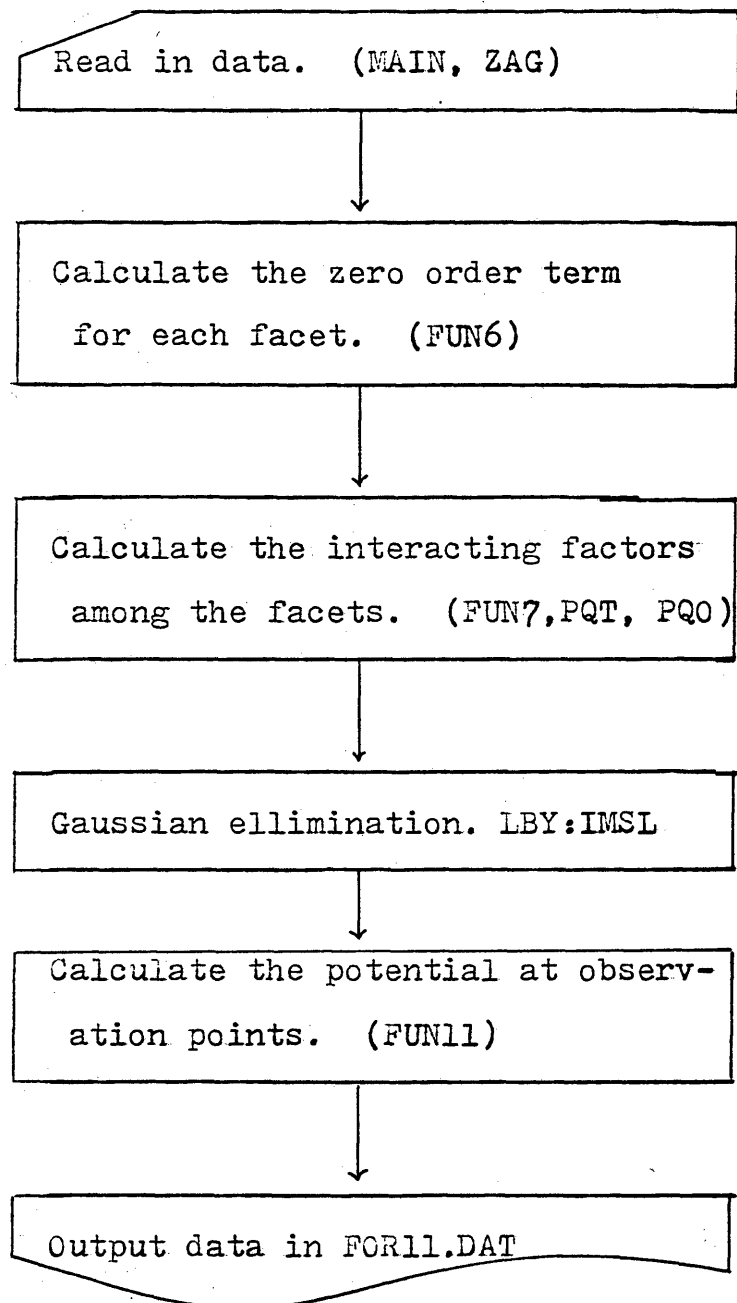


Fig.A4-3: The number of the vertices on the second contour is 8 which is twice as that for the first contour. The number of the vertices on the second contour is reset to 4 and that for the third contour is then 8. The triangular facets created by the second and the third contours are shown in dashed lines.

FHNR3U.FOR

This program calculates the potential for three dimensional thin insulators. The main flow chart is shown as follows:



The variables of the program are shown as follows:

AK: the transverse resistance of the thin layer.

NIS: the total number of the current electrodes.

XS(I), YS(I), ZS(I): the coordinate of the I-th current electrode.

SIGN(I): the sign of the I-th current electrode.

NIR: the total number of the observation points.

XR(I), YR(I), ZR(I): the coordinate of the I-th observation point.

NFS: the total number of the rectangle facets.

CF1(I), CF2(I), CF3(I): the coordinate of the center point of the I-th facet.

DF1(I), DF2(I), DF3(I): the normal direction of the I-th facet, which is opposite to the direction of the normal component of the current density flowing from the positive current electrode.

AF(I): the area of the I-th facet.

HI(I): the length of any edge of the I-th facet.

DV1(I,1), DV2(I,1), DV3(I,1): the direction cosine of one edge of the I-th rectangular facet.

DV1(I,2), DV2(I,2), DV3(I,2): the direction cosine of the edge of the I-th rectangular facet, which forms a right-hand coordinate system with (DF1(I), DF2(I), DF3(I)) and

(DV1(I, 1) ,DV2(I, 1),DV3(I, 1)).

The program reads in the general informations by the conversation from the TTY. The data about the thin layer is read in from a file specified by the input from TTY. The input sequence from this specified file is shown as follows:

(1)NFS,AK

(2G)

(2)DO ## I=1,NFS

CF1(I),CF2(I),CF3(I),AF(I),HI(I),DF1(I),DF2(I),DF3(I)

(8G)

DV1(I, 1),DV2(I, 1),DV3(I, 1),DV1(I, 2),DV2(I, 2),DV3(I, 2)

(6G)

REFERENCES

- Barnett, C. T., 1972, Theoretical modeling of induced polarization effects due to arbitrarily shaped bodies: CSM PhD Thesis.
- Boggon, J. H., 1971, Electromagnetic and electrical Modeling by the finite element method: Geophysics, v. 36, no. 1, p. 132-155.
- Bole, J. D., 1968, Perturbation methods in applied Mathematics: Ginn and Blaisdell.
- Daniels, J. J., 1977, Three-dimensional resistivity and induced-polarization modeling using buried electrodes: Geophysics, v. 42, no. 5, p. 1006-1019.
- Dieter, K., Paterson, N. R., and Grant, F. S., 1969, IP and resistivity type curves for three-dimensional bodies: Geophysics, v. 34, p. 615-632.
- Fox, 1978, Topography Effect: Professional Report, Utah University.
- Geoscience Inc., 1965, Theoretical two-dimensional resistivity and induced polarization profiles: Cambridge, Tech. Bull. 12.
- Harrington, Roger F., 1968, Field computation by moment methods: New York, Macmillan Co.
- Holmann, G. W., 1972, Electromagnetic scattering by conductors in the earth near a line source of current: Geophysics. v. 36, no. 1, p. 101-131.
- Holmann, G. W., Three dimensional induced polarization and electromagnetic modeling: Geophysics. v. 40, no. 2, p. 309-324.

Hurley, D. G., 1975, Boundary conditions for thin imperfect conductors and insulators: *Geophysical Prospecting* 23, p. 70-79.

Keller, G. V., 1966, Dipole method for deep resistivity study: *Geophysics*. v. XXXI, no. 6, p. 1088-1104.

Keller, G. V., and Frischknecht, F. C., 1966, *Electrical method in Geophysical prospecting*: New York, Pergamen Press.

Keller, G. V., Furgerson, R., Lee, C. Y., Harthill, N., and Jacobson, J. J., 1975, The dipole mapping method: *Geophysics*. v. 40, no. 3, p. 451-472.

Peter, Leo J., 1945, The direct approach to Magnetic interpretation and its application: *Geophysics*, v.14, no.3, p. 290-320.

Raiche, 1974, An Integral Equation Approach to Three-Dimensional Modeling: *Geophys. J. R. Astr. Soc.*, 36, p. 363-376.

Shanks, D., 1954, Non-linear transformations of divergent and slowly convergent sequences: Doctoral thesis of the Graduate school of the University of Maryland.

Snyder, D. D., and Merkel, R. M., 1973, Analytic models for the interpretation of electrical surveys using buried current electrodes: *Geophysics*, v. 38, p. 513-529.

Snyder, D. D., 1975, A method for modeling the resistivity and IP response of two dimensional bodies: *Geophysics* v. , p. - .

Stratton, J. D., 1941, *Electromagnetic theory*: McGraw-Hill book company, New York and London.

Van Nostrand, R.G. and Cook, K.L., 1966, Interpretation of resistivity data: U.S. Geovernment Printing Office, Washington.

Weidelt, P., 1975, Electromagnetic Induction in Three-Dimensional Structures: J. Geophys. 41, p. 85-109.